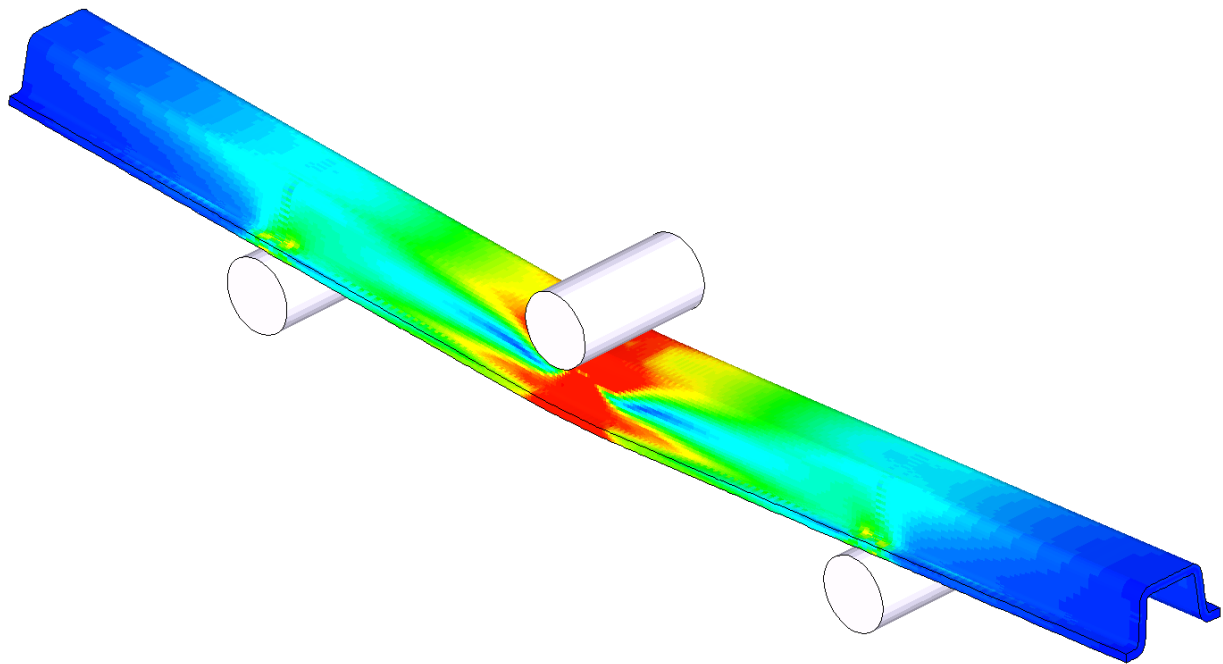# CHALMERS

Modelling and simulation of composites crash tests for validation of material models using LS-DYNA

Master's thesis in Applied Mechanics

FREDRIK KARLSSON
WICTOR GRADIN

Modelling and simulation of composites crash tests for validation of material models using LS-DYNA

FREDRIK KARLSSON
WICTOR GRADIN

Modelling and simulation of composites crash tests for validation of material models using LS-DYNA
FREDRIK KARLSSON
WICTOR GRADIN

Cover:
An illustrative figure showing a deformed beam in three point bending.

Modelling and simulation of composites crash tests for validation of material models using LS-DYNA
Master's thesis in Applied Mechanics
FREDRIK KARLSSON
WICTOR GRADIN
Department of Applied Mechanics
Division of Material and Computational Mechanics
Chalmers University of Technology

Abstract

The beneficial properties of polymer reinforced fibre composite materials permits weight savings within the car industry, allowing the vehicles to become more fuel efficient, which in turn will lower the pollutant emissions. In order to apply this group of material, a reliable material model in crash simulations is required in order to reduce testing. The purpose of the present study was to evaluate if a newly developed physically based material model improves the accuracy of finite element crash simulations.

The thesis is divided into two main parts. In the first part, the transfer of the material model from an ABAQUS environment to an LS-DYNA environment was successfully verified and benchmark tested against the physically based material model MAT261 in a small application. In the second part, the major benchmarking study was performed by a crash investigation of a three-point bending test of a beam. An additional benchmarking study was carried out by investigating crushing of a corrugated specimen. The results were compared to already performed experimental tests.

The benchmark study shows that both material models physically captures the failure behaviour in the dynamic crushing of a three-point bending test of a beam. However, since the failure behaviour in the experiment was unknown, it is hard to draw any conclusion whether the failure behaviour corresponds to the experiments or not. The correlation of the force-displacement response, as well as the absorbed energy, was poor between the simulation results and the experimental test. In the benchmarking test of the crushing of the corrugated specimen, it was however possible to see a correlation in the force-displacement relation. Although, the drop in force due to damage in the simulations was not as clear as in the experiment. The overall conclusion is that the new material model appear to be more robust than MAT261. However, in order to have a reliable material model in crash simulations, such that testing can be reduced, further development of physically based material models will be required.

Keywords: Composite failure, Crash, Delamination, Finite Element Modelling, LS-DYNA, MAT261, Three-point bending

Preface

This Master's thesis project is a part of the research project *Modelling crash behaviour in future lightweight composite vehicles* financially supported partly by Vinnova and partly by the industrial partners of the project Volvo Car Corporation, AB Volvo, Autoliv, Altair Engineering, DYNAmore Nordic, ÅF Industry AB, Semcon AB and Escenda Engineering AB. This thesis was conducted at the CAE department at Semcon AB in Gothenburg, Sweden. The project was carried out during the spring semester 2016, and corresponds to 30 higher educational credits. The examination was done by the department of Applied Mechanics at Chalmers University of Technology.

Acknowledgements

First and foremost we would like to thank Semcon AB for giving us the opportunity to carry out our Master Thesis at your office. A special thanks to our examiner, as well as supervisor, Assoc. Prof. Martin Fagerström for all your support and guidance throughout the project. We would also like to take the opportunity to thank our supervisor Fredrik Stig for your support. Moreover, we would like to thank the participants within the research group *Modelling crash behaviour in future lightweight composite vehicles*.

Last but not least we would like to thank our families and friends for their support and patience.

CONTENTS

1 Introduction

A general trend in the producing industry is to include polymer reinforced fibre composites in a greater extent than before, including the car industry. This is mainly due to the beneficial properties of great specific[1] stiffness, strength and energy absorption of this group of materials which provide a light but still high performance material. These beneficial properties permits weight savings within the car industry to be obtained, allowing the vehicles to become more fuel effective, which in turn will lower the pollutant emissions. In order to apply this material, and still be competitive and have short lead time in developing, a reliable material model in crash simulations is required in order to reduce testing.

This striving is of current interest and within this field there is an ongoing research project where Chalmers University of Technology is participator together with several industrial companies, such as Semcon AB. This have led to new improved material models for the progressive failure in composite laminates. However, in order to benefit from these models in the industrial application, a bridge between the scientific research and the daily usage of the models is necessary. This Master's thesis goal is to overcome this gap such that a new material model can be implemented in the daily simulations.

1.1 Purpose

In this project a crash model for composites, which has been developed at Swerea SICOMP, will be transferred from ABAQUS to LS-DYNA format, followed by a verification using data from already performed finite element simulations. Furthermore, benchmarking crash analyses will be conducted, and the results will be compared to an already existing model in LS-DYNA as well as with experimental tests in order to determine if this new model is improving the accuracy of the results. In order to achieve the purpose for this project the following specific goals were stated:

- To present the underlying theory of crash in composites and the material models used as well as investigate possible modelling techniques.

- To transfer Swerea SICOMP's material model from ABAQUS environment to LS-DYNA and thereafter verify the obtained model behaviour as well as benchmark against an already implemented material model in LS-DYNA.

- Extend the benchmarking to a more complex crash model and compare simulation results to experimental tests.

1.2 Delimitations

The initial ambition was to also conduct benchmarking analysis on a tube, which also have been investigated within the research project. However, due to time limitations this part was excluded.

The project will be conducted during 20 weeks with two full time working students.

---

[1]Specific refers to the ratio between a certain property and the mass.

2 Theory

In the following chapter the underlying theory of composite materials in general, with the main focus on crash, failure behaviour as well as common modelling techniques are presented. In addition the theory behind the material models under consideration in this thesis is presented.

2.1 Composites

A composite material is according to Agarwal et al. [1] a material which constitutes of at least two distinct materials, and it consists of one or more discontinuous phases embedded in a continuous phase. The latter one is in literature referred to as the matrix, whereas the discontinuous phase is referred to as the reinforcing material also known as the fibre.

2.1.1 Crash in composites

The beneficial specific energy absorption properties of composite materials make them attractive for crash structures [2]. This since the main target in crash is to absorb as much energy as possible without causing damage to the occupant meanwhile minimising the weight of the component. According to Jacob et al. [3] the specific energy absorption for a carbon fiber reinforced polymer composite typically is in a range of 120-220 kJ/kg. As a comparison this value for steel can be in the range of 20-40 kJ/kg [4]. In composite materials the main energy absorption occurs after initial cracks have been initiated, and progresses as the progressive crushing continues. However, the energy absorption in composite materials depends on which failure modes that are triggered. According to Jacob et al. [3] there are mainly two failure modes when it comes to composite materials, namely catastrophic failure and progressive failure. The first mentioned is not of interest when it comes to designing crashworthy structures while progressive failure is. This since the energy absorbed in catastrophic failure is smaller than in progressive failure [3].

In order to determine the absorbed energy in a crash, the relation between the force and the displacement needs to be considered. The force-displacement response typically increase linearly up to when failure initiates, and the force then decrease as the failure progresses. Final failure is reached when the structure is no more able of carrying any load. A schematic illustration of a typical force-displacement curve, in progressive failure, is being illustrated in Figure 2.1. The total amount of absorbed energy can be obtained by evaluating the area under the force-displacement curve.
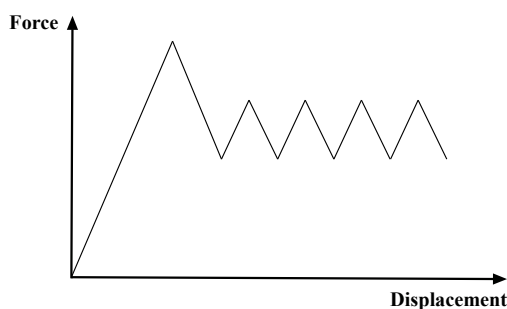
Figure 2.1: An illustrative force-displacement curve for progressive failure.

2.1.2 Failure modes

The definition of failure differ within different structural applications. In some applications the structure is considered to fail as soon as small permanent deformations occur, whilst in other applications failure arises when total fracture occur [1]. In crash the latter one is considered since the main energy absorption in the

material occur after initial crack initiation and thus the following content will have the main focus in this approach. For composite materials, internal material failure occurs before any visual aspects of failure is observed. The internal material failure may be observed in many forms such as fibre breakage, microcracking of the matrix and local separation of plies (delamination) [1]. For the special case when all the fibres are oriented in the same direction, namely unidirectional (henceforth referred to as UD) fibre reinforced composites, the failure modes can be divided into two separate failure groups; matrix and fibre failure modes [1].

Matrix failure modes

Matrix tensile failure occurs when the structure is loaded in transverse direction which give rise to high stress concentrations around the fibres. This may lead to crack initiations in the interface between matrix and fibres [1]. The fracture plane, that is the plane where failure occurs, is located normal to the applied load as can be seen in Figure 2.2(a) [5]. The strength in this mode is usually low with a typical value within the range of 40-80 MPa [1].

According to Pinho et al. [5] matrix compressive failure is mainly dominated by matrix properties, and failure is driven by shear. This implies that it is intuitively to expect the fracture plane to be located in the plane where maximum shear stress is located, i.e. with 45 degrees rotation normal to the applied load. However, it has been experimentally shown by Pinho et al. that the fracture plane is located with an angle of 53 degrees for most composite materials. For this mode the strength is typically in the range of 140-300 MPa [1]. Figure 2.2(b) illustrates a schematic view of the matrix compression failure mode.

(a) Matrix tension   (b) Matrix compression
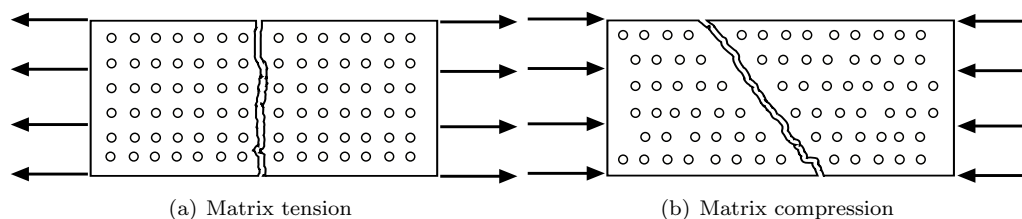
Figure 2.2: Matrix failure modes in tensional and compressional loading.

Fibre failure modes

When the structure is loaded with tensional loads in the fibre direction, catastrophic failure may occur as a result of the accumulation of individual fibre failures within plies. According to Orifici et al. [6] this occur when not enough intact fibres is remaining to carry the required loads, causing the load to be redistributed to the matrix. The strength in this mode is high with a typical value within the range of 1500-2200 MPa [1].

If compressive loads are applied, microbuckling and kinking bands may occur. According to Pinho et al. [7] microbuckling occurs as a result of instability of fibres within the elastic matrix, whereas the formation of kinking bands occur due to an initial misalignment within the structure. These misalignments cause the stresses to be redistributed, promoting more misalignment of fibres to arise, which in turn triggers failure [7]. For this mode the strength is typically in the range of 800-1800 MPa [1]. Figure 2.3 schematically illustrates the failure modes when a structure is loaded with tension and compression in the fibre direction.
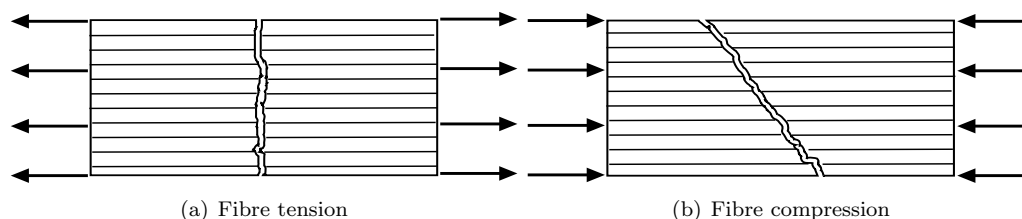

(a) Fibre tension   (b) Fibre compression

Figure 2.3: Fibre failure modes in tensional and compressional loading.

Delamination

The phenomena where laminated composite materials tend to separate from each other, is in the literature referred to as delamination. Delamination is according to Oricifi [6] caused by high through-thickness stresses and may occur in three different modes; peeling, shearing and tearing. The three modes are illustrated in Figure 2.4. Depending of the composite's layup and stacking sequence as well as the loading condition, one or several of the damage modes may be triggered [8]. Delamination can according to for instance [9] and [8] be taken into account in Finite Element simulations by introducing cohesive elements between plies.
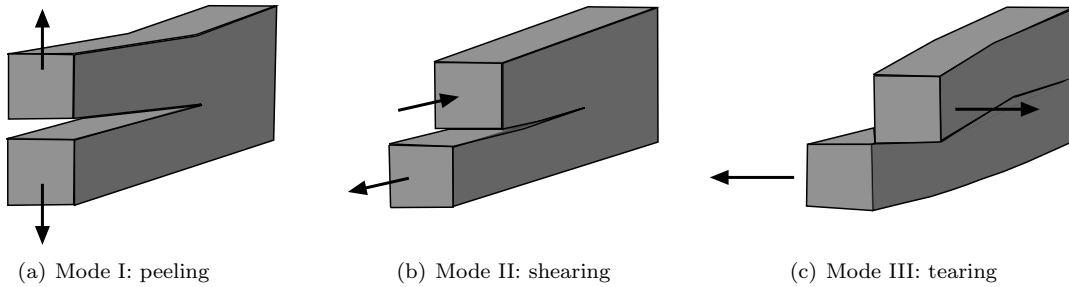

(a) Mode I: peeling   (b) Mode II: shearing   (c) Mode III: tearing

Figure 2.4: Delamination failure modes.

2.1.3 Finite element modelling techniques

The modelling of composite materials can be divided into two main areas where the first one determines how the plies are modelled. The second one is how the connection between each ply is modelled. In this section different state of the art methods for these areas are presented. Furthermore numerical aspects of modelling due to under integration of the elements is also presented.

Composite discretisation methods

The most common way to model the plies is to model them either using shell or solid elements. For both these element formulations it is possible to either use one element through the stack-up of the composite or to have one element for each ply. If one element through thickness is used, no interlaminar behaviour can be captured if this is not included in the material model. Using solid elements is in general more computational expensive than using shell elements. This since a larger in-plane and out-of-plane aspect ratio can be used using shell elements. The kinematic modelling in the solid elements have less approximations than shell elements which in some cases use the approximation of plane stress. However, the bending is in general captured in a more satisfying way with shell elements.

When using shell elements there are mainly two approaches to model a composite. One option is to use layered thin shell elements, which only have one shell element through the thickness of the composite. The stack-up has one or more integration points which defines each ply through the thickness. The classical laminate theory is the underlying calculation foundation. An illustration of this element formulation can be seen in Figure 2.5(a). The second modelling approach using shell elements is to use stacked shell elements, see Figure 2.5(b). In this method each ply throughout the thickness is represented with a separate shell element [10].

If solid elements are used, there are mainly three stacking approaches which can be applied. The first one is to use one single element which adds all the separate ply properties together using a smeared material model in accordance to their volume fraction, Figure 2.6(a) [10]. The second approach is to use one or several solid elements for each ply in the stack-up, as illustrated in Figure 2.6(b). This makes it possible to resolve each ply separately and if using at least three elements for each ply it is possible to capture the bending stiffness accurately in each ply even if delamination has occurred. In order to have small length to thickness ratio in this approach, to prevent locking effects, the discretisation needs to be fine [10]. Consequently this approach is highly computational expensive. The final approach is to use thick shells, which is an element formulation combining the low computational costs in the shell formulation with the three-dimensional solid elements. The

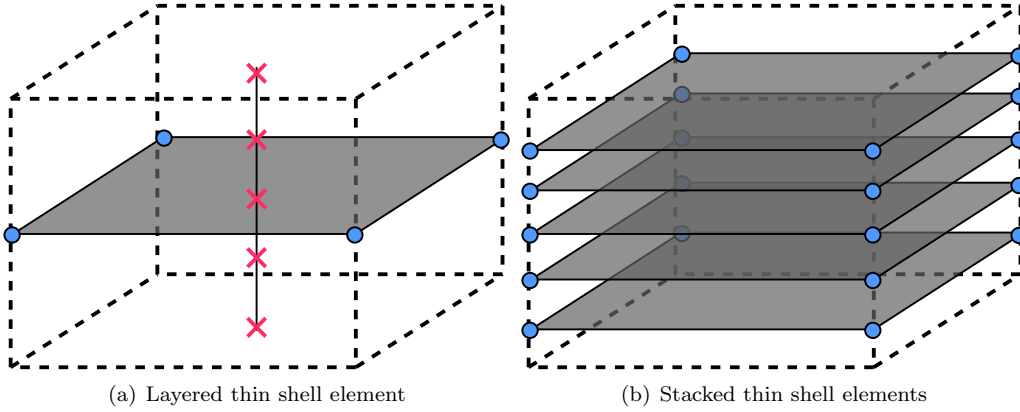(a) Layered thin shell element   (b) Stacked thin shell elements

Figure 2.5:   Composite of five plies modelled using two methods for shell elements.

thick shell elements have, as a solid element, eight nodes and uses one element through the thickness for the composite. In addition, each ply in the composite is added inside the element using integration points, as with layered thin shells. An illustration of the thick shell elements can be seen in Figure 2.6(c).

Delamination modelling methods

There are two main methods to model the interface between the plies; tiebreak contacts and cohesive elements. To be able to use these methods it is required that each ply is modelled separately using either solid or shell elements. Although if delamination does not need to be modelled between some of the plies, these can be modelled using one single element. The first method is to use tiebreak contacts for modelling the interface between the plies. This method uses a mathematically based failure criteria in order to prescribe when the plies should separate. Using a stress based approach the failure criteria describing when delamination occur may be expressed according to Equation (2.1). σ_n and σ_s represents the normal and shear stresses at the interface. In addition, NFLS and SFLS corresponds to the strength of the contact in the normal and shear direction. When this condition has been fulfilled the plies separate. The energy released due to the delamination is calculated from the relation between the separation distance between the plies as well as the combination of the interfacial stresses in the tiebreak, according to Siromani et al. [11].

$$\left(\frac{|\sigma_n|}{NFLS}\right)^2 + \left(\frac{|\sigma_s|}{SFLS}\right)^2 \geq 1 \tag{2.1}$$

According to Karlsson et al. [12] cohesive elements do not have a physical material, instead they describe the degrading load carrying capacity using a nonlinear spring based approach. The force response depends on the neighbouring faces through a defined cohesive law which is illustrated in Figure 2.7(a). The traction vector, $\mathbf{t}$, is dependent of the separation distance, d. The traction vector is linearly increasing as d increases until the separation distance have reached a critical separation distance d_e. When the distance increases further failure initiates at the interface. Total failure occur when the critical separation distance d_c is reached. Since the response only is described by a mathematical law the elements do not need a thickness. Both shell and solid elements can be defined to have a cohesive law between them [12]. In Figure 2.7(b) an illustrative example of a cohesive element can be seen. According to a study conducted by Fleming [13] cohesive elements gives substantially better results than using tiebreak criterion.

Hourglass effects

When using finite element as a discretisation method it is of importance to be aware of diverse numerical complications that may occur during a simulation. These complications can in some cases be directly linked to the choice of discretisation, that is the choice of element type and the number of integration points. When using elements with reduced integration, that is elements with one integration point, a well known numerical instability

(a) Layered solid

(b) Stacked solid

(c) Layered thick shell
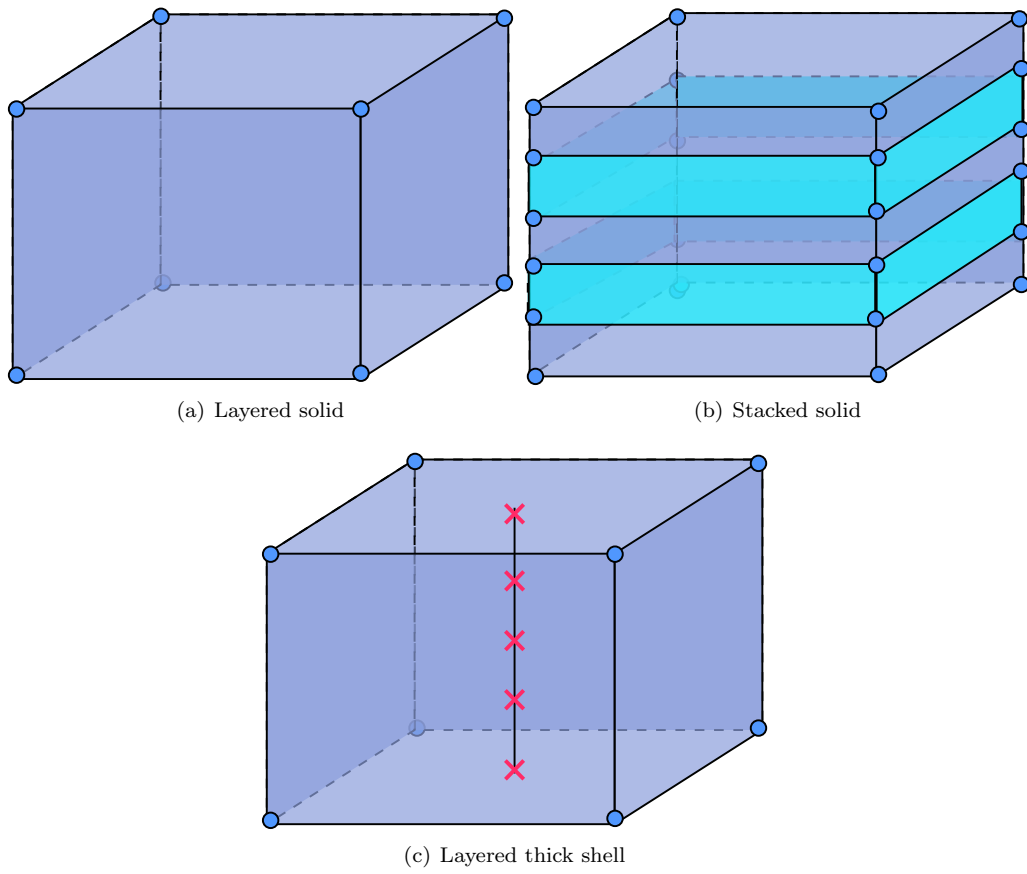
Figure 2.6: Composite of five plies modelled using different methods for solid elements.
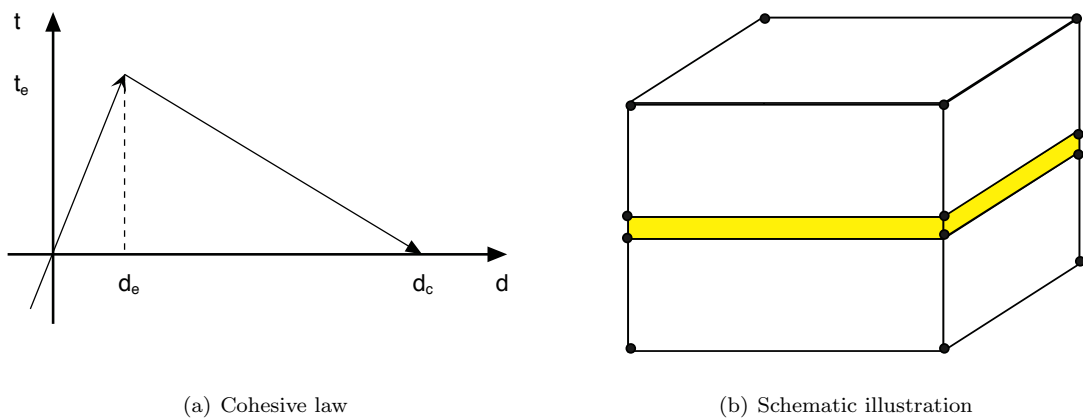

(a) Cohesive law

(b) Schematic illustration

Figure 2.7: Illustration of the cohesive law as well as two eight noded solid elements with an interlaminar cohesive eight noded element.

called hourglass can occur. Hourglass can according to Belytschko et al. [14] be considered as a spurious zero energy mode which in static solutions may cause singularities of the stiffness matrix. An illustrative representation of a possible zero energy mode is illustrated in Figure 2.8, for a four noded quadrilateral element.
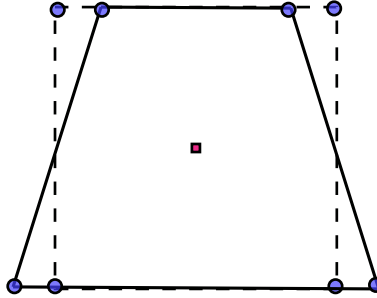

Figure 2.8: Schematic illustration of an undeformed under intergrated element (dashed line) with a possible zero energy mode (solid line).

There are several ways to control this mesh instability phenomena, including viscous based hourglass control as well as stiffness based hourglass control. Common for both these techniques is that they add artificial energy to the model in order to compensate the spurious zero energy mode. This implies that the artificial energy will be added to the total internal energy, if hourglass instability occur. In order to have reliable results from the finite element simulations, the ratio between the artificial and the internal energy should not exceed 5% [15].

Time step size

The largest time step possible to be used in an explicit solver using solid elements have a relation to the element size and the density according to Equation (2.2), where c is the wave propagation velocity in the material [10]. It can be seen that there is a linear relation between the smallest element length and the calculated critical time step. Thus, the smallest element will control the time step. The time step used in the simulation is not allowed to exceed this critical time step, Δt_{crit}.

$$\Delta t_{crit} \approx \frac{L_{crit}}{c} \tag{2.2}$$

In-situ

Material data for composites is based on tests using UD test specimens. However, in multi-directional ply stack-up's the neighbouring plies bounds the shear and transverse failure which partly prohibits the failure in the plane. This entails that the strength of which the initial damage occur is to low in this application. In order to compensate for the difference in the strength from the material data and the actual application strength in the composite, the strength parameters can according to Olsson [16] be scaled to a so called in-situ strength.

Non crimp fabric (NCF)

In applications of composites in industry there is often an advantage, due to manufacturing cycle time and costs, to use similar methods as for textiles. This in order to get a multi-directional fibre directed material instead of using autoclave of stacked UD prepreg sheets. There are different kinds of automated textile processes where the fibres can be bundled and locked together manually. An example of such a method is a woven fabric, which schematically is being illustrated in Figure 2.9. These textile methods have in general lower material properties compared to UD prepreg's due to the effect of crimp. Crimp occurs when the fibres curves when locked together [17].

In order to reduce the crimp and thus minimising the decrease of the material properties, another method can be used called non crimp fabrics (henceforth refereed as NCF). This method stitches together layers of UD
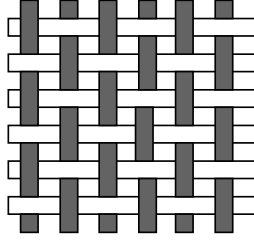
Figure 2.9: Plain weave.

fibres which can be oriented in different directions. When stitching the layers together some crimp occur since the fibres are pushed aside which generates small local defects. The consequence of the still arising crimp is that the material still does not achieve as good material properties as the UD laminate. However the local in-plane tension and compression properties are greater than a woven fabric material [17]. The fracture plane angle in matrix compression is in general higher for NCF materials compared to UD prepregs. This is due to the higher internal friction [18].

2.2 Material models

The theory behind the material model MAT261, as well as the material model developed within the research project to which this master thesis project belongs, will in this section briefly be presented. Initially the theory behind a fixed crack model, which both models are based on, will be presented.

2.2.1 Fixed crack model

A fixed crack model uses the assumption that after crack initiation the fracture only develops in a plane, the fracture plane. It is on this plane a chosen material model is applied in order to give the stress strain relation. When damage is initiated a crack in a fracture plane arises. The strain in the material is then transferred to the fracture plane coordinate system. In this local system the traction vector is calculated using a chosen constitutive law. The stress assumes to be the same as for the undamaged state [19]. The angle of the plane in relation to the material coordinates is either estimated from previous knowledge, or determined from several potential fracture planes. This is done by calculating the traction vector for several potential fracture planes and determine the most critical plane for crack initiation.

2.2.2 LS-DYNA material model MAT261

This material model is developed by Pinho et al. [20] and utilises a three-dimensional failure criteria which is physically based. The failure modes included in the material model are; fibre compressive and tensile fracture, as well as matrix tensile and compressive fracture with the angles of the fracture plane of 0 and typically 53 degrees respectively.

In fibre tension the max stress criterion predicts the failure initiation (f_{ft}), whereas Mohr-coulomb based criteria are assumed to be applicable for failure initiation in matrix tension (f_{mt}) and compression (f_{mc}). For matrix compression the specific criterion used is according to Puck [20]. The model uses a three-dimensional kinking model for failure initiation in fibre compression (f_{fc}). The equations describing each mode of failure

initiation is presented in Equation (2.3).

$$f_{ft} = \frac{\sigma_{11}}{X_t}$$

$$f_{fc} = \begin{cases} \left(\dfrac{\tau_T}{S_T - \mu_T \sigma_N}\right)^2 + \left(\dfrac{\tau_L}{S_L - \mu_L \sigma_N}\right)^2 & if \quad (\sigma_n \leq 0) \\[2em] \left(\dfrac{\sigma_N}{Y_T}\right)^2 + \left(\dfrac{\tau_T}{S_T}\right)^2 + \left(\dfrac{\tau_L}{S_L}\right)^2 & if \qquad (\sigma_n \geq 0) \end{cases}$$

$$f_{mt} = \left(\frac{\sigma_N}{Y_T}\right)^2 + \left(\frac{\tau_T}{S_T}\right)^2 + \left(\frac{\tau_L}{S_L}\right)^2$$

$$f_{mc} = \left(\frac{\tau_T}{S_T - \mu_T \sigma_n}\right)^2 + \left(\frac{\tau_L}{S_L - \mu_L \sigma_N}\right)^2$$

(2.3)

The effective stress for all load cases is linearly decreasing when damage has been initiated. The decrease is proportional to the damage variable in relation to the strain according to a bilinear damage law, see Figure 2.10 [5]. This linear decrease of stress is due to the decrease in stiffness of the material after damage. The strength decrease implies that a partially damaged material is still able to carry load after breakage, however the capability is linearly decreasing as the strain increases. When the crack is fully developed and no more growth of the crack occur the model does not continue to absorb energy. A smeared formulation is used in this model. This implies that the fracture energy is evenly distributed over the volume of the element [5].
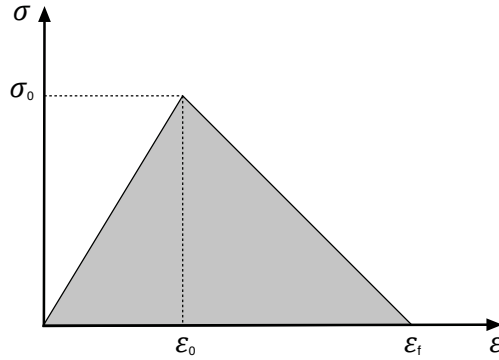
Figure 2.10: A bilinear damage law with a linear decreasing of the strength after damage.

Material card MAT261

The material card for MAT261 is described in LS-DYNA's Keyword User's Manual Volume 2 [21] and can be seen in Table 2.1. The card can be divided into three main sections. The blue values are the material parameters which corresponds to the elastic orthotropic response. The red parameters defining the coordinate system of the material in relation to the local element coordinate system. Finally the green parameters determines the response after initial failure. The green parameters in card 2 determines the removal of failed elements as well as the failure behaviour of the composite. The green parameters in card 5 and 6 determines the bilinear behaviour from the fracture toughness and the strength of the material. Finally the fracture angle, non-linear shear behaviour as well as softening in the crash front is defined in card 7. For more detailed description of each variable as well as the values used in the simulations, see Appendix C.

Table 2.1: Material card MAT261.

Card 1	MID	RO	EA	EB	EC	PRBA	PRCA	PRCB
Card 2	GAB	GBC	GCA	AOPT	DAF	DKF	DMF	EFS
Card 3	XP	YP	ZP	A1	A2	A3		
Card 4	V1	V2	V3	D1	D2	D3	MANGLE	
Card 5	ENKINK	ENA	ENB	ENT	ENL			
Card 6	XC	XT	YC	YT	SL			
Card 7	FIO	SIGY	LCSS	BETA	PFL	PUCK	SOFT	

2.2.3 SICOMP's material model - version one

The first version of the material model developed within the research project by Swerea SICOMP is a model which combines progressive damage and friction in the matrix compressive failure mode. This in order to account for local effects such as the friction created in microcracks. The added friction is only focusing on the matrix shear arising in matrix compressive loading in accordance to the theory by Gutkin et al. [19]. The theory is based on a fixed crack model in combination with a damage and friction formulation. The assumption that the fracture plane is fixed would be a good approximation since the failure in compression is driven by the shear component of the traction vector in this plane [19]. In addition, this material model includes the same failure modes and damage laws as the material model MAT261 developed by Pinho et al. [20], except that kinking in fibre compressive failure is not included in this model. Instead the max stress criterion is used. The equations describing each failure mode is presented in Equation (2.4).

$$f_{ft} = \frac{\sigma_{11}}{X_T}$$

$$f_{fc} = \frac{|\sigma_{11}|}{X_C}$$

$$f_{mt} = \left(\frac{\langle \sigma_N \rangle_+}{Y_T}\right)^2 + \left(\frac{\tau_L}{S_L}\right)^2 + \left(\frac{\tau_T}{S_T}\right)^2$$

$$f_{mc} = \max_{\alpha \in [0,\pi]} \left\{ \left(\frac{\tilde{\tau}_L}{S_L}\right)^2 + \left(\frac{\tilde{\tau}_T}{S_T}\right)^2 \right\}$$

(2.4)

Coupling damage and friction in transverse compression

For a constant compressive stress and a steady increasing shear deformation, the material initially behaves linear elastic until damage initiates. The damage area will in compression give rise to frictional forces due to contact between faces of the microcracks in the matrix. In order to include the friction in the material model the shear stress can be calculated from a combination of the shear deformation and the friction.

The shear stress in relation to the shear deformation can be seen in Figure 2.11. The response can be divided into three main regions where the first, region A, is the elastic region where no damage has been introduced. The second, region B, is where both the shear deformation and the friction together is the source to the shear stress. The last region, region C, is where only the shear stress arise due to friction, which occur when the damage is fully developed. If comparing this behaviour to a model following a bilinear damage law, as for MAT261 in Figure 2.10, it can be seen that the initial elastic region is still the same. However if the material experience compressive normal stresses in the matrix when damage has been initiated, a non-linear softening behaviour occur in SICOMP's model instead of the linear softening in the bilinear law. Furthermore, after the damage is fully developed SICOMP's material model still absorb energy due to friction which the bilinear law

does not capture. As for the material model MAT261 a smeared formulation is used in SICOMP's model. The present version of SICOMP's material model is only valid for elements with an aspect ratio of one [19].
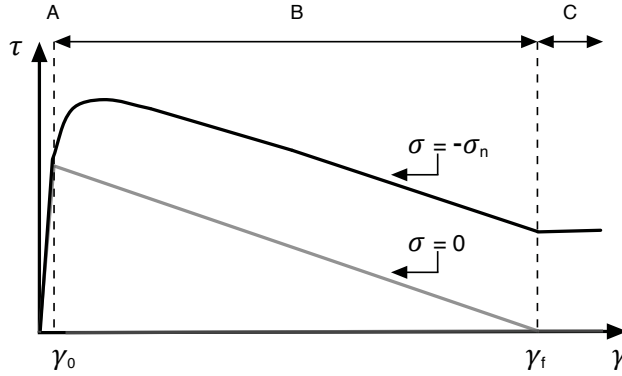

Figure 2.11: One dimensional illustration of the shear response with a damage model using friction.

Model algorithm for transverse compression

The main approach for matrix compressive failure is to initially calculate the trial stress using the material behaviour of a linear elastic transversely isotropic model. This give a linear relation between the trial stress and the strain as can be seen in Equation (2.5).

$$\tilde{\sigma} = C : \varepsilon \tag{2.5}$$

In order to determine the angle of the plane where fracture will be initiated, the stress is rotated to multiple potential fracture planes using a transformation matrix. For each plane the corresponding traction vector is evaluated which then is used in order to calculate f_{mc} in Equation (2.4), which is the damage initiation criterion in transverse compression. The potential fracture plane which maximise the function is the fracture plane where the crack growth is assumed to occur if damage arises. If this value is larger than 1 the material experience initiation of fracture in that plane. The material response on the fracture plane is then calculated using the constitutive law which couples damage and friction which assumes that dissipation of energy is due to damage formation and friction from sliding. Furthermore, the total strain is used in calculation of the damaged stress since only sliding give rise to permanent strains [19].

Material card SICOMP's model

The material card for the user material can be seen in Table 2.2. In the first card, the number of input and output parameters are defined as well as the parameters needed to calculate the time step and a flag indicating if the material is orthotropic. If failure is allowed or element temperature and deformation gradients should be considered, this can be defined in the second card. The third and forth card defines the direction of the material within each element and finally the last card is where all values on the input parameters are defined. All material parameters, except the strength parameters, were hard coded inside the material subroutine. For more detailed description of each variable as well as the values used in the simulations, see Appendix B.

Table 2.2: Material card for the user material.

Card 1	MID	RO	MT	LMC	NHV	IORTHO	IBULK	IG
Card 2	IVECT	IFAIL	ITHERM	IHYPER	IEOS			
Card 3	AOPT	MAFC	XP	YP	ZP	A1	A2	A3
Card 4	V1	V2	V3	D1	D2	D3	BETA	IEVTS
Card 5	P1	P2	P3	P4	P5	P6	P7	P8

Overestimation of onset strain in transverse compression

When it comes to the present version of SICOMP's material model, there is no guarantee that the onset strain, γ_0, should be less than the maximum strain, γ_f. In order to understand how this affect the material behaviour, a simplified case when $\tau_L = 0$ is here described. During one time step the stress calculated τ'_0, using an elastic relation to the strain, can become higher than the strength of the material in transverse shear, S_T. Furthermore, the strain corresponding to this stress will then be the onset strain, γ'_0, and thus exceed the maximum strain allowed before final failure, γ'_f. This material behaviour is illustrated in Figure 2.12 where Figure 2.12(a) shows the theoretical response and Figure 2.12(b) illustrates the behaviour that may occur. If a sudden change in stress occur between two time steps, the onset strain may exceed the maximum failure strain, which implies that the material model may give a non physical response.

(a) Theoretical bilinear response   (b) Emerging bilinear response
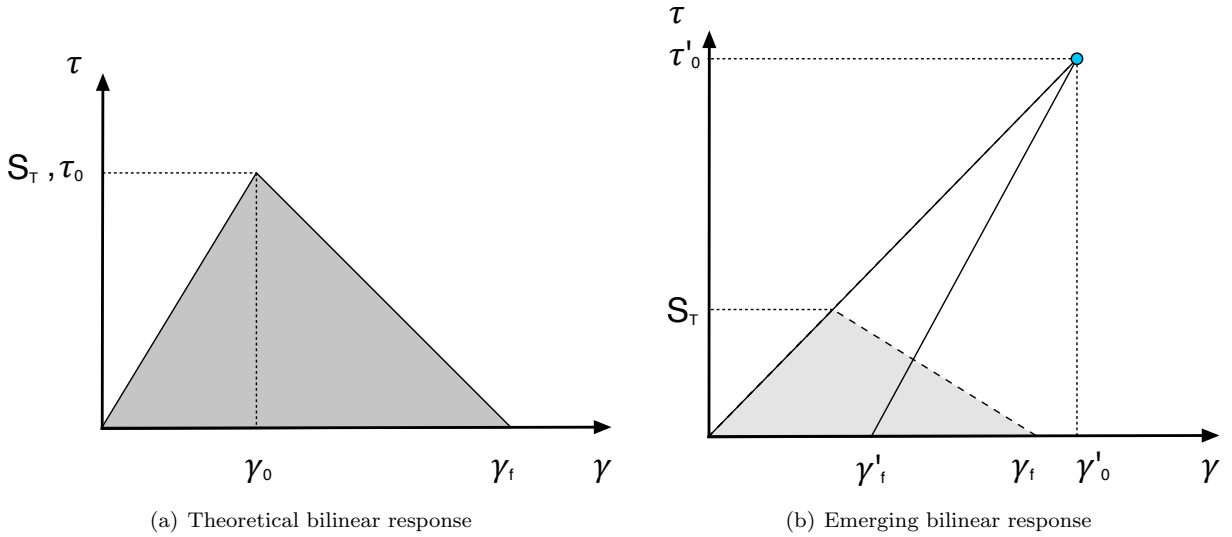
Figure 2.12: Bilinear damage law illustrating when the maximum strain, γ_f, is less then the onset strain, γ_0. In b), γ'_0 and γ'_f denotes the resulting erroneous parameters for the failure model whereas γ_f denotes the expected values as also indicated in a).

3 Method

In the beginning of the project a literature study was conducted. Information regarding the material model which has been used was gathered as well as for crash modelling for composites in general. In this phase the softwares ANSA and LS-DYNA were studied using tutorials from respective software company.

After the literature study, the material model was analysed using a small cube in order to verify the transfer of the material model. The setup for the tests were in accordance with the method used by Costa [15] when the verification of the material model was performed. The cube studied was three dimensional and subjected to several loading cases in order to capture the behaviour of the material. Each loading case was simulated with different mesh refinements to capture discretisation effects.

Initially MAT261, an already existing material model in LS-DYNA, was used in the cube simulations. This in order to get familiar with the software and the behaviour of this kind of material model. In parallel with this, the studied material model was transferred from ABAQUS to LS-DYNA where the analysis was carried out. The transfer of the material model was performed by the participants in the research project, to which this thesis belongs. When the material model was transferred, and verified, a benchmarking analysis was carried out for this cube by comparing the results between the transferred material model and MAT261.

The benchmarking of a beam subjected to three-point bending setup, previously experimentally tested within the research project to which this master thesis project belongs, was performed. Thus, the component was modelled as close to the experimental setup as possible in order to get a useful comparison with the experimental results.

The first step when modelling the beam was to use a coarse discretisation using solid elements, and apply an elastic ideally plastic material model. This model was used in order to investigate the behaviour of the structure regarding different parameters such as; the friction coefficient between the beam and the supports and the length of the beam. The beam was modelled using one element through the thickness of each ply and the material model developed by Swerea SICOMP was applied to the beam. The results were compared to the experimental tests, as well as with the results obtained using MAT261. Furthermore, delamination was included in the beam between the interfaces where the neighbouring plies had different directions of the fibre.

In order to reduce the computational costs, a transition from solid elements to shell elements was investigated. Two approaches were tested. The first one was to have additional shell element rows overlapping the solid elements. The second approach was to use a rigid connection between all the nodes at the solid boundary surface and the shell edge. Both these approaches captures the rotation of the solids and transfer this behaviour to the following shells. In order to make sure that the solid to shell transition was transferring the dynamics in a correct manner, dynamic simulations were carried out.

In addition to the investigation of the beam, a corrugated specimen was studied. The specimen was modelled using both MAT261 and SICOMP's material model and the results were compared between each other as well as to experimental results.

In this thesis two versions of LS-DYNA (R7.1.2 as well as R8.1.0) were used in different comparisons due to the accessibility of these two versions throughout the project. In addition ANSA v16.0.1 was used as preprocessor and LS-PrePost v4.3 as well as META v15.1.2 as postprocessor. The simulations were conducted using an explicit solver.

4 Testing

In this chapter the experimental tests already performed prior to this study will be presented. The experiments performed includes quasi-static [22] and dynamic [23] crushing in a three-point bending of a beam, as well as a quasi-static crushing of a corrugated specimen [24].

4.1 Material used in experimental test

The experimental tests were preformed using a carbon fibre reinforced polymer HTS45/LY556 which is a NCF material. The NCF is stitched using glass fibre/plyamide threads and selected material parameters for the material can be seen in Table 4.1 in accordance to Bru et al. [25]. In addition, the fracture angle in this material is 62 degrees. For more information about the material and how these parameters were obtained, see [25].

Table 4.1: Material parameters for HTS45/LY556 used in the experimental testing.

Elastic properties				
Modulus			**Poisson's ratios**	
E_{11} (MPa)	E_{22} (MPa)	G_{12} (MPa)	ν_{12} (-)	ν_{23} (-)
132000	9300	4400	0.29	0.4
Strength properties				
	X_t (MPa)	Y_t (MPa)	S_L (MPa)	
	1787	29.2	77.8	
	X_c (MPa)	Y_c (MPa)	S_T (MPa)	
	631	130	60	
Friction properties				
Internal pressure			**Coefficient of friction**	
p_{0L} (MPa)	p_{0T} (MPa)		μ_L (-)	μ_T (-)
75	30		0.32	0.32
Fracture toughness				
Interlaminar				
	$G_{Ic}(kJ/m^2)$		$G_{IIc}(kJ/m^2)$	
	0.149		0.69	
Intralaminar and translaminar				
$G_c^{ft}(kJ/m^2)$	$G_c^{fc}(kJ/m^2)$	$G_c^{mt}(kJ/m^2)$	$G_{IIc}^{mt}(kJ/m^2)$	$G_{IIc}^{mc}(kJ/m^2)$
67.1	103.1	0.149	0.69	0.69

4.2 Three-point bending of a beam

The beam which experimentally was tested, prior to this thesis, had the dimensions according to Figure 4.1(a), with a total length of $L = 935$ mm. The beam was tested in a three-point bending test and Figure 4.2 illustrates the test setup for both the quasi-static test, Figure 4.2(a), and the dynamic test, Figure 4.2(b). The beam rests on two cylindrical supports which have a diameter of 50 mm and a distance between them of 500 mm, see Figure 4.2(a). In addition, the diameter of the impactor was the same as for the cylindrical supports. The plies within the material had 0 degree fibre direction except for the outermost plies which had the direction of 90 degree, having a total of 32 plies. A zero degree fibre direction is defined in accordance to Figure 4.1(b). The material orientation of the stack-up can shortly be written as $[90/0_{15}]_s$.
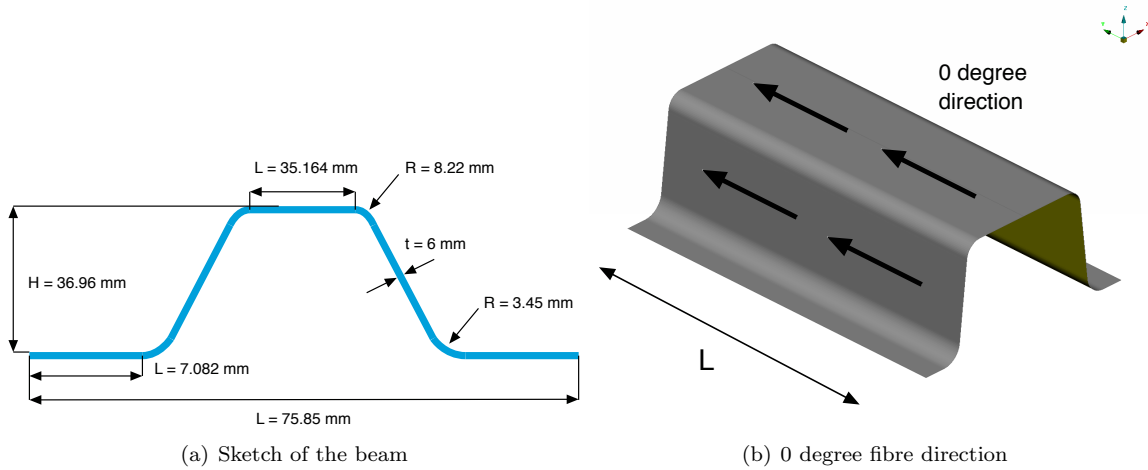

(a) Sketch of the beam

(b) 0 degree fibre direction

Figure 4.1: Schematic view of the cross section of the beam with dimensions, and 0 degree fibre direction.

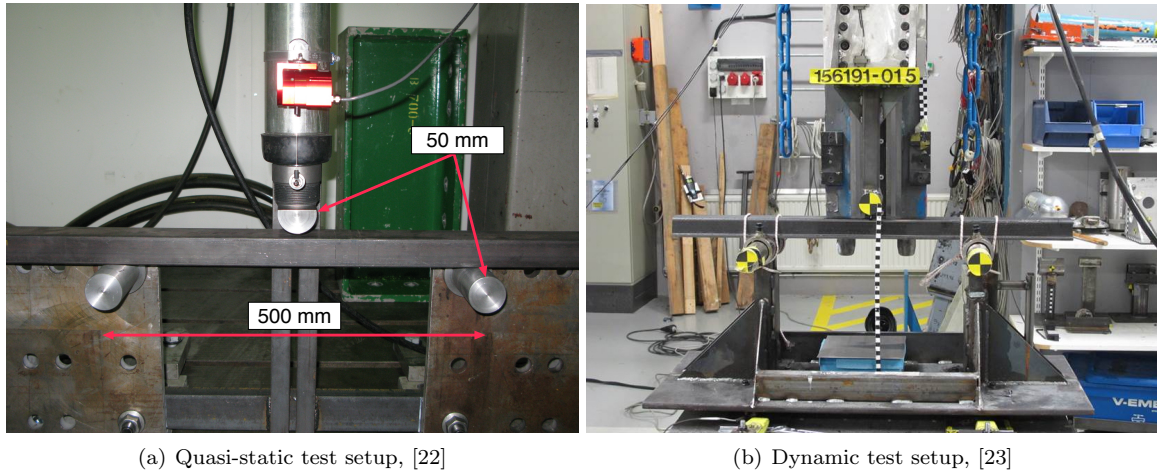(a) Quasi-static test setup, [22]

(b) Dynamic test setup, [23]

Figure 4.2: Test setup of the three-point bending of the composite beam.

In the dynamic tests, the impactor was released from different heights resulting in impact velocities between 5-10 m/s. The weight of the impactor was 24 kg and the force was measured in the support rig. The quasi-static test was performed using an average velocity of 3.6 mm/s of the impactor. The force was measured from a sensor located at the impactor. The relation between the measured force and the displacement of the impactor was established in a force-displacement curve which often is of interest in crash analyses. Especially since the energy absorbed can easily be obtained by evaluating the area under the force-displacement curve.

The force-displacement relation for the quasi-static test is shown in Figure 4.3(a) for four separate tested beams. As can be seen, all the tests follows the same tendency where a force peak was seen at a displacement

of approximately 8 mm followed by a significantly decrease in the force. However it can be seen that the test using specimen 2a gave generally a lower force response compared to the other tests. In addition, specimen 2b gave a slightly higher force response. This is explained by the fact that specimen 2a had two less 0 degree plies compared to the other specimens. Furthermore, specimen 2b had two additional 0 degree plies compared to the other specimens.

The absorbed energy was calculated as the area underneath the force-displacement curve and the corresponding energy-displacement relation is illustrated in Figure 4.3(b). It was observed that the same tendency can be seen as in the force-displacement relation: specimen 2a absorbs least energy and 2b absorb the most energy.

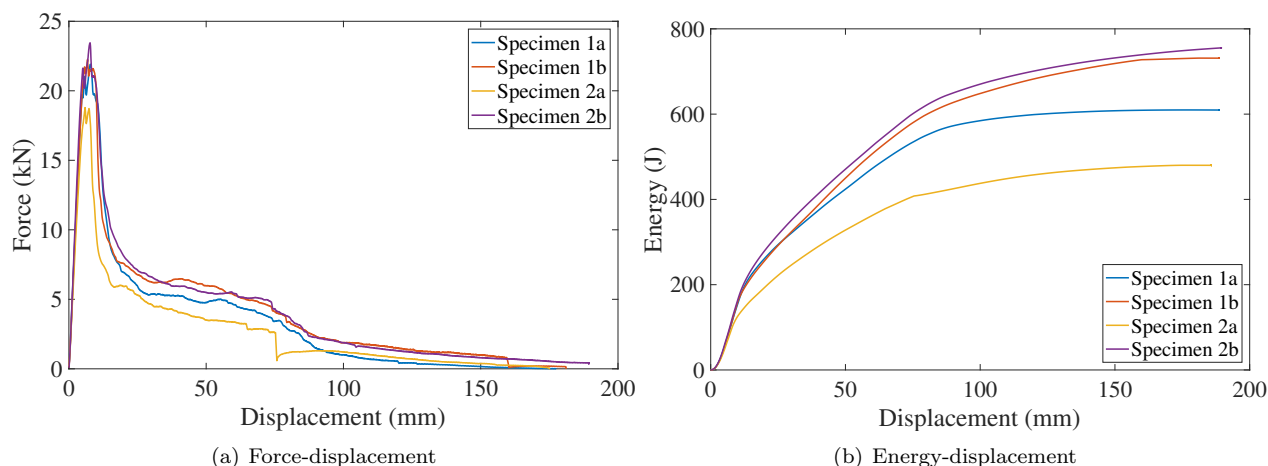(a) Force-displacement   (b) Energy-displacement

Figure 4.3: Experimental force-displacement results as well as energy-displacement results for the quasi-static testing.

For the dynamic test, the force-displacement relation for the different velocities are illustrated in Figure 4.4(a) where the mean of the quasi-static test also is included. In the experiment, one specimen for each velocity was used. As can be seen, the main trend is that the force peak is largest for the lowest velocity and is then decreasing as the velocity increases. However, the peak for the velocity of 8.15 m/s has lower force peak than for 9.85 m/s. Furthermore, the force peak also occur earlier for low velocities and as the velocity increases the peak occur for a larger displacement. It can be observed that the quasi-static test have a lower force peak compared to the test with $v = 5.01$ m/s and thus does not follow the trend of the increasing peak force. The corresponding energy-displacement relation for the dynamic tests are illustrated in Figure 4.4(b). It was observed that the energy absorption increased as the impact velocity increased except for the velocity of 8.15 m/s and the quasi-static test.

In the manufacturing it is documented that some deviations between the tested beams were seen both in density and thickness. Furthermore, two specimens were lacking fibre all the way out in the radius. These specimens were used for the dynamic tests with impact velocities of 9.85 m/s and 8.15 m/s. This may explain why the test with the velocity of 8.15 m/s deviated from the decreasing force peak trend seen in Figure 4.4(a). It may also be due to some difference in the test setup for this velocity.

In all tests it was observed that fracture only occurred close to the impact. The rest of the beam had a more or less elastic response where no fracture occurred. The zone where the fracture occur will henceforth be referred to as the fracture zone. In fractorgraphy, conducted by Swerea SICOMP, it was seen that this region was extended to around 10-20 mm away from the impact. However a more thorough investigation of the fracture has not been conducted. Thus which type of fracture that occur in the tests is in the present time unknown.
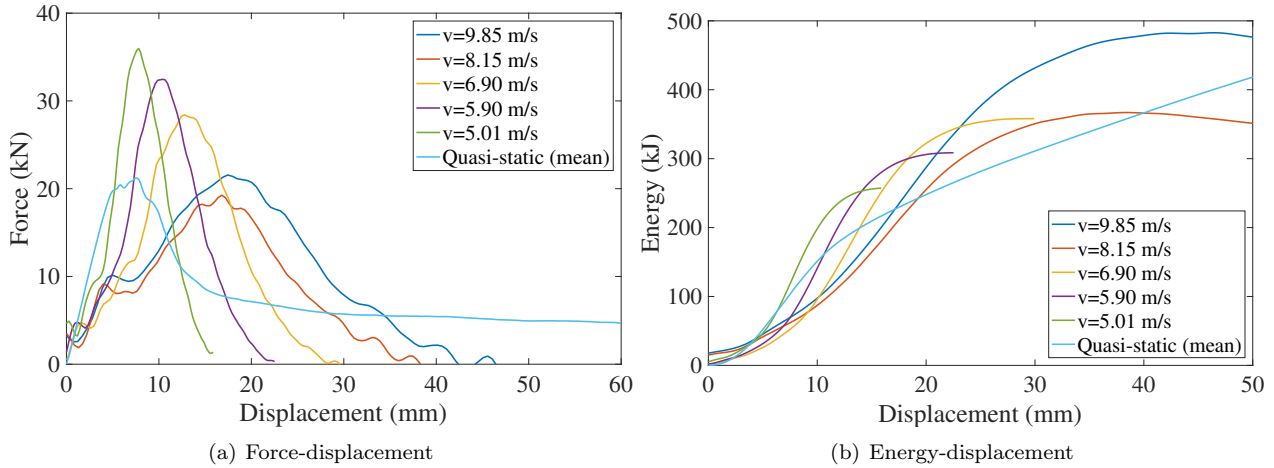
| (a) Force-displacement | (b) Energy-displacement |

Figure 4.4: Experimental force-displacement results as well as energy-displacement results for the dynamic testing.

4.3 Crushing of a corrugated specimen

In the study conducted by Costa [24] results from an experiment was presented for a corrugated specimen with dimensions according to Figure 4.5(a), with the impact diameter of 10 mm. The thickness of the specimen was 3 mm and the length was 50 mm. The test setup can be seen in Figure 4.5(b). In the test the specimen was loaded quasi-statically with an impact velocity of $v = 0.01$ mm/s. The composite material in the corrugated specimen is the same material as for the beam, described in Section 4.1. The plies within the material were cross ply oriented with 0 degree fibre direction altered with 90 degree having a total of 16 plies, which shortly can be written as $[0/90]_{4s}$. In the experiment, it was observed that cracks in the matrix occurred. It was also observed that delamination occurred in lower part of the specimen thickness, at the interface between a 0 and 90 degree plies. Furthermore, it was observed that no kinking occurred in fibre compression.

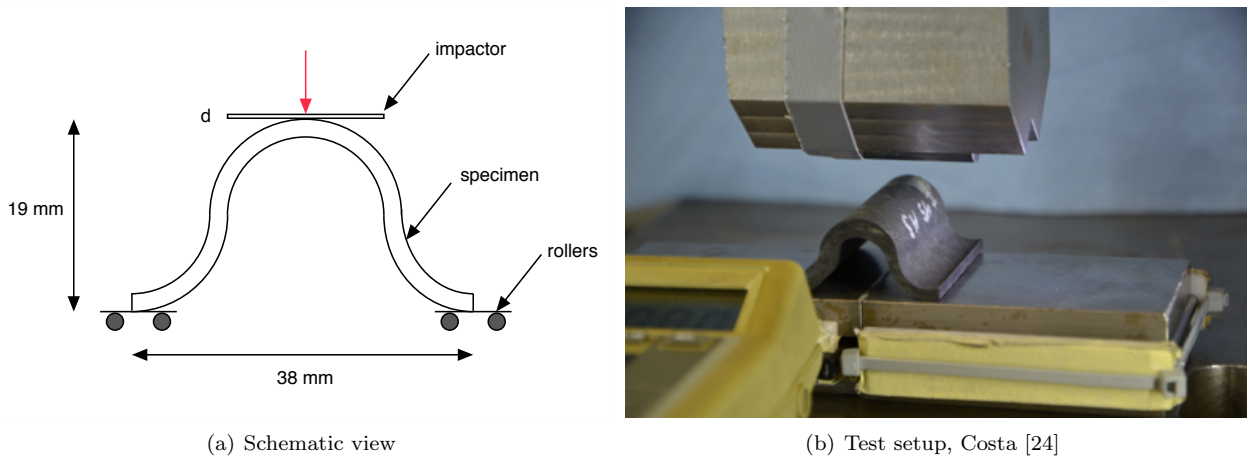| (a) Schematic view | (b) Test setup, Costa [24] |

Figure 4.5: Schematic view of the cross section of the corrugated specimen with dimensions as well as the test setup. The impactor diameter is $d = 10$ mm.

5 Verification and pre-investigation of material model implementation in LS-DYNA

In order to verify that SICOMP's material model gave the same response in LS-DYNA as in a previous study conducted by Costa [15], where ABAQUS was used as solver, a cube test was conducted. The cube, with a side length of 1 mm, was simulated quasi-static for different loading conditions, see Figure 5.1. The loading conditions investigated were tension and compression in fibre direction as well as transverse to the fibre direction. In addition to the verification of the material model developed by Swerea SICOMP, a comparison to material model MAT261 in LS-DYNA was conducted in order to see differences between the models. For these investigations LS-DYNA version R7.1.2 with share memory parallel processing (SMP) using single precision were used.

The main setup of the test can be seen in Figure 5.1. The left surface nodes were constrained such that the displacement was prevented in the loading direction. Furthermore, all displacements and rotations were prevented in the lower vertex node. The boundary conditions were implemented using BOUNDARY-SPC. The applied strain was modelled using a prescribed displacement of the right surface nodes. The displacement was prescribed linearly from zero to 0.1 mm, which corresponds to 10% strain, during 0.1 seconds. The prescribed displacement was implemented using BOUNDARY-PRESCRIBED-MOTION.
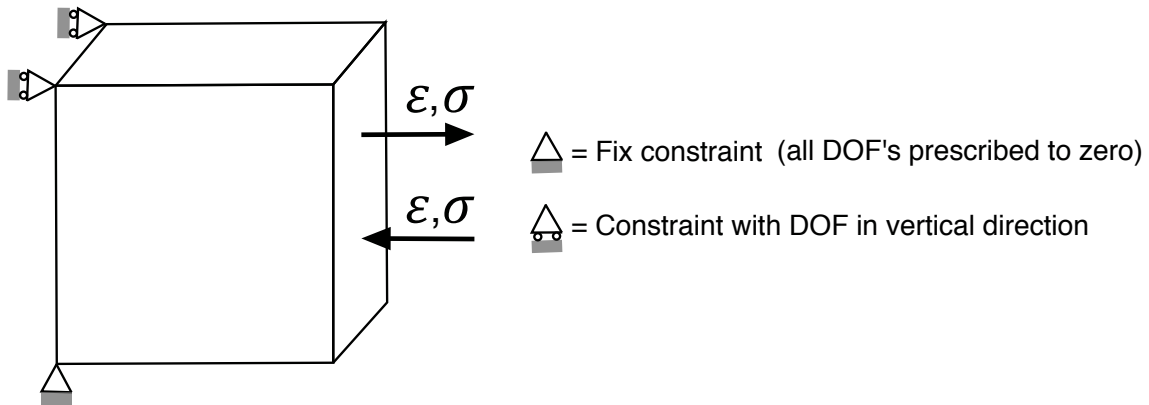

Figure 5.1: A schematic cube model where the boundary conditions as well as applied strain is illustrated.

The material parameters used Costa's study can be seen in Table 5.1 [15]. In order to verify the results to Costa's study it was required to use the same material parameters in this verification. The density used was $\rho = 1.6 \cdot 10^{-9}$ ton/mm^3. These material parameters differ from the parameters presented in Table 4.1. This since the material characterisation investigation conducted by Bru et al. [25] was performed after Costa's study was conducted.

The mesh dependence of the model was investigated for each load case by increasing the number of elements through the thickness from one to two elements. Consequently the number of elements were altered from one to eight elements as can be seen in Figure 5.2(a) and Figure 5.2(b). Costa's study [15] indicated that for matrix compression softening occur of all elements through thickness and thus twice the energy was absorbed. Hence, Costa suggested that only one element through thickness in the loading direction should be used for this loading case in order to get the desired energy absorption. This implied that the number of elements decreased to four elements, see Figure 5.2(c). With this reasoning the matrix compression case in the present study was modelled in the same way. However, this material model is restricted to only be discretised using one element through the thickness in a ply. This since when using more elements through the thickness of the ply, the model overestimates the absorbed energy.

Pinho et al. [5] described that the characteristic length should be the volume of the element divided by the area of the fracture plane. In practice, this means that the scaling of the fracture energy density needs to be performed with respect to the angle between the fracture plane and the element sides. However, this is not done in the SICOMP model. Instead, a scaling is made along the assumption that the normal to the fracture

Table 5.1: Material parameters for HTS45/LY556 used in the verification of SICOMP's material model.

Elastic properties				
Modulus			**Poisson's ratios**	
E_{11} (MPa)	E_{22} (MPa)	G_{12} (MPa)	ν_{12} (-)	ν_{23} (-)
136000	9150	4900	0.29	0.4
Strength properties				
	X_t (MPa)	Y_t (MPa)	S_L (MPa)	
	1787	29	40	
	X_c (MPa)	Y_c (MPa)	S_T (MPa)	
	626	130	60	
Friction properties				
Internal pressure		**Coefficient of friction**		
p_{0L} (MPa)	p_{0T} (MPa)		μ_L (-)	μ_T (-)
75	30		0.32	0.32
Fracture toughness				
Interlaminar				
$G_{Ic}(kJ/m^2)$			$G_{IIc}(kJ/m^2)$	
0.149			0.69	
Intralaminar and translaminar				
$G_c^{ft}(kJ/m^2)$	$G_c^{fc}(kJ/m^2)$	$G_c^{mt}(kJ/m^2)$	$G_{IIc}^{mt}(kJ/m^2)$	$G_{IIc}^{mc}(kJ/m^2)$
50	25	0.222	1.92	1.92

plane is always in the loading direction which for matrix compression leads to an error of approximately 40% in the characteristic length. Since the elements in matrix compression no longer will be cubic the calculation of the characteristic length needs to be investigated. Since the fracture plane assumes to be orthogonal to the loading the characteristic length is consequently based, from the relation between the volume of the element and the fracture area, on the longest side of the element. However, the element length LS-DYNA calculate is the shortest side length of the element and thus for a fair comparison, the characteristic length should be twice the element length calculated by LS-DYNA.

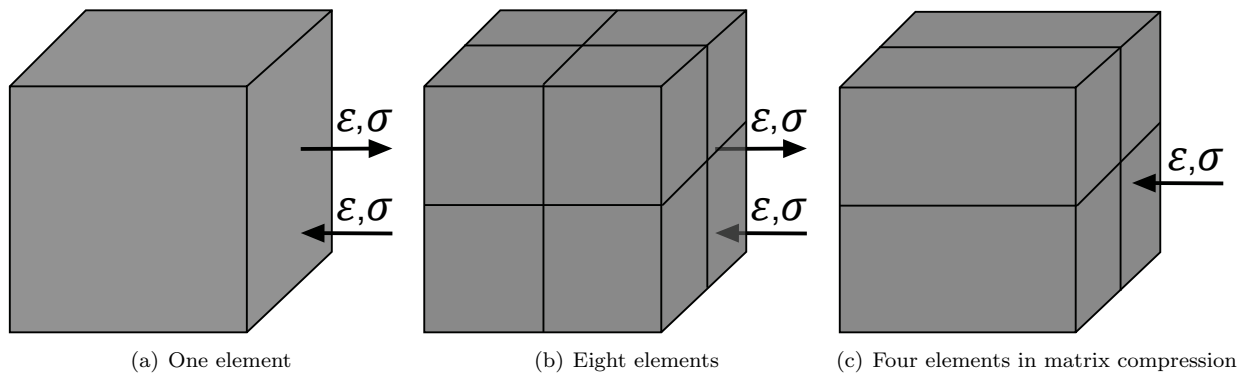(a) One element   (b) Eight elements   (c) Four elements in matrix compression

Figure 5.2: The discretisation of the cube for one and two elements through the thickness as well as the special case for matrix compression.

Furthermore, the characteristic length of the elements is calculated differently in ABAQUS and LS-DYNA. In ABAQUS, the characteristic length is determined at the initial time step and preserved during the simulation. In LS-DYNA, it is instead updated for each time step throughout the simulation. In order to give a trustworthy comparison between the softwares, the characteristic length was manually defined as the initial length of the elements inside the implementation of the material model. However this was not used in the comparison between SICOMP's model and MAT261 since both these simulations were computed in LS-DYNA.

For all cube analyses, the stress-strain relation was calculated as well as the internal, kinetic and artificial energy. The stress was calculated from the nodal forces at the surface where the displacement was applied. The nodal force output was achieved by using the keyword DATABASE-NODFOR together with DATABASE-NODAL-FORCE-GROUP where the set of nodes, for which the force output should include, were defined. The sum of these forces were then divided by the initial cross section area of the cube which gave the stress. The strain used in the stress-strain relation was the engineering strain, i.e. the end displacement divided by the initial length of the cube in the loading direction. The kinetic energy was studied in order to make sure that the simulations were quasi-static.

In LS-DYNA different hourglass formulations can be used by adding the CONTROL-HOURGLASS keyword. In order to investigate which hourglass formulation that should be used an investigation was performed, see Appendix A. It was seen that the stiffness based formulation using exact volume integration and a hourglass coefficient of 0.05 was the one giving the best behaviour. Furthermore, for anisotropic materials it is recommended to use invariant node numbering, [26]. This was added by the CONTROL-ACCURACY keyword with the parameter $INN = 4$.

5.1 Verification of SICOMP's model

In this section, the results for the verification of the material transfer from ABAQUS to LS-DYNA is presented. The results are presented for simulations carried out in ABAQUS and in LS-DYNA using one and eight elements. However, in matrix compression only four elements were used in accordance to Chapter 5. In the presented results ABAQUS is abbreviated to Abq and LS-DYNA to Dyna.

5.1.1 Fibre tension

The subsequent figure, Figure 5.3, illustrates the stress-strain relation for fibre tension in the cube analyses. The results indicates that the obtained stress-strain relation using LS-DYNA corresponds well with the reference response using ABAQUS. A deviation in the strain where final damage occur can be seen.
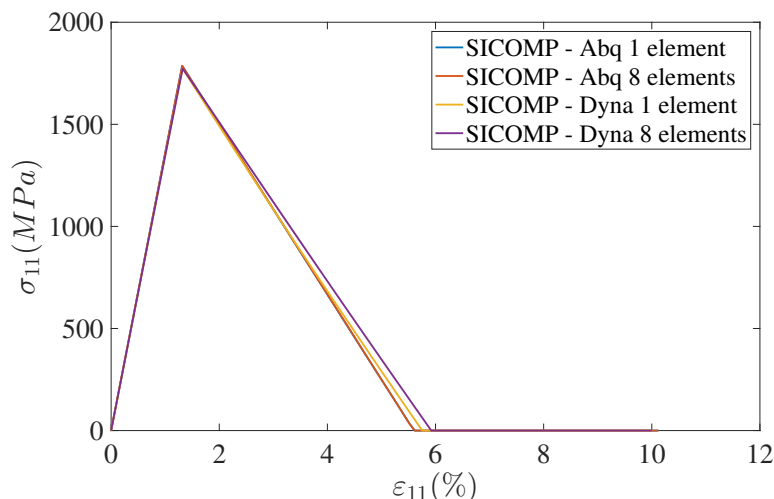

Figure 5.3: Stress-strain response in fibre tension for the verification of SICOMP's model.

5.1.2 Fibre compression

For fibre compression, see Figure 5.4(a), the stress-strain relation corresponds well for one element. However, when using eight elements the response in LS-DYNA is deviating as the strain reaches $\varepsilon_{11} = 3.2\%$ and becomes unstable. For the corresponding load case it was seen in the results that the artificial energy and the kinetic energy increased when the strain reaches $\varepsilon = 3.2\%$, see Figure 5.4(b).
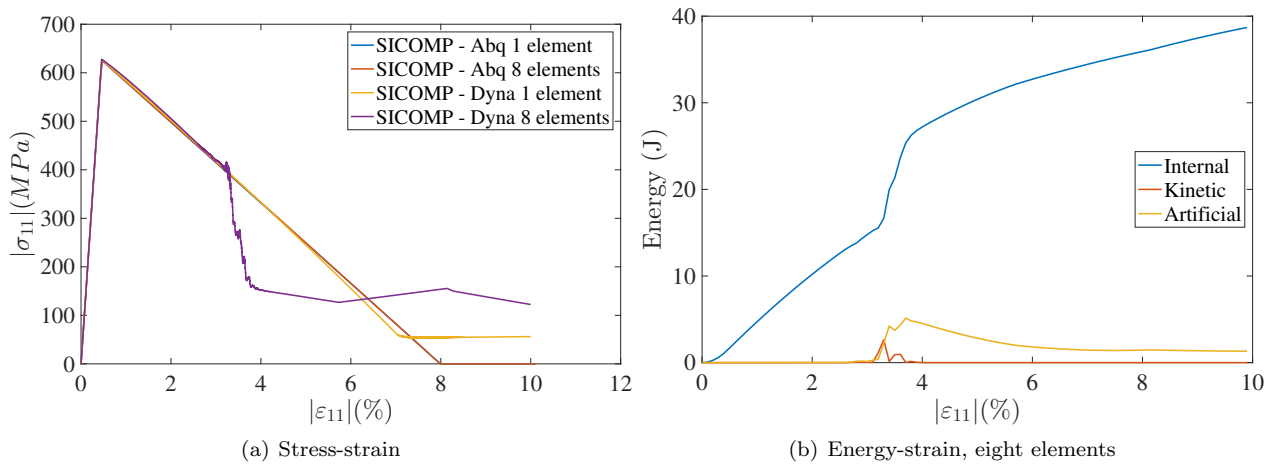
(a) Stress-strain

(b) Energy-strain, eight elements

Figure 5.4: Stress-strain response in fibre compression for the verification of SICOMP's model.

5.1.3 Matrix tension

Figure 5.5 shows the obtained results for matrix tension. The stress-strain relation, Figure 5.5(a), corresponds well with the reference response from ABAQUS. For the eight element cube some instability appears at $\varepsilon_{11} = 1.6\%$ and the simulation terminated when the strain reached $\varepsilon_{11} = 1.9\%$. It was also seen that the artificial energy increased at a corresponding strain, see Figure 5.5(b). However, since this appear after fully damage has been obtained the sudden termination has no influence on the results.
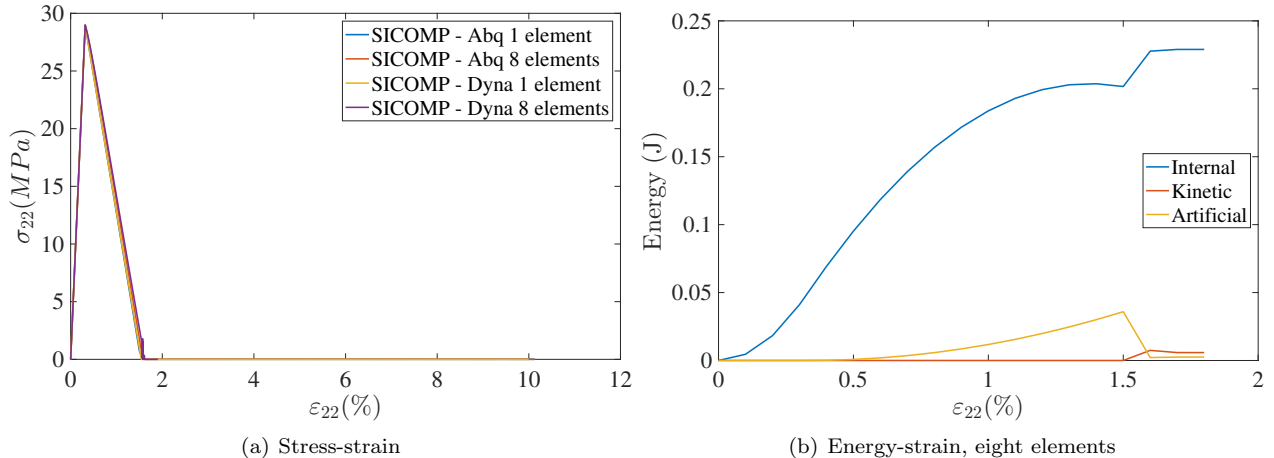

(a) Stress-strain

(b) Energy-strain, eight elements

Figure 5.5: Stress-strain relation in matrix tension as well as the energy-strain relation for the verification of SICOMP's model.

5.1.4 Matrix compression

For matrix compression it was observed that the results obtained from LS-DYNA corresponded well with the results from ABAQUS, see Figure 5.6. From the results it is possible to see that even though fully damage has been reached, the model is still capable of carrying load. This corresponds well with the underlying theory for this load case, when a combined friction and damage model is used, as described in Section 2.2.3.
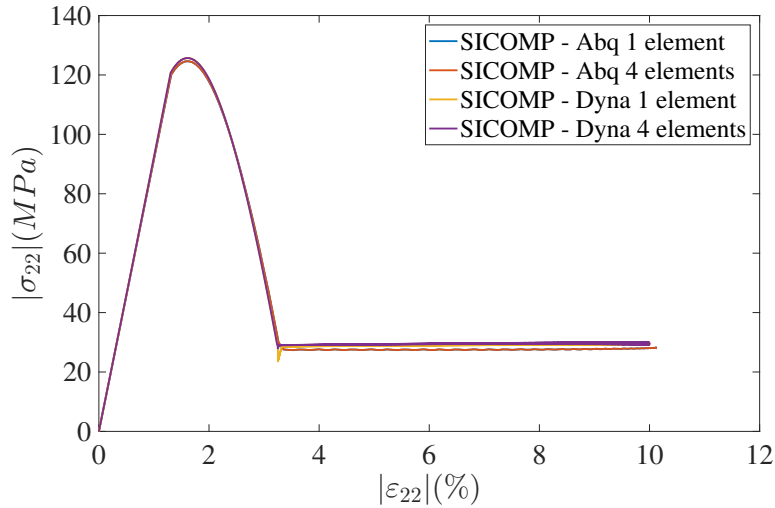
Figure 5.6: Stress-strain relation in matrix compression for the verification of SICOMP's model.

5.1.5 Discussion

As can be seen in the results, final damage is reached later in LS-DYNA for loading in fibre tension compared to ABAQUS. The deviation may be explained due the difference in how the strains were calculated between the two softwares used. In ABAQUS, the strains were calculated using the approximation of small deformations, whilst LS-DYNA always calculates the strains assuming large deformations. Another observation that may explain why the results in fibre compression and matrix tension deviates for eight elements can be found when studying the energies. At the strain levels where the results starts to deviate, an increase in the artificial energy as well the kinetic energy can be seen. The ratio between the artificial energy and the internal energy reaches 21% and 18% for fibre compression and matrix tension, respectively. This indicates that the results are unreliable since the ratio is above 5% [15]. In matrix tension, the solution is terminated after this peak in artificial energy.

5.2 Benchmarking

In this section a comparison between SICOMP's material model and MAT261, which is an already implemented material model in LS-DYNA, will be presented.

5.2.1 Fibre tension

Figure 5.7 shows the obtained stress-strain when loaded in fibre tension. It can be observed that the response is similar between the two material models. A small deviation when final damage occur can however be seen using one element.
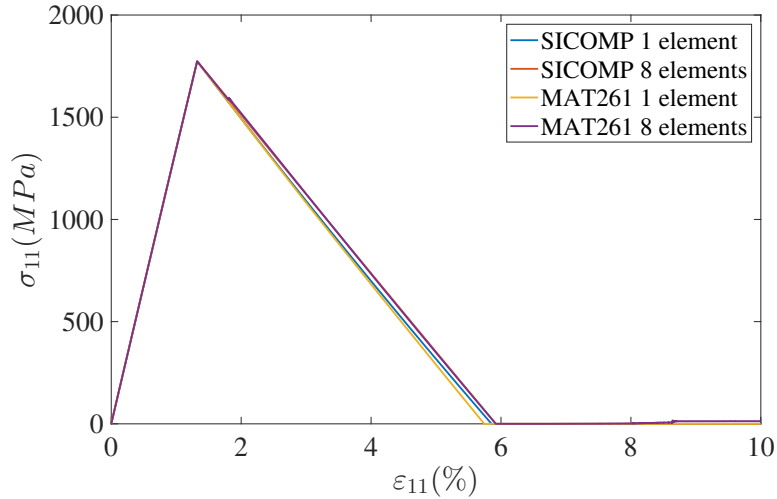

Figure 5.7: Stress-strain relation in fibre tension in the benchmark investigation.

5.2.2 Fibre compression

In fibre compression it can be observed that the responses was similar to each other until a strain of 3.2% is reached, see Figure 5.8. When the strain increased further the results starts to deviate, especially for eight elements. Final damage is not reached in neither cases. With MAT261, the artificial energy increases when strain reaches $\varepsilon = 4.5\%$ and oscillates around 0.2J, see Figure 5.9(a). As the strain reaches 7.5% the ratio between the artificial energy and the internal energy increases to a value of 28%. With SICOMP's material model, the artificial energy increases when strain reaches $\varepsilon = 3.2\%$, see Figure 5.9(b). The increasing trend reaches a threshold around $\varepsilon = 4\%$ where it afterwards decrease.

5.2.3 Matrix tension

Figure 5.10 shows the stress-strain response when a tensional loading, transverse the fibre direction, was applied. The response using one element was similar between the two material models. With SICOMP's material model using eight elements the simulation terminated when the strain reached $\varepsilon = 1.9\%$. In addition to that, an unstable behaviour can be observed with MAT261 when the strain reaches $\varepsilon = 5\%$ using eight element discretisation. However, none of these unstable behaviours should have any influence on the accuracy of the results since these behaviours occur after fully damage has been reached.

5.2.4 Matrix compression

In matrix compression, the results deviates between the two material models under consideration, see Figure 5.11. The material response, with MAT261, follows a bilinear damage response where no load carrying capability

Figure 5.8: Stress-strain relation in fibre compression in the benchmark investigation.

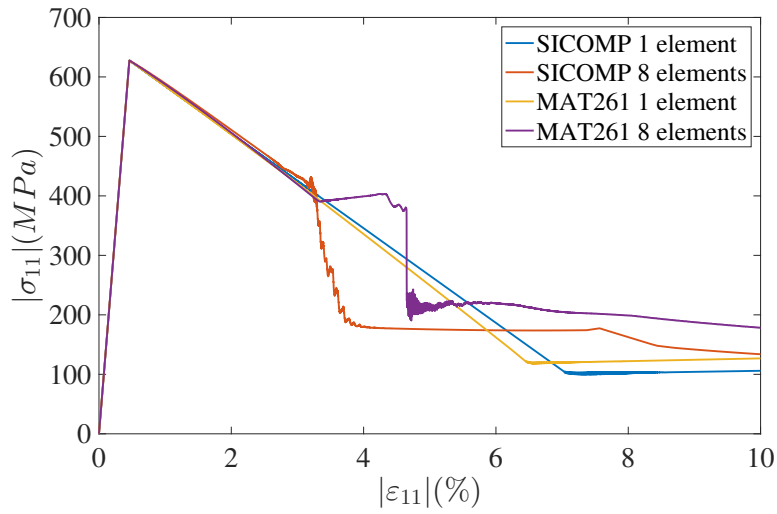(a) MAT261, eight elements
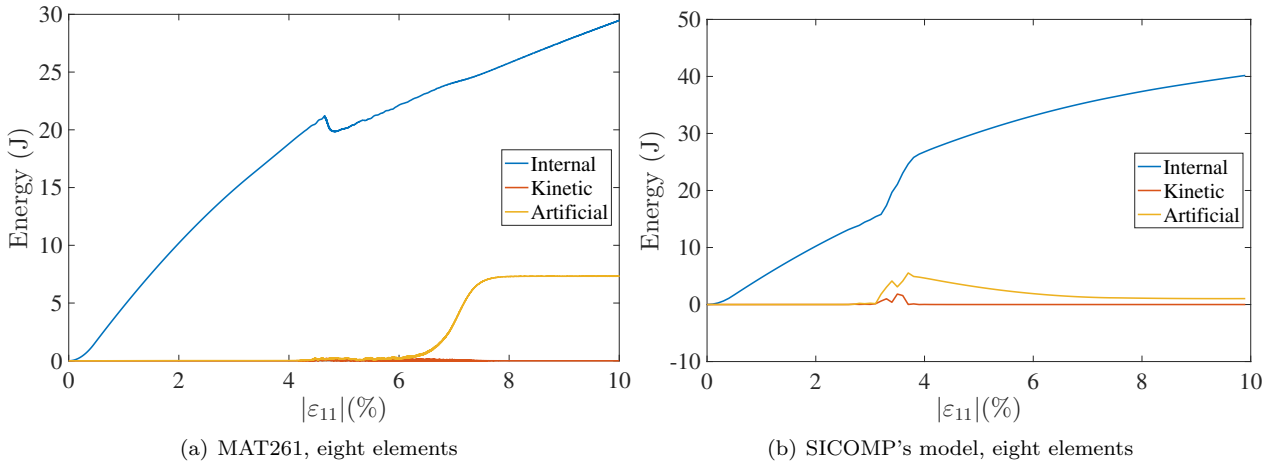

(b) SICOMP's model, eight elements

Figure 5.9: Energy-strain relation in fibre compression in the benchmark investigation.
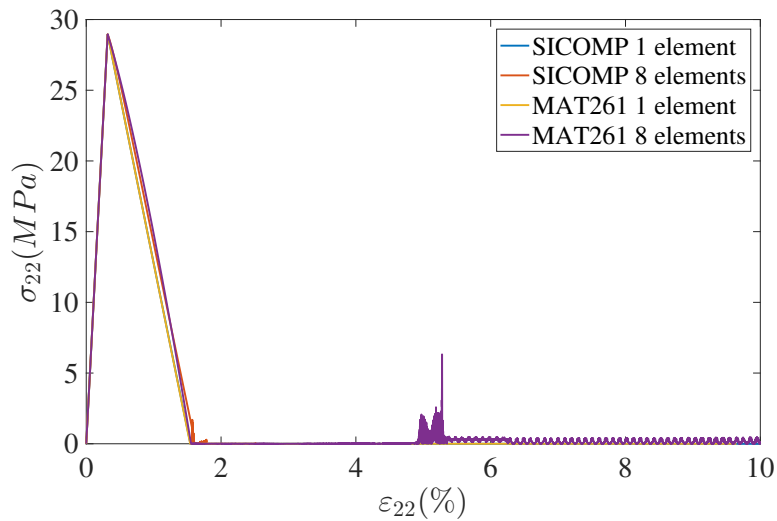

Figure 5.10: Stress-strain relation in matrix tension in the benchmark investigation.

remains after final damage has been reached. However, SICOMP's material model has a non-linear softening response after initial failure has been reached. Furthermore, the elements are still capable of carrying load after final damage has been reached.
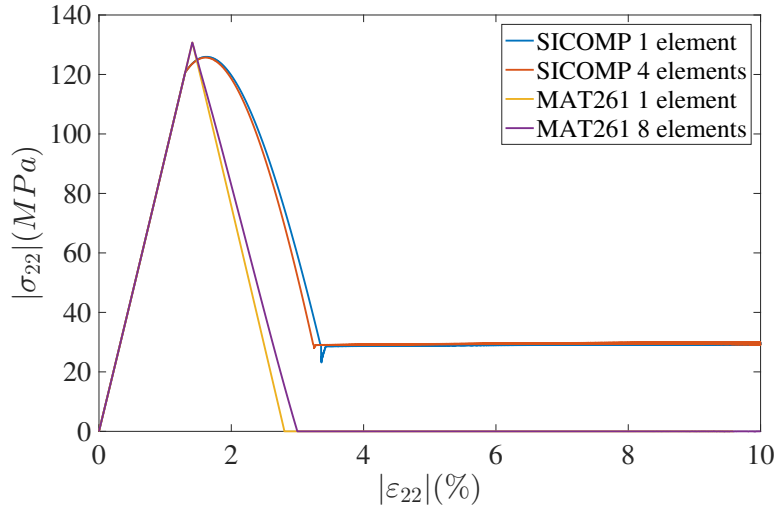

Figure 5.11: Stress-strain relation in matrix compression in the benchmark investigation.

5.2.5 Discussion

As can be seen in the results from this benchmarking study the stress-strain response in fibre tension are similar between the two models under consideration. In fibre compression, the deviation between the models using eight elements is more pronounced. However, the deviating behaviour seems to arise due to numerical issues, rather than differences between material models. This since the artificial energy is increasing at the strain where the deviation occur. When loading transverse the fibre direction in tension, similar behaviour was observed in the stress-strain response. Finally, when loaded in matrix compression, it can be seen that both the material models gave a stress-strain response accordingly to the corresponding material theory. Thus the difference in this load case only highlights the differences in damage evolution in these models. In this load case MAT261 follows a bilinear law, whilst SICOMP's model has a nonlinear softening behaviour after initial damage.

As stated earlier some numerical problems occurred in fibre compression. After consultation with DYNAmore Nordic it appeared that the strong orthotropy in the material may be the source of the numerical problems. The suggestion was to change the strength parameters such that the material response was less orthotropic. However, since the verification was carried out by comparing to already conducted FE-results using these material properties, this was not applicable.

5.3 Conclusions

In the verification of SICOMP's model it was seen that the overall response corresponded well with the reference results from ABAQUS. However, the material response deviated when loaded in fibre compression where final damage was not reached.

In the benchmarking study it was seen that when loaded in fibre tension and matrix tension, the same response was obtained for both material models under consideration. In fibre compression both models initially had the same response. However, when the displacement increased the response deviated between the models, especially in the eight element case. The difference between the material response, for matrix compression, highlights the the differences in damage evolution in these models.

6 Modelling approach for benchmarking components

In this chapter the modelling approach for the three-point bending of a beam, as well as crushing of a corrugated specimen, will be presented.

6.1 Beam test

The section describes the method for building the beam model, followed by parameter investigations of the contact friction between the beam and the supporting cylinders. Furthermore, the section also covers an investigation of the dynamic effects when varying the length of the beam. Additionally, a solid to shell transition investigation will be carried out.

6.1.1 Simulations approach

The simulations approach of the beam was to initially run simulations for a solid uniform beam model, discretised with only solid elements. Having the solid uniform beam as a reference model, an investigation whether a transition from solid elements to shell elements could be utilised, was conducted. This in order to reduce the computational costs. If the solid to shell transition could be used, an investigation of how delamination failure mechanisms affect the results was carried out. This by adding cohesive element zones in the intersection between plies with different fibre directions. Otherwise the solid uniform beam model was used for this investigation.

6.1.2 The FE-model

In this section the setup of the FE-model of the beam is presented. For this model LS-DYNA version R8.1.0 with Massively Parallel Processing (MPP) using double precision were used if nothing else is stated. The same material parameters for the NCF composite material HTS45/LY556 was used as in the experimental test as was described in Chapter 4 and can be seen in Table 4.1. The density used was $1.51 \cdot 10^{-9}$ ton/mm^3. Both the impactor and the supports were assumed to be made of a soft steel with $E = 210000$ MPa, $\rho = 7.85 \cdot 10^{-9}$ ton/mm^3 and $\nu = 0.3$. The steel material was modelled using an elastic material model as long as the stresses was below the yield strength of $\sigma_y = 350$ MPa.

Geometry

The setup of the beam was modelled as close to the experimental setup as possible. This resulted in the model which can be seen in Figure 6.1. For simplification only the supporting cylinders were modelled instead of the whole testrig. This simplification excludes the inertia of the rig which for the dynamic test may give some effects on the result. However, it was assumed that this effect is minor. Furthermore, the impactor was for simplicity modelled as a cylinder with the same mass, which is the geometry in contact with the beam. The velocity of the impactor was prescribed using an initial velocity of 5.9 m/s in the dynamic test. This velocity was chosen since it was observed from experiment that significant damage occurred in the beam without breaking it in two.

Since the geometry have double symmetry planes the model only needs to consist of a quarter of the beam. The same symmetry was used for the impactor in order to minimize the number of elements and thus only a quarter of the impactor was modelled. In the symmetry planes, the displacement in the normal direction was prescribed to zero. For the shell elements the rotations in the in plane axis were additionally prescribed to zero. When applying symmetry to the model the contact area between the beam and the support was reduced by a factor of two. Since the stress state was preserved this implies that the reaction force also would decrease by the same amount. With the same reasoning, with double symmetry the reaction force was decreased by a factor of four in the contact between the beam and the impactor.
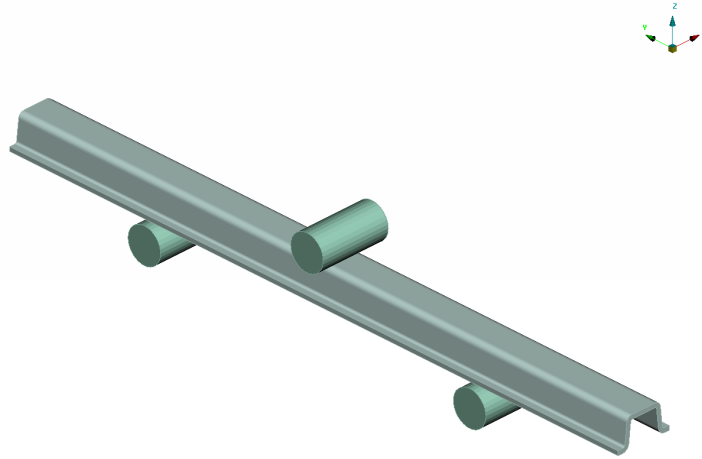
Figure 6.1: The modelled beam including the two supporting cylinders underneath and the impactor in the middle of the beam.

Discretisation

To assure that the possible differences between FE results and experimental tests originates from the material model and not the discretisation, discretisation dependencies should be minimised. Only the solid element formulation captures 3D stress state in a correct way, see Section 2.1.3, and thus solid elements was used in the discretisation. As indicated before, due to the energy density scaling, SICOMP's model is only valid for elements with an aspect ratio of one which implies that the fracture zone needs to be modelled using cubic solid elements. In addition, the beam consists of 32 plies through the thickness and since each ply should be resolved using at least one solid element, in order to be able to capture delaminations, the mesh becomes very dense. However, it is only the fracture zone which is needed to be discretised using this refined mesh. This because the rest of the beam has an elastic response and thus no fracture occur, see Section 4.2. Since the fracture zone was expanded about 20 mm from the impact in the experimental test it was chosen that the fine discretisation should be used in a region of 30mm around the impact. The support was modelled using a shell mesh in order to have a smooth contact without unnecessary additions to the cpu time. Furthermore, the impactor was modelled using solid elements with a refined mesh closest to the impactor surface.

In order to efficiently add the ply stack-up in the discretisation, the LAMINATE TOOL in ANSA was used. This was performed by initially creating a laminate property and assigning the meshed region to this property. The next step was to open the AUXILIARIES-LAMINATE TOOL in the LS-DYNA DECK and in the created laminate define the number of plies and their fibre orientation, the desired material and the thickness of each ply. The same procedure can be used for both solid and shell elements. The main difference is that the assigned property needs to be either a SOLID LAMINATE or a SHELL LAMINATE depending on the choice of element. In addition, for a SOLID LAMINATE the stacking needs to be changed to "per ply". It is of importance to only have one solid element through the thickness before changing the stacking to "per ply". This since when the stacking is changed to "per ply", the stack-up is repeated for each element. Furthermore, the element orientation of the solid elements determines in which direction the stack-up is growing and it is of importance to make sure that this orientation is in the desired direction. The element orientation can easily be changed using the ELEMENT-SOLID-ORIENT FACETS function in the LS-DYNA DECK in ANSA.

Boundary and Contact Conditions

All the degrees of freedom for the cylindrical supports were fixed using the boundary condition BOUNDARY-SPC in LS-DYNA. The impactor was set to only be able to move in the z-direction, which is the direction of the impact. For the dynamic case, an initial velocity of 5.9 m/s on the impactor was prescribed.

The contact condition between the circular supports and the beam, as well as the contact condition between the impactor and the beam, were defined in similar ways. The contact condition used was CONTACT-AUTOMATIC-SURFACE-TO-SURFACE in LS-DYNA, with the beam set to slave. The static friction coefficient in the connection to the support was unknown and consequently a handbook value between epoxy and steel of $\mu_s = 0.4$ was assumed according to Grahn et al. [27]. However a parameter study was performed, as can be found in the next section, in order to see what effects the friction coefficient have on the results. For the contact, the soft constraint formulation is recommended to be used when large difference in elastic bulk modulus between the materials in contact occur [26]. Thus, this parameter was set to SOFT=1. Furthermore a viscoelastic damping coefficient, VDC, was used with 20% [26].

Improving simulation accuracy

In order to improve the solution precision, the additional flag OSU in the card CONTROL-ACCURACY where used for the beam. With this flag active, a so-called 2nd order objective stress update is enabled. This increases the accuracy of the calculation and it is also recommended from DYNAmore if problems with negative volumes is present or elements undergoing large rotations [26]. If an element loses the contact to the rest of the model due to deletion of fully damaged elements these elements may undergo unphysical deformations and rotations. Having OSU active helps the simulation to deal with these loose elements.

Delamination

In order to include the interlaminar behaviour in the solid uniform beam model, 8 node cohesive elements were used in accordance to the theory in Section 2.1.3. The participants in the project group had more experience of this technique compared to the tiebreak criterion. Since interlaminar behaviour may occur between plies which have different fibre directions the cohesive elements were applied between the 0 and 90 degree plies. The 8 node cohesive elements were added using the LAMINATE TOOL in ANSA. The thickness of the cohesive elements was set to zero. The model was then exported to a key file and then re-imported to ANSA without including the ANSA comments. This resulted in that each ply and cohesive element had separate part id's and thus it was possible to set separate element formulation for them. The element formulation for the cohesive elements was set to ELFORM 19 since this is the only cohesive element formulation which can be used for solid elements. In order for the elements, which have a cohesive element in between them, to have contact after the cohesive element was deleted, a contact condition was added. The contact condition used was CONTACT-ERODING-SURFACE-TO-SURFACE.

6.1.3 Pre-study and setup analysis

In order investigate how different parameters influence the result, parameter investigations of the contact friction between the beam and the supporting cylinders and the dynamic effects when varying the length of the beam were carried out.

The investigation of these features were conducted using a linear elastic perfectly plastic isotropic material model in order to simplify the model. Furthermore, the mesh used was a solid mesh with a fine mesh at the impact zone which then successively is increased in size further out. The area of which the elements were kept cubic was defined to be 50 mm from the impactor. In this area an element length of 2 mm was used. The number of elements through thickness was set to four. An increase of the element length was such that the elements in the end of the beam was four times larger than in the area where cubic elements were used.

For all the studies in this section, a linear elastic ideally plastic material model was used with $\rho = 1.51 \cdot 10^{-9}$ ton/mm^3 (which is the same density as for the NCF material), $E = 210000$ MPa and $\sigma_y = 235$ MPa. For these investigations LS-DYNA version R7.1.2 with Shared Memory parallel Processing (SMP) using single precision were used.

Contact condition - Friction coefficient

The contact condition parameter investigated was the static friction between the steel supports and the beam. This since the value on the static friction coefficient is unknown and thus the impact of the chosen handbook value of $\mu_s = 0.4$ needed to be investigated. The investigation was performed by altering the frictional coefficient between 0 to 0.5 with an interval of 0.1 and the force-displacement relations were compared. This test was conducted using the impact velocity of 5.9 mm/s.

For a small increase of the static friction, from 0 to 0.1 and 0.2, a clear difference in the relation between the force and displacement was seen, as is illustrated in Figure 6.2(a). However, as the friction is further increased, the difference in response decreases. The results shows that the largest difference in response was for small values on the static friction coefficient. Furthermore, no significant difference in the response for frictions between 0.3 and 0.5 was seen, as also can be seen in Figure 6.2(b). This implies that even if the handbook value of $\mu_s = 0.4$ slightly deviates from the actual friction in the contacts in the performed test, the simulation results will not be effected.

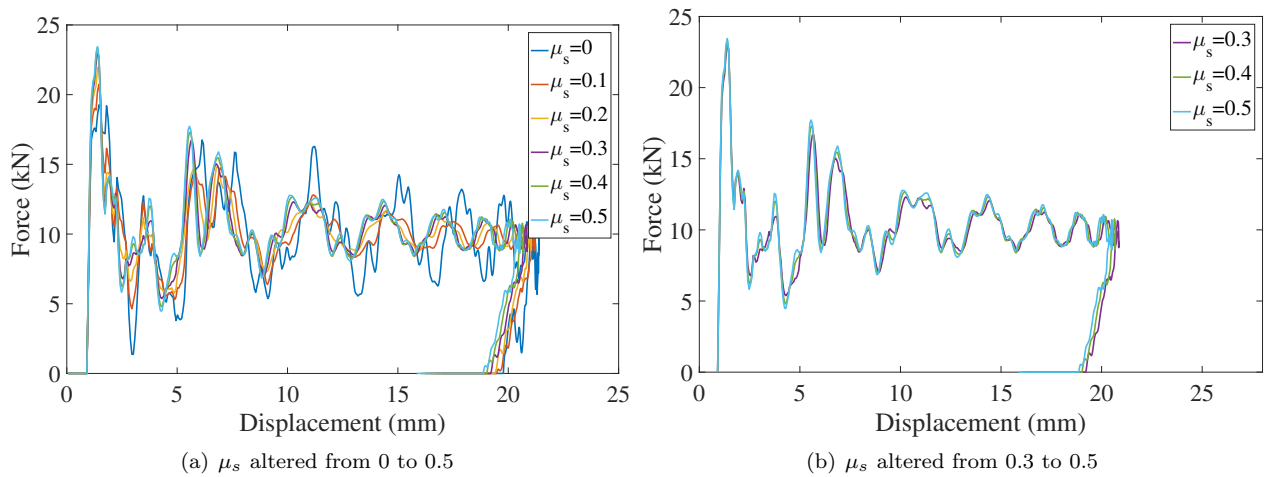(a) μ_s altered from 0 to 0.5   (b) μ_s altered from 0.3 to 0.5

Figure 6.2: The contact force in the support versus displacement of the impactor for different static friction coefficients in the contact between the beam and the supports.

Dynamic effects - length of beam

In order to investigate how the dynamic response of the beam is influenced by the sections of the beam outside the supports, different lengths of the beam were examined. The parametrised length was stepwise altered from the actual length of the beam, to a length just exceeding the distance between the impactor and the support. In order to make sure that the investigation included dynamics of the structure, the impact velocity was fixed at 5.9 m/s.

The relation between the force and displacement for different lengths of the beam is illustrated in Figure 6.3 where the decrease of the beam length is presented in percentage. For a slight decrease in length it was observed that the response was initially quite similar. However, as the displacement of the impactor increased the frequency in the force peaks increased although the amplitude of the force peaks were preserved. For the case when the length was reduced further, the response is illustrated in Figure 6.3(b). It can be observed that both the amplitude as well as the frequency of the force peaks deviates from the force calculated using the original beam length. Since the beam reacts dynamically, the deviation in the response should be due to the change in mass and thus inertia of the beam. As a concluding remark, the length of the beam influence the dynamics of the beam. Consequently, the entire beam needs to be included in the FE-model in order to capture the correct dynamical behaviour of the beam.
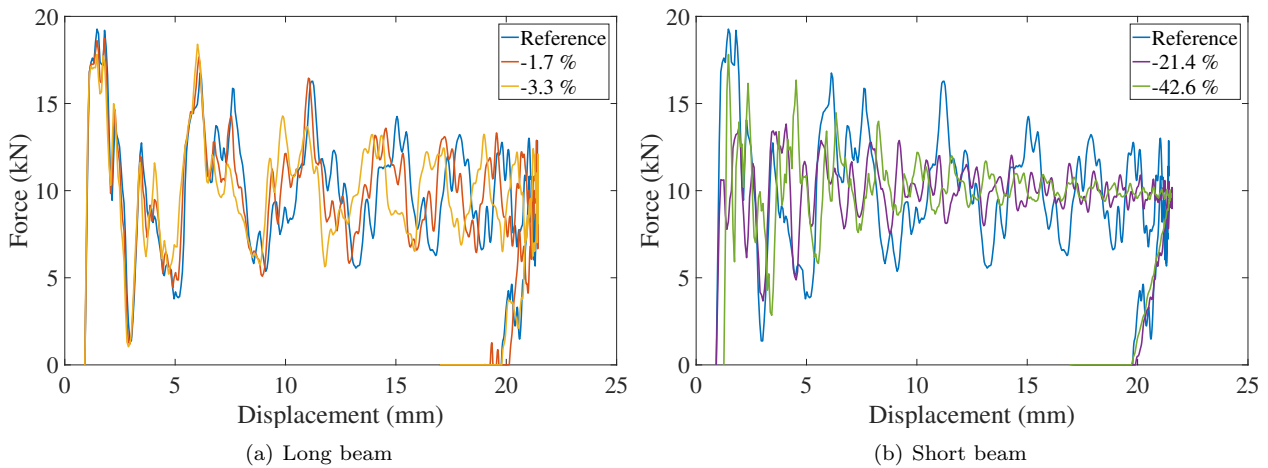
(a) Long beam

(b) Short beam

Figure 6.3: The contact force in the support versus displacement of the impactor for different lengths of the beam labelled in percentage of the original beam length.

6.1.4 Solid to shell transition

The main idea with having a transition from solid elements to shell elements is to reduce the computational costs of only having solid elements. In the solid nodes there are no rotational degree of freedom which the shell elements needs in order to transfer the bending in a correct way. The transition was determined to be applied outside the fracture zone at 30 mm which is just outside the refined mesh area. To minimise the simulation costs the mesh was successively made coarser further away from the solid to shell transition. This was obtained using the function SPACING in ANSA. The maximum ratio accepted were determined to be 10 which gave an element size of about 1.8 mm at the end of the beam.

In order to illustratively show the importance of this rotation an example of a cantilever beam can be considered which is split into two sections, see Figure 6.4. The beam is clamped in the innermost node and it is loaded with a force F in the outermost node. If the rotational degree of freedom is not coupled between node a and node b in a correct manner the transition will act as a joint, which is illustrated in Figure 6.4(a). However, if the rotational degree of freedom is coupled in a correct manner, between the two nodes the beam will act as a rigid beam, which is illustrated in Figure 6.4(b). In addition, the transition needs to preserve the energy balance as well as transfer stresses from the solids to the shells without any stress wave reflection in the transition zone. Two methods to fulfil these criteria will in this section be presented.
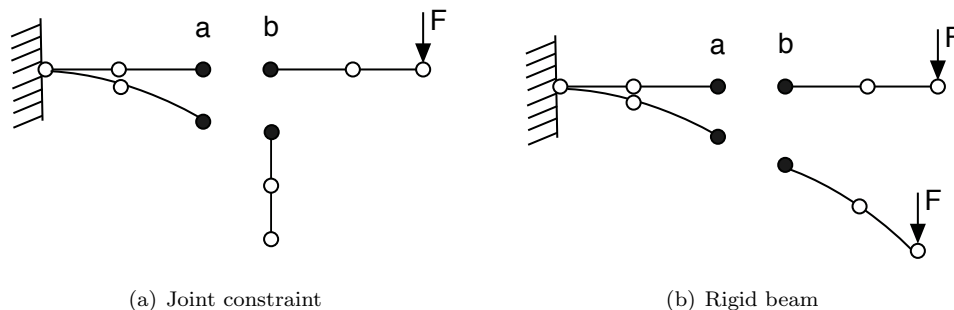

(a) Joint constraint

(b) Rigid beam

Figure 6.4: Illustration of two ways to constrain nodes.

Two investigations were conducted including both a three-point bending test, as well as an impulse test. For these investigations the same material model, with associated material properties, and the same discretisation as described in Section 6.1.3 were used. The three-point bending test was performed using the impact velocity of 5.9 m/s with the transition from solid to shell applied on a distance of 50 mm from the impactor.

In the impulse test a load was applied at the end of the shell. The test was conducted using the same geometry as in the three-point bending test, except that only the beam was included. A schematic illustration of this test can be seen in Figure 6.5. The representation of the impulse was modelled by adding a force with a trapezoidal load curve with the magnitude of 100N. The load was applied at t=1 ms and released at t=1.1 ms. The surface opposite to the edge where the load was applied was constrained using a fixed boundary condition. The impulse test was performed in order to make sure that no stresses or displacements were mirrored at the transition. In addition to that, the test was conducted to check that no energy losses occurred. If the transition managed to generate the desired physical behaviour, the transition was applied on the final model, which is described in Section 6.1.2. This in order to conclude if the transition worked for a composite material, using the material model MAT261, as well for a refined mesh. The results from this investigation can be seen in Section 7.1.2.
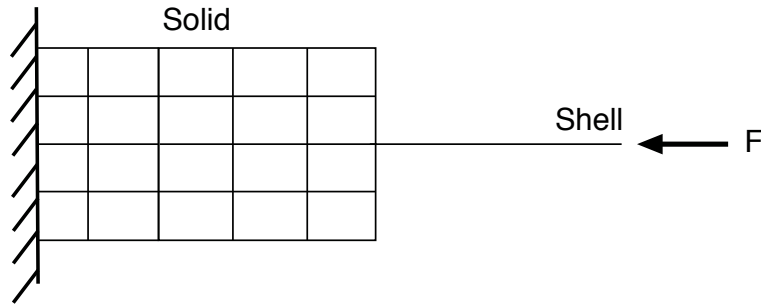

Figure 6.5:   A schematic illustration of the impulse test.

Stepwise transition

The transition can be modelled using three shell elements overlapping the solid elements in the centre of the beam, which schematically is illustrated in Figure 6.6. This in order for the shell elements to get the rotational degrees of freedom required from the solid elements, which do not have these degrees of freedom. In the overlapping section, the stiffness as well as the density, were successively altered in intervals of 25% from the solid elements to the shell elements.
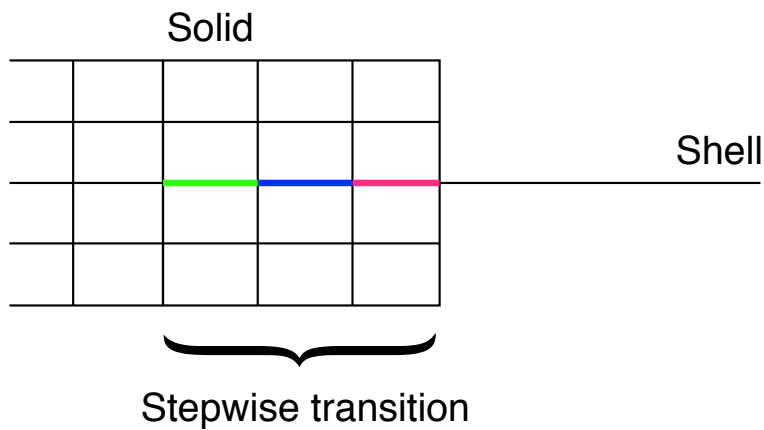

Figure 6.6:   A schematic illustration of the stepwise transition from solid elements to shell elements.

Constrained nodal rigid body

An alternative way to model the transition from solid elements to shell elements is to use CONSTRAINED-NODAL-RIGID-BODY. This constraint is suitable to use when two parts are rigidly joined together, and it is well suited if no failure is of concern within the joined area. This approach constraint the nodes at the transition to act rigidly. The constraint allows the shell elements to get the rotational degrees of freedom

required from the solid elements. A schematic representation of the transition is illustrated in Figure 6.7. The constraint was defined by selecting all the nodes at the solid surface, at the transition, using CONSTRAINED-NODAL-RIGID-BODY in ANSA. The nodes at the solid edge were set to be the master nodes.
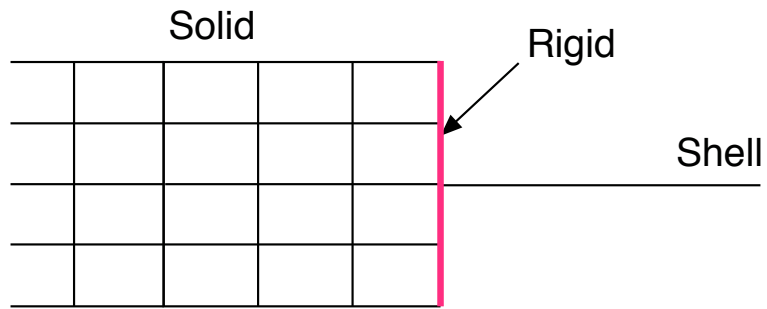

Figure 6.7:   A schematic illustration of a rigid transition from solid to shell elements for constrained nodal rigid body transition.

6.2   Corrugated specimen

It emerged that an additional model would be useful, in order to have an intermediate step between the small cube test and the more extensive three-point bending of the beam. The additional investigated model was crushing of a corrugated specimen, which experimentally has been studied by Costa [24]. This section presents the test setup as well as the building of the corrugated specimen model. For this investigation, LS-DYNA version R8.1.0 with Massively Parallel Processing (MPP) using double precision was used.

The setup of the corrugated specimen was modelled as close to the experimental setup as possible. Same material cards for SICOMP's model and MAT261 were used as for the beam simulations and these cards can be seen in Appendix B and C. No in-situ effects were taken into account nor delamination. In addition, no element deletion was included in the simulations.

As for the beam model earlier studied, it was only necessary to model one fourth of the corrugated specimen since double symmetry planes could be utilised. The boundary conditions along the symmetry planes were defined in accordance to Section 6.1.2. The contact between the corrugated specimen and the ground was modelled using rollers as boundary conditions at the edges which were free to translate horizontally in the plane in Figure 4.5(a). The contact between the impactor and the corrugated specimen was implemented using CONTACT-AUTOMATIC-SURFACE-TO-SURFACE where SOFT=1 with the viscoelastic damping coefficient, VDC, set to 20% in accordance to Section 6.1.2.

The corrugated specimen was discretised using one solid element per ply through the thickness, having the length of 0.1875 mm. Closest to the impactor the length of the elements in each ply were 0.3 mm. Further away the element length was stepwise increased up to the element length of 2 mm. In order to decrease the computational costs, a constant impact velocity of $v = 10$ mm/s was used. This was assumed to be sufficiently slow as long as no dynamical effects occurred, even though an impact velocity of $v = 0.01$ mm/s was used in the experiment. The constant velocity of the impactor was prescribed using the function BOUNDARY-PRESCRIBED-MOTION in ANSA. Furthermore, the objective stress update parameter, OSU, in the CONTROL-ACCURACY keyword was used, in accordance to Section 2.1.3.

7 Results

The following chapter presents the obtained results from the main investigations carried out in this project. The parts covered are; Beam test and Crushing of a corrugated specimen.

7.1 Beam test

All results for the investigations regarding the beam will here be presented. The solid uniform beam as well as the investigation of a transition from solid to shells will be presented. In addition, how the addition of taking delamination into account affects the results, is also included.

7.1.1 Solid uniform beam

In this section, the results for when the beam was modelled using only solid elements throughout the beam will be presented. This model will henceforth be referred to as the solid uniform beam. The solid uniform beam model includes 5.88 million solid elements with the same amount of integration points. This resulted in 18.6 million degrees of freedom. The method used to model the beam is in accordance to the methodology described in Section 6.1.2. The model was used with both material model MAT261 and SICOMP's model and results are presented separately. In addition, a comparison of the results using the two material models will be presented and comparisons to experimental data will be made.

MAT261

An overview of the undeformed beam in the cross section at the symmetry plane parallel to the centerline of the impactor can be seen in Figure 7.1(a). The initial damage occurred underneath the impactor in this symmetry plane. This damage occur at the edge of the largest radius closest to the centre of the beam's cross section as can be seen in Figure 7.1(b). At the fracture location the matrix damage variable reached the value of 1 and thus the matrix reached final failure. How this fracture propagates along the beam is stepwise, at three different displacement states, in Figure 7.2 with a view seen from below. From the results, it can be seen that the fracture occur early in the simulation, and it continues to propagate as the impactor displacement increases.

(a) Undeformed overview.

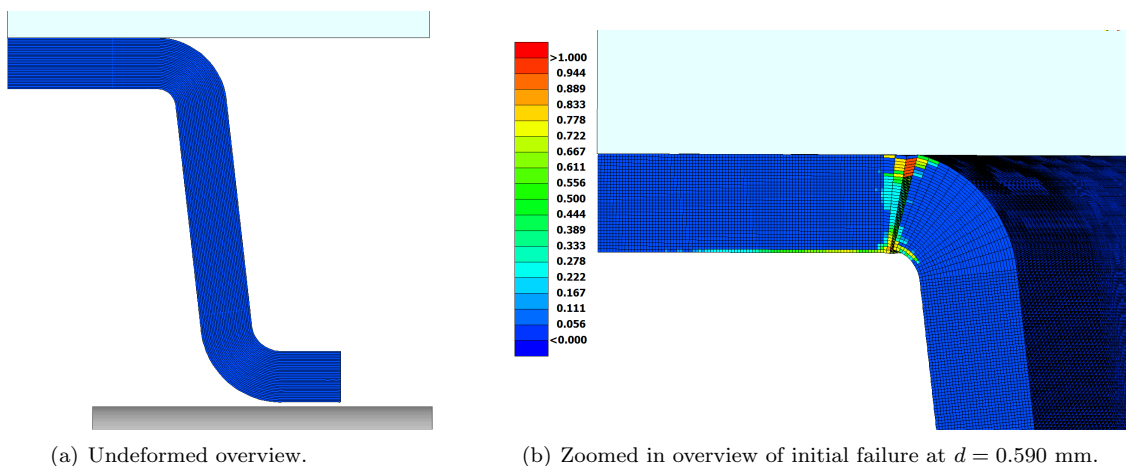(b) Zoomed in overview of initial failure at $d = 0.590$ mm.

Figure 7.1: An overview of the undeformed beam as well as a close up view of where failure initiates where the matrix damage variable is visualised, along the radius of the beam.

(a) $d = 0.590$ mm
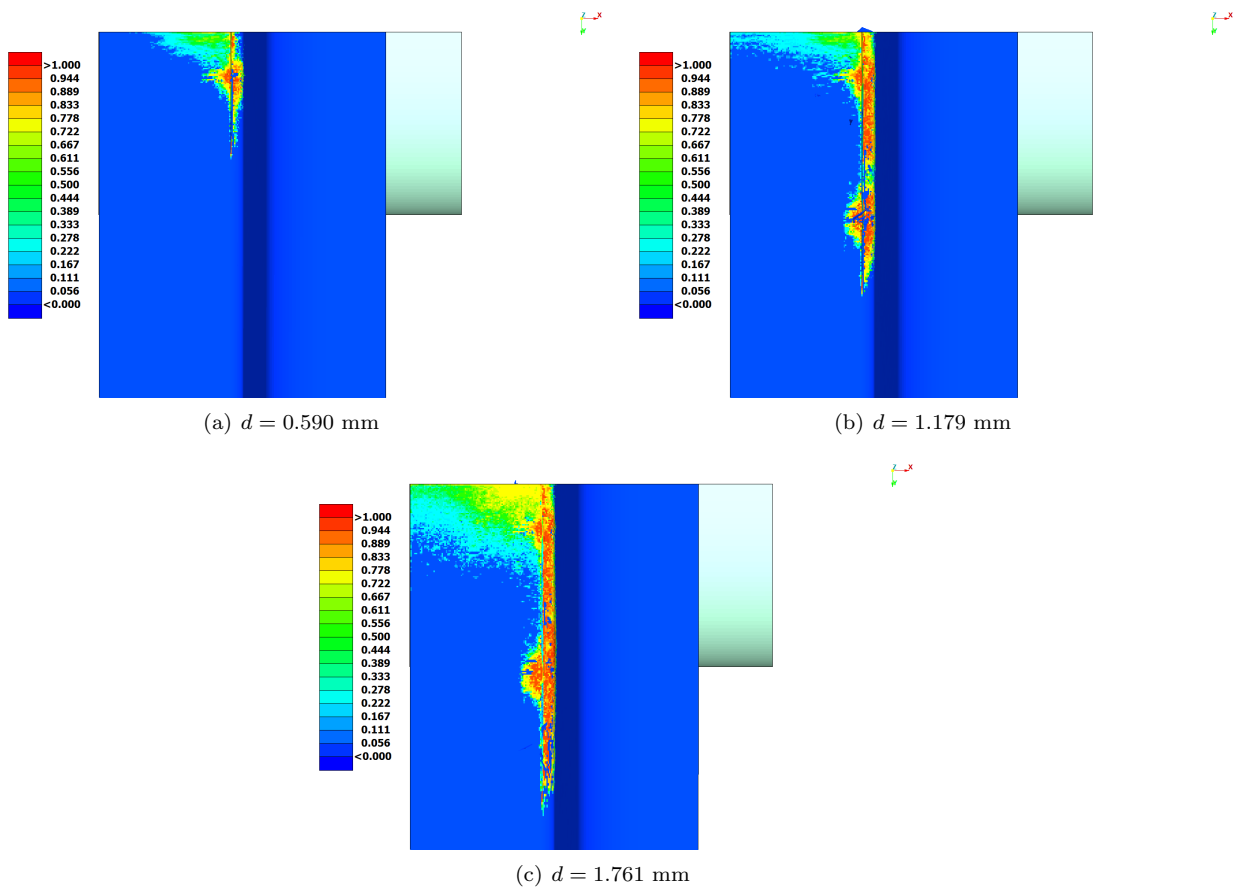

(b) $d = 1.179$ mm

(c) $d = 1.761$ mm

Figure 7.2: Illustration of the matrix damage variable for how the failure, along the radius of the beam, propagates throughout the simulation for three different impactor displacements, d. The view is seen from below, with the impactor coloured as silver.

Figure 7.3 illustrates the fibre driven damage for both fibre tension and fibre compression at the impactor displacement $d = 1.761$ mm. It can be seen that some elements are damaged in both tension and compression, which is unphysical. This since only one of these modes can be present in one element at the time. When the beam model using only solid elements was run using MAT261 the simulation were pre-terminating when the displacement of the impactor was $d = 1.96$ mm. The termination was due to that an element with negative volume occurred. From the results it can be observed that both fibre failure modes are present where fibre compression is slightly more pronounced at the damage observed underneath the impactor.

(a) Fibre tension
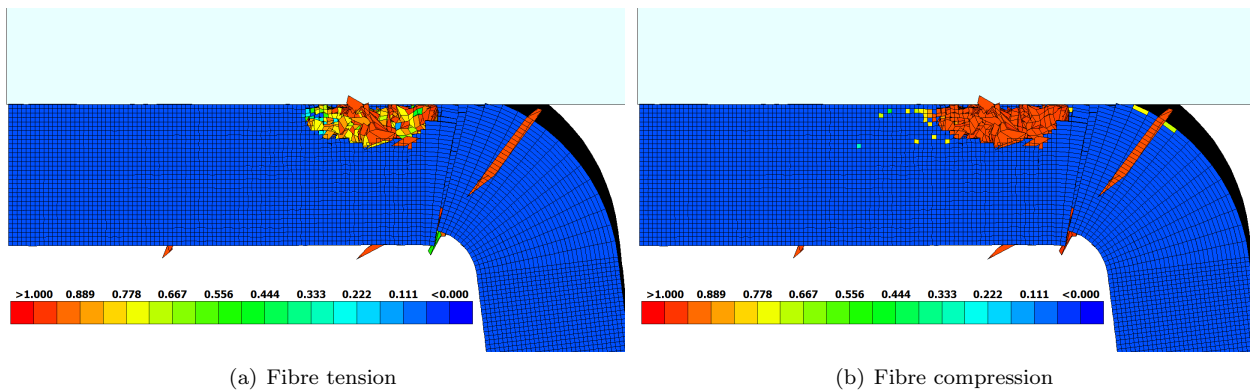

(b) Fibre compression

Figure 7.3: Illustration of the fibre dominated damage variables underneath the impactor, including fibre tension damage variable as well as fibre compression damage variable, at the impactor displacement $d = 1.761$ mm.

The energy-displacement response, Figure 7.4, illustrates that the internal energy becomes negative when the displacement reached 0.724 mm. A negative internal energy indicates that there are unphysical behaviours within the model. Whether this unphysical behaviour is attributed to elements which are released from the beam without being fully damaged, and hence not deleted, or elements that still contributes to the strength of the beam is hard to conclude. The results from this simulation generates negative internal energy, which implies that the results are unreliable. At the same displacement where the internal energy drops below zero, it can also be seen that the artificial energy starts to increase. This implies that the results becomes unreliable as the impactor displacement reaches 0.724 mm.
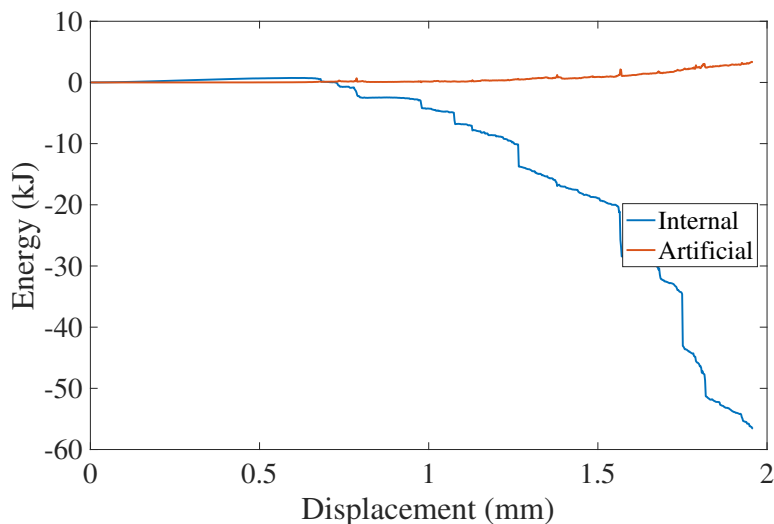

Figure 7.4: Illustration of the obtained energy-displacement responses for the beam using MAT261.

36

MAT261 with ERODE

As was observed in the previous section the simulation was pre-terminated due to negative volume. If negative volumes or other strangely elements occur some different erosion editions can be added in order to remove these unwanted elements. It was observed that before the negative volume occurred in the simulation, the time step was decreased significantly. Thus, one approach to remove elements with negative volume is to set the ERODE flag in CONTROL-TIMESTEP to 1 whilst the minimum time step, TSMIN, is required to be a non zero value. This causes the elements which gives smaller time step than the set value of TSMIN to be eroded [26]. The time step when strangely shaped elements occurred was defined as the minimum time step. This gave that TSMIN$= 2 \cdot 10^{-9}$ s.

It is of importance to be aware of that adding this flag may allow the simulation to reach further. However ERODE do not take into account if the element still contributes to the structure or if it has been detached from it. Thus, this method may affect the result by deleting elements which still may contribute. This entails that this method should not be used if not necessary and if it is used it should be used with caution.

Having this ERODE flag active, the simulation managed to reach further. However, the simulation was cancelled at an impactor displacement of $d = 2.91$ mm, due to that the time step became to small in order for the simulation to proceed. Although the minimum time step to be allowed was set to TSMIN$= 2 \cdot 10^{-9}$ s the time step decreased below this value without eroding the elements causing this small time step. The same failure of the beam was obtained with the ERODE flag set to active, as without it. Thus, the results presented in this subsection will only include energy-displacement responses. The obtained energy-displacement response is being illustrated in Figure 7.5, where it can be observed that the internal energy as well as the artificial energy follows the same trend as without the ERODE flag activated.
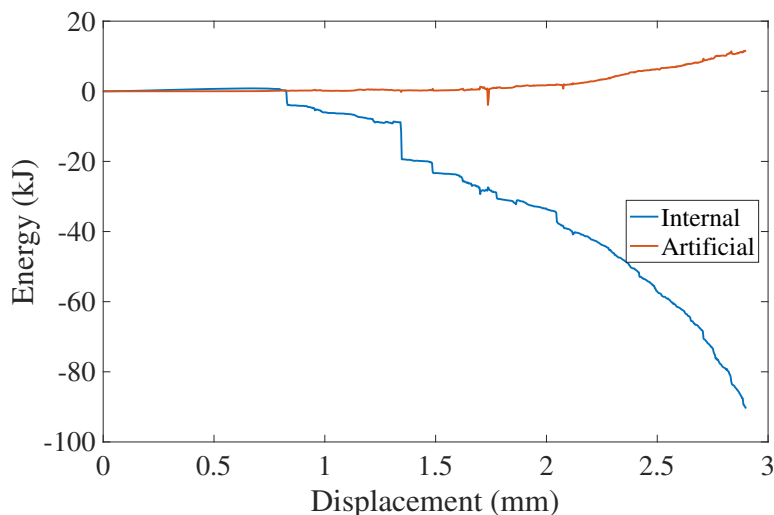

Figure 7.5: The obtained energy-displacement responses for the beam using MAT261 and ERODE.

SICOMP's model

The beam model using only solid elements was run using SICOMP's material model. In the simulation, no element deletion were allowed since this feature was initially not implemented in the usermat subroutine. The simulation ran to the impactor displacement of $d = 22$ mm which was approximately the same end displacement as the experimental results. Figure 7.6 illustrates the damage variables at the symmetry plane below the impactor for the time step corresponding to $d = 22$ mm. It can be observed that damage occurred through the thickness of the beam as also was seen using MAT261. In matrix tension, Figure 7.6(b), it can be seen that the lowermost 90 degree ply experience damage. However, no fibre tension damage can be observed, seen in Figure 7.6(c).

Finally, the damage arising in fibre compression, Figure 7.6(d), indicates that damage occur at the uppermost 0 degree plies underneath the impactor. Furthermore, damage occurred at the lowermost ply in the vertical part of the beam.

(a) Matrix compression

(b) Matrix tension

(c) Fibre tension

(d) Fibre compression
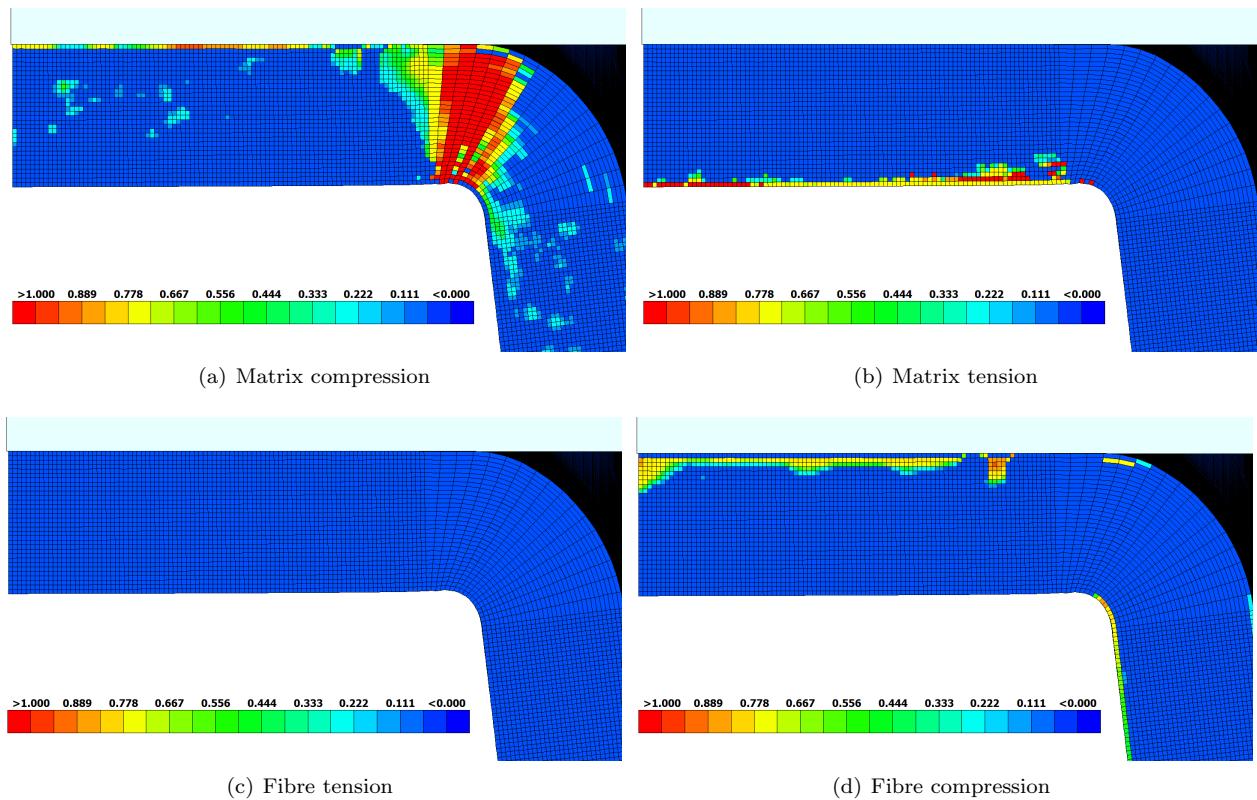
Figure 7.6: Illustration of the damage variables, using SICOMP's model, in the cross section below the impactor at the displacement $d = 22$ mm.

In Figure 7.7(a), the beam is shown from below for matrix compression. It can be seen that the damage which initiates from the symmetry plane at the impactor continued to grow along the radius. However the growth only extends a short distance. The extension of the matrix tension damaged area in Figure 7.6(b), is shown in Figure 7.7(b) with a view seen from below.
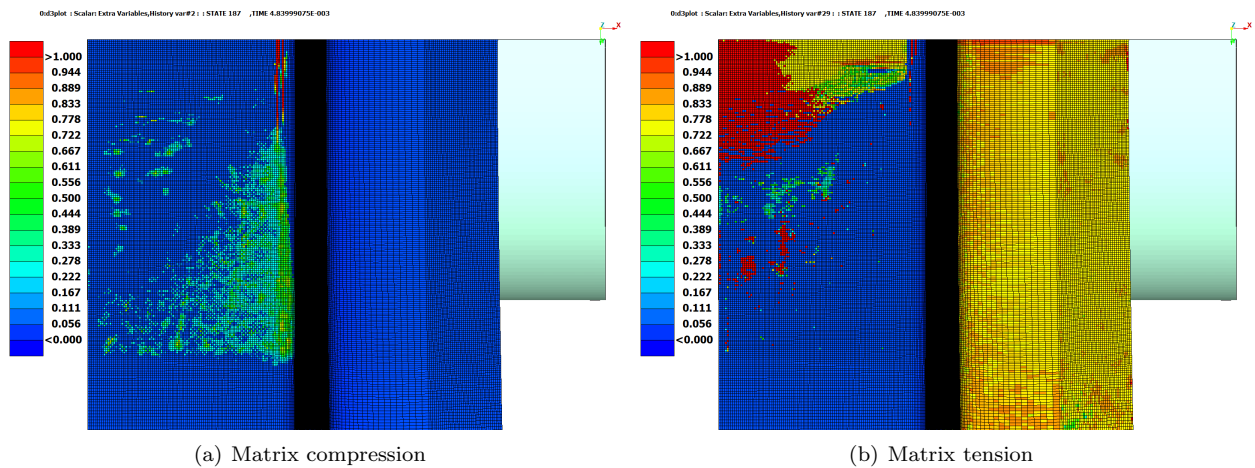
(a) Matrix compression

(b) Matrix tension

Figure 7.7: Illustration of the matrix damage variables for how the failure, along the radius of the beam, at the displacement $d = 22$ mm. The view is seen from below, with the impactor coloured as silver.

The obtained energy-displacement response is illustrated in Figure 7.8. From the results, it can be observed that the artificial energy starts to increase as the impactor displacement reaches $d = 5.92$ mm, where the ratio between the artificial energy and the internal energy is 5%. This implies that the results becomes unreliable for impactor displacements larger than $d = 5.92$ mm [15].
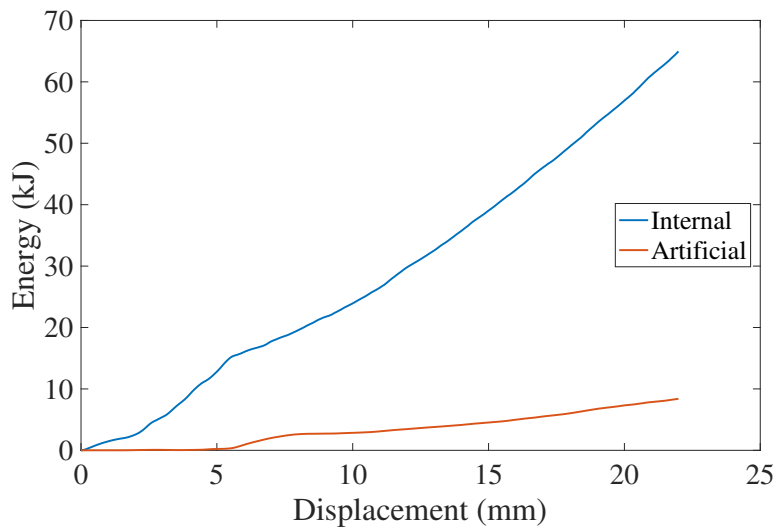

Figure 7.8: Illustration of the obtained energy-displacement responses using SICOMP's material model.

Comparison

In this section, a comparison between MAT261 and SICOMP's material model will be presented. The comparison will include the damage modes as well as the relation between force and displacement. In addition a comparison of the energy absorbed in the crash will be presented. The results in the simulations will also be compared to the experimental test.

The damage arising in the simulation using MAT261 and SICOMP's model was similar. The same damage at the large radius of the beam was seen for both models, Figure 7.1(b) and Figure 7.6(a) correspondingly. However, for SICOMP's model this matrix damage occurred for a larger displacement of the impactor compared to MAT261. Furthermore, this matrix damage grew shorter along the beam using SICOMP's model, Figure 7.7(a), compared to MAT261, Figure 7.2. Since the damage formulation is different between the material models in this mode of failure, this can be one cause for the difference in damage growth.

The damage at the upper part of the beam cross section using MAT261, Figure 7.3, which initiated due to fibre damage was not arising using SICOMP's model. When using SICOMP's material model, only the first initiated failure mode is allowed in the damage evolution. This implies that it is only the first occurring failure mode which is taken into account. This can be the reason to why the damage, seen in fibre damage for MAT261, is not seen when using SICOMP's model.

Figure 7.9(a) illustrates a comparison between the force-displacement response from the experimental test and the finite element simulations, using both MAT261 and SICOMP's material model. In this comparison, the force-displacement responses have been shifted in displacement in order for the first significantly force increase to occur in the support at the same displacement. This implies that small initial force responses before the actual increase of the force are excluded. The obtained results from the finite element simulations, with SICOMP's material model, indicates that the force response is significantly lower compared to the experimental test. The maximum force peak in the experiment was observed to be $F = 32$ kN, whilst it with SICOMP's material model measured a peak force of $F = 12.5$ kN, i.e. 61% lower. The force peak in the experimental test occurred at an impactor displacement of $d = 10$ mm, whereas with SICOMP's material model it occurred at $d = 4.9$ mm. The simulations using MAT261 did not reach as far as with SICOMP's material model, but it can be seen in Figure 7.9(b), that also this material model overestimates the initial force peak. The maximum force peak obtained was $F = 8.4$ kN, at an impactor displacement of $d = 1.2$ mm. However, it is hard to draw any conclusions if the two material models correlates to each other without having more results with MAT261.

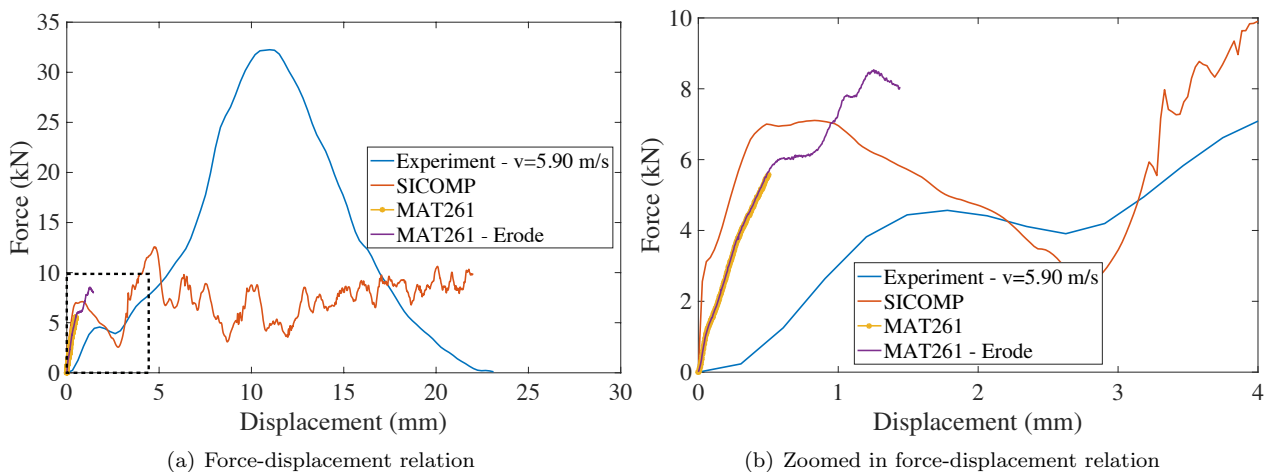(a) Force-displacement relation (b) Zoomed in force-displacement relation

Figure 7.9: Force-displacement response for the experimental test and finite element simulations using MAT261 and SICOMP's material model.

In the subsequent figure, Figure 7.10, a comparison of the energy-displacement response of the absorbed energy for the finite element simulations, as well as the experimental test is illustrated. As for the force-displacement response, the zero displacement have been adjusted in order for the energies to start to increase at the same displacement. From the results it can be seen that the absorbed energy is much larger in the experimental test, compared to the simulation results. In the experimental test the absorbed energy follows a s-shaped curve and it has a maximum of $E = 300$ kJ. The absorbed energy from the simulation results with SICOMP's model increases linearly up to a maximum value of $E = 80$ kJ. The two material models under consideration follows a similar energy-displacement response until the simulation with MAT261 pre-terminates.
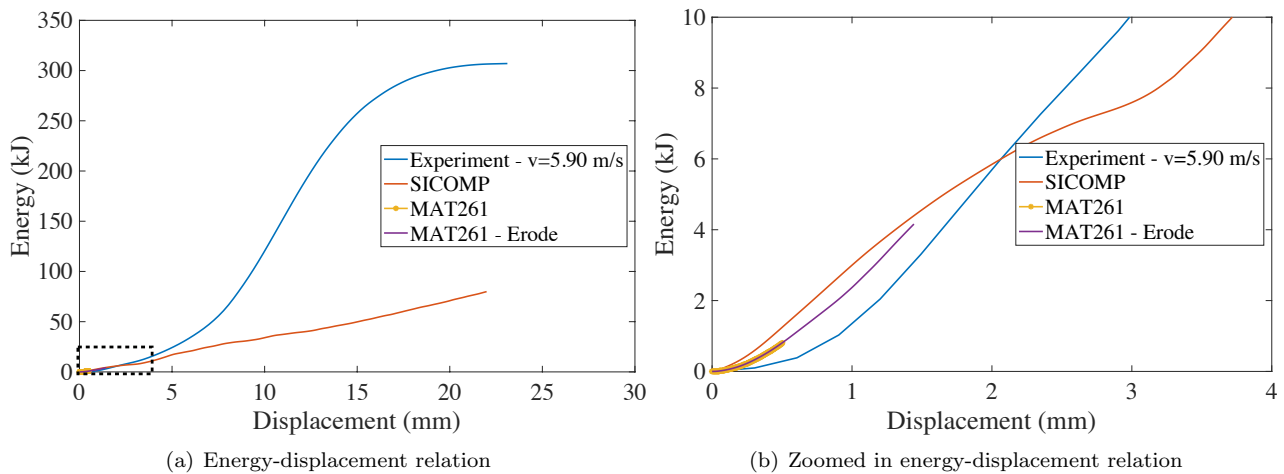

(a) Energy-displacement relation   (b) Zoomed in energy-displacement relation

Figure 7.10:   Energy-displacement response for the experimental test and finite element simulations using MAT261 and SICOMP's material model.

7.1.2 Transition solid to shell

Stepwise transition

The relation between force and displacement in a three-point bending with and without the transition from solid to shell was simulated and the corresponding results are illustrated in Figure 7.11. As can be seen, the response have overall same tendency for both models. A slight offset can be seen between them which increases for increasing displacement.
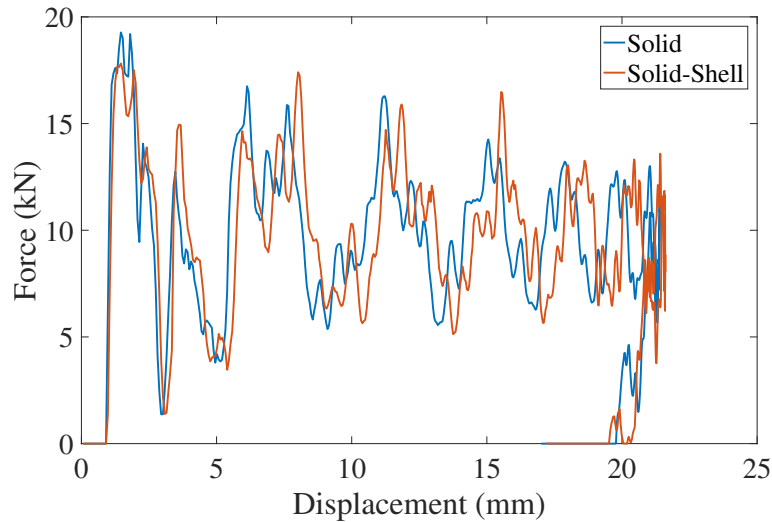

Figure 7.11: The force versus the displacement with and without the solid to shell transition using stepwise transition.

Figure 7.12 illustrates the propagation of the displacement field in the y-direction at four different time steps; where Figure 7.12(a) represents the initial state at t=1ms, Figure 7.12(b) the second state at t=1.032 ms, Figure 7.12(c) the third state at t=1.045 ms and finally Figure 7.12(d) the fourth state at t=1.075 ms.

(a) t=1 ms

(b) t=1.032 ms

(c) t=1.045 ms

(d) t=1.075 ms
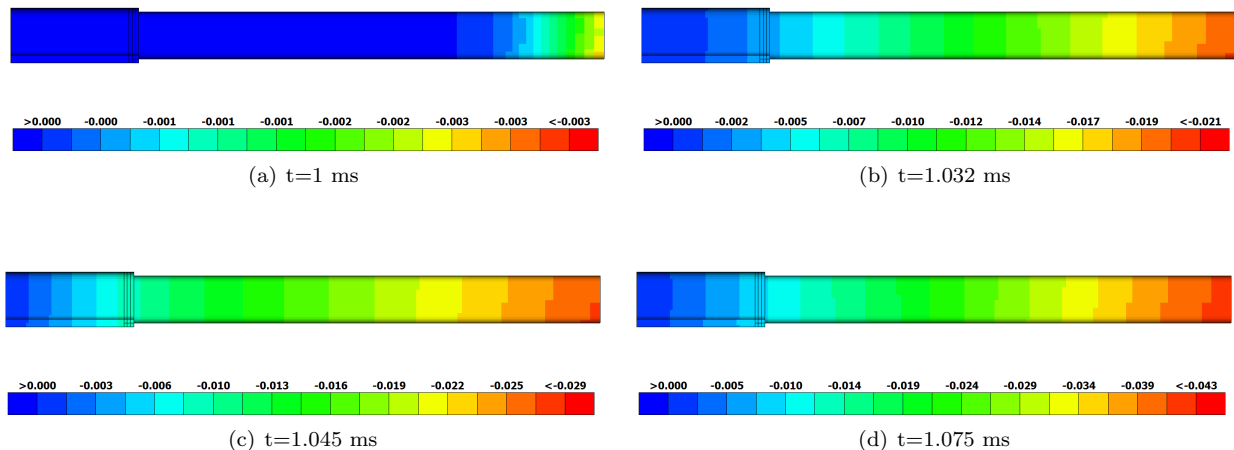
Figure 7.12: The propagation of the displacement field in y-direction caused by an impulse load for stepwise transition.

The displacement field was also studied along a nodal path with five nodes. Two nodes were located in the shell section just before the transition, and one node was located at the transition. Additionally two nodes were located just after the transition in the solid section, as can be seen in Figure 7.13(a). From the obtained results, presented in Figure 7.13(b), it can be observed that the nodal displacements along the nodal path

corresponds well to each other. It can be seen that the absolute value in a peak or valley is decreasing closer to the fixed wall. In addition, the fixed support will prevent the displacement of the nodes closer to it. This implies that higher stresses should occur closer to the wall, which also was observed. As a concluding remark, the results indicates that the impulse wave propagates through the shell section of the beam, into the solid section of the beam, without any reflection.

(a) Nodal path
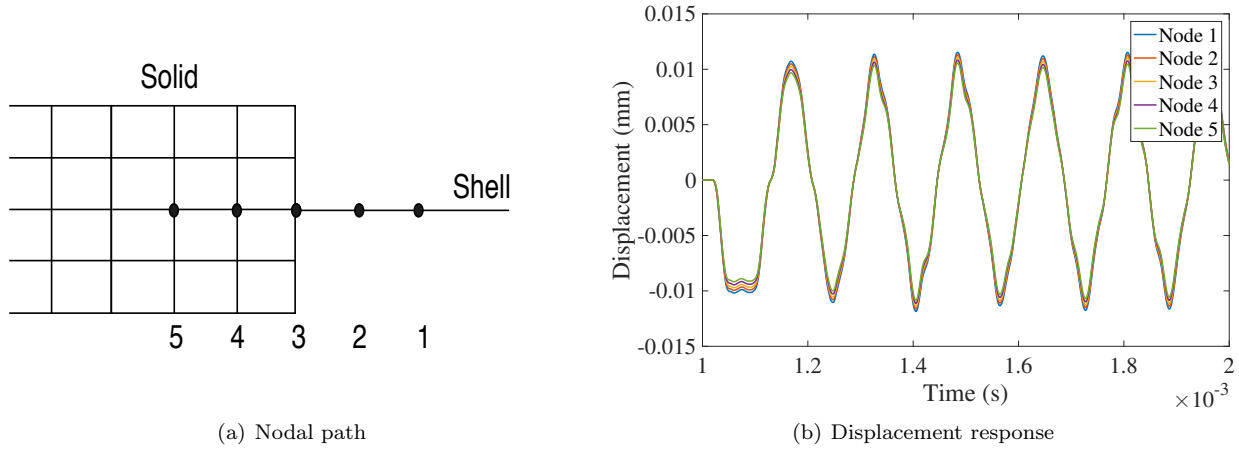

(b) Displacement response

Figure 7.13: The y-displacement in five nodes, before as well as in and after the solid shell transition, throughout the simulation for stepwise transition.

The results for the global energies (kinetic, internal and total energy) throughout the simulation time can be seen in Figure 7.14. By studying the obtained results it can be seen that the sum of the kinetic and internal energy gives the total energy. In addition it can be observed that the total energy increase as the impulse load hits the shell edge of the beam. The energy increase then stagnates at $t = 1.1$ ms, since the impulse load is released at this time, and the kinetic energy goes down to zero. The total energy is then remained constant throughout the simulation.

Figure 7.14: The kinetic, internal and total energy of the system throughout the simulation for stepwise transition.

From the results, it can be concluded that the transition from solid to shell works well. The stresses and displacements are not mirrored at the transition and no energy losses can be seen. However, if extending this transition technique to the final model using MAT261, see Figure 7.15(a), it was observed that the transition caused problems. The solid elements closest to the transition region failed, which can be seen in Figure 7.15(c). The reason to why this problem occur may be explained due the low strength in shear as well as matrix tension for this material. By this reason, another transition technique was investigated.
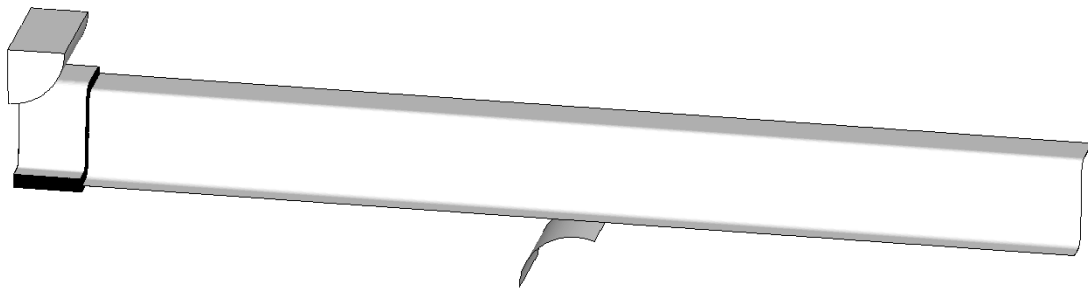
(a) Overview of beam
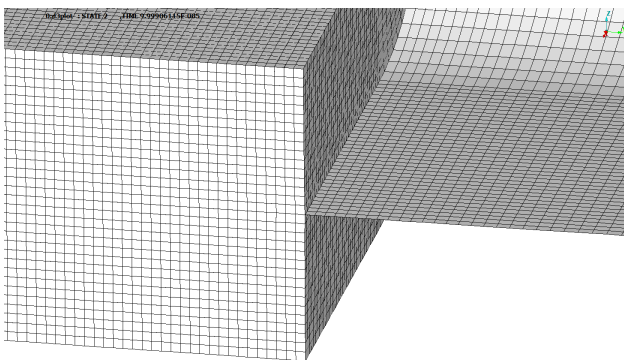
(b) Zoomed in before failure
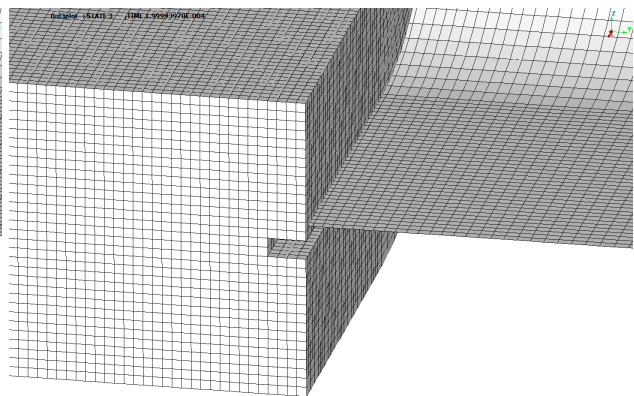
(c) Zoomed in after failure

Figure 7.15: Beam modelled with a stepwise transition from solid elements to shell elements, illustrating the elements around the transition region before and after failure.

Constrained nodal rigid body

The force-displacement response for the three-point bending analysis for this transition method can be seen in Figure 7.11. The response is similar as without any transition.
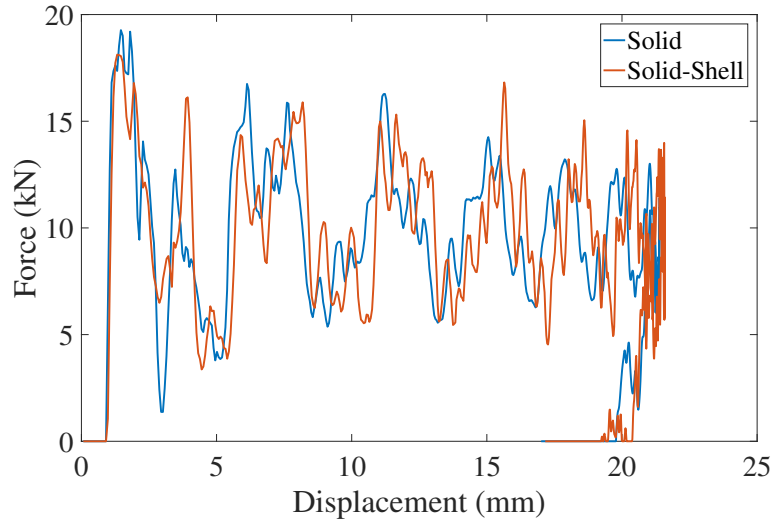
Figure 7.16: The force versus the displacement with and without the solid to shell transition using constrained nodal rigid body transition.

The impulse analysis gave results equivalent to the stepwise model for energies, Figure 7.17, and for the y-displacement throughout the beam as well as at the transition, as can be seen in Figure 7.18 and 7.19.
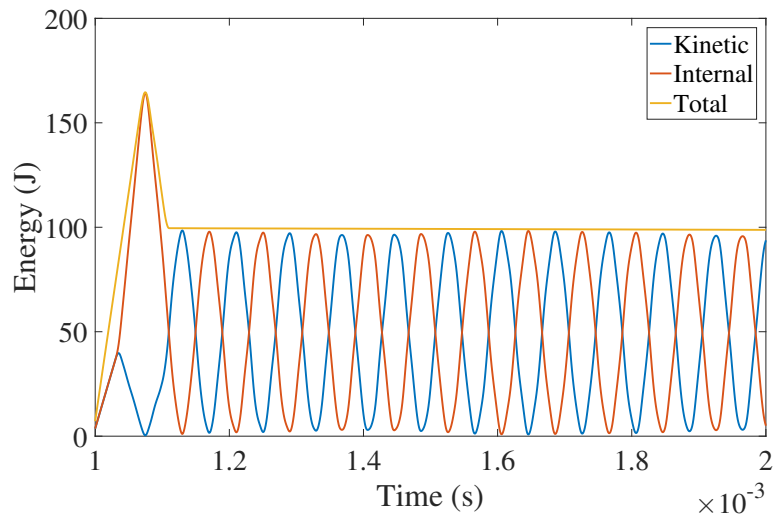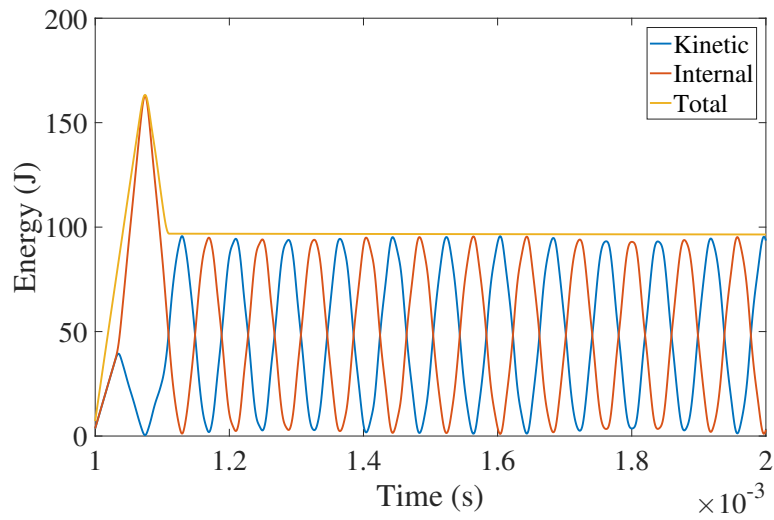

Figure 7.17: The kinetic, internal and total energy of the system throughout the simulation for constrained nodal rigid body transition.

(a) t=1 ms

(b) t=1.032 ms

(c) t=1.045 ms

(d) t=1.075 ms
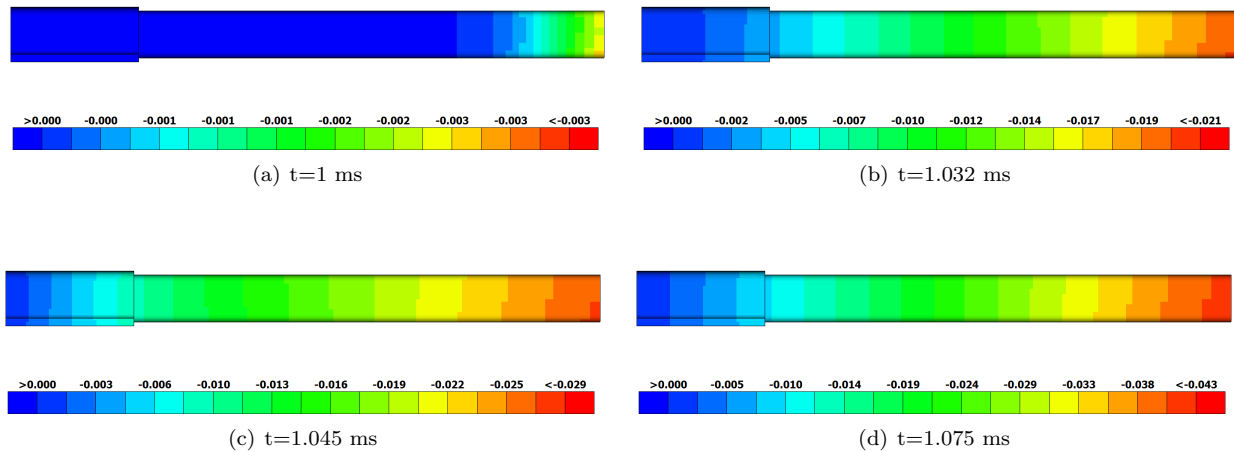
Figure 7.18: The propagation of the displacement field in y-direction caused by an impulse load for constrained nodal rigid body transition.

(a) Nodal path

(b) Displacement response
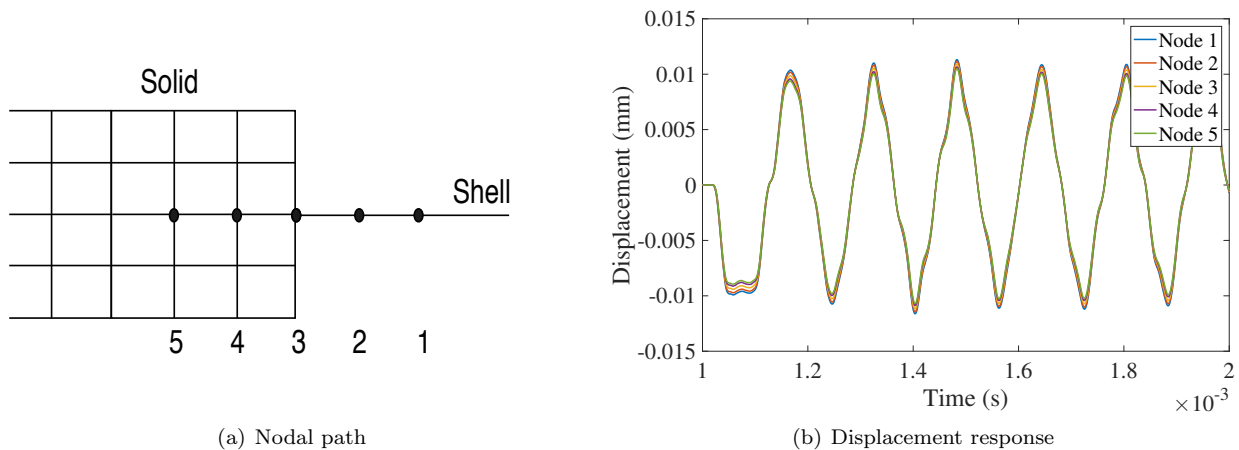
Figure 7.19: The y-displacement in five nodes, before as well as in and after the solid shell transition, throughout the simulation for constrained nodal rigid body transition.

The results shows that the transition works well for this simplified analysis. When applying the transition to the final model, using MAT261, it was seen that the transition works well also here. This implies that this method to model the transition should be applicable is this application.

Solid uniform beam vs transition solid to shell

A comparison of the resulting damage in the beam for the constrained nodal rigid body transition and the solid uniform beam will here be presented using the material model MAT261. The solid uniform beam was modelled according to Section 6.1.2 and the transition from solid to shell was modelled using a constraint nodal rigid body. The distance discretised with solid elements was 30 mm from the impactor, corresponding to the fracture zone.

Independently which model used, the initial damage occurred at the edge of the largest radius closest to the centre of the beam's cross section. The fracture for constrained nodal rigid body transition as well as for using the solid uniform beam model can be seen in Figure 7.20. As can be seen the same initial failure can be seen at the radius for both models. However, for the solid uniform beam a more widespread failure occur in the cross section. Furthermore an additional failure occurred at the top of the beam underneath the impactor which did not occur using the transition.

In Figure 7.20, the propagation of the fracture at the radius is also being illustrated for both models. It can be seen that the fracture, when using the transition model, is prevented to propagate in the same extent as for the solid uniform beam. In addition the computational time where compared between the modelling methods. The cpu time to reach to the simulation time 0.2 ms was calculated for both models. The results from this showed that the transition from solid to shell was 74% faster.

(a) Solid uniform beam   (b) Constrained nodal rigid body transition
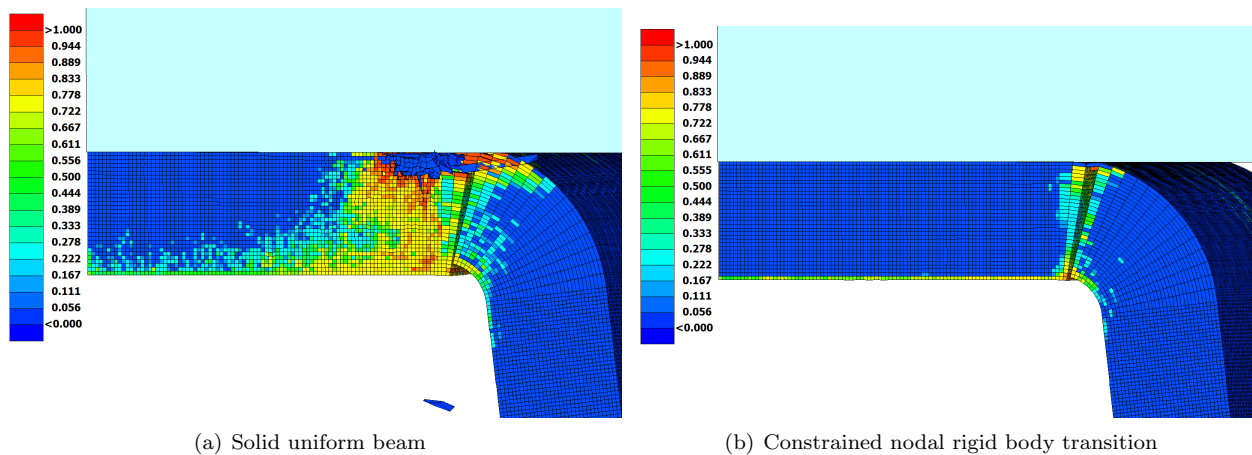
Figure 7.20: The damage of the beam at the impactor displacement of 1.470 mm.

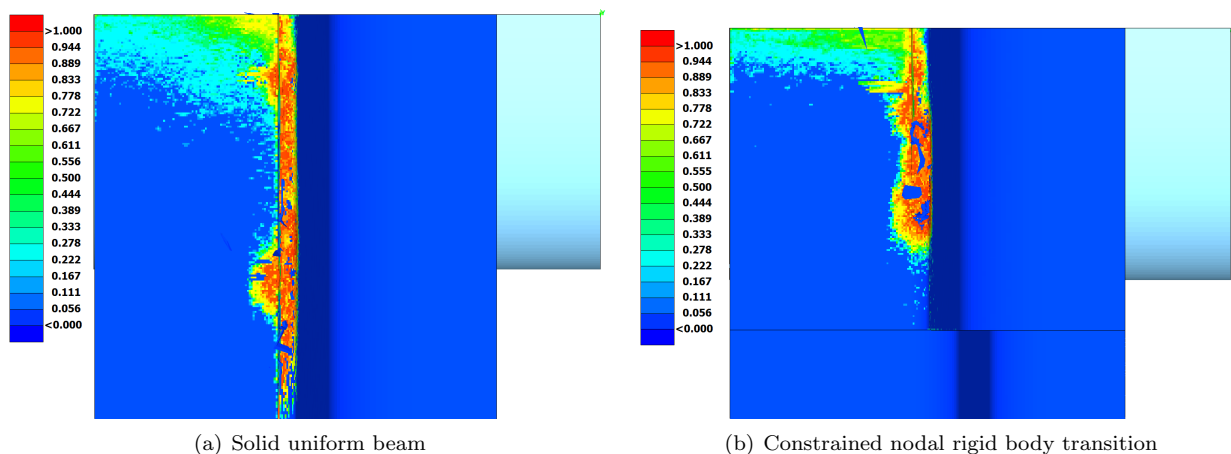(a) Solid uniform beam   (b) Constrained nodal rigid body transition

Figure 7.21: The damage underneath the beam at the impactor displacement of 1.470 mm.

It was observed that although the transition using a stepwise transition worked, with an isotropic material model, the method did not work for the composite material under consideration. The stepwise transition

only transferred the stresses through the interface between the two middle plies, which resulted in failure in the elements closest to the transition in these two plies. For the constrained nodal rigid body transition, the contact did not experience failure. However, the growth of the damage were altered compared to when only solid elements were used. This might be due to that the constrained nodal rigid body constraint gave a to stiff behaviour of the beam or that the transition were to close to the zone where fracture occurred. The distance from the impact to the transition were determined to be outside the fracture zone seen in experiments. However, for some reason this might not have been sufficiently far away.

The results indicate that using the constrained nodal rigid body transition influenced the failure behaviour of the beam. The fracture at the radius of the beam was prevented to grow along the beam in the same extent and the fracture just underneath the impactor were not arising. Thus, even if the transition significantly decreased the cpu time this transition method is not appropriate to use in order to get reliable results.

7.1.3 Delamination

MAT261

The simulation using MAT261 was cancelled at the impactor displacement of $d = 1.592$mm due to that the time step became too small in order for the simulation to proceed. The first damage was seen to be triggered by matrix dominated damage as is illustrated in Figure 7.22(a). It was noticed that the damage now occurred along the second ply from below at the radius. This damage continues to grow as the displacement of the impactor increases as is illustrated in Figure 7.22(b).

Furthermore, a zone in the top of the beam was seen where fibre dominated damage occurred. This damage is illustrated using failure variable for fibre compression and tension in Figure 7.23 for two different impactor displacements. As can be seen the damage occurred mainly due to fibre compression. When elements are released from the beam, some elements also experiences damage in fibre tension.

It was seen that delamination occurred at the edge of the radius in the connection between both the uppermost and lowermost cohesive layer. The delamination was growing along, as well as towards, the middle of the beam as the simulations continued.

(a) $d = 0.590$mm

(b) $d = 1.592$mm

Figure 7.22: Illustration of how the matrix dominated damage propagates throughout the simulation for two different impactor displacements.

The internal as well as the artificial energy is illustrated in Figure 7.24. The internal energy became negative, as for the solid uniform beam, at a displacement of $d = 1$ mm and continued to decrease as the simulation continued. At the same displacement, the artificial energy was increasing significantly. This implies that the results after this displacement are unreliable.

(a) Fibre compression $d = 1.179$ mm

(b) Fibre compression $d = 1.761$ mm

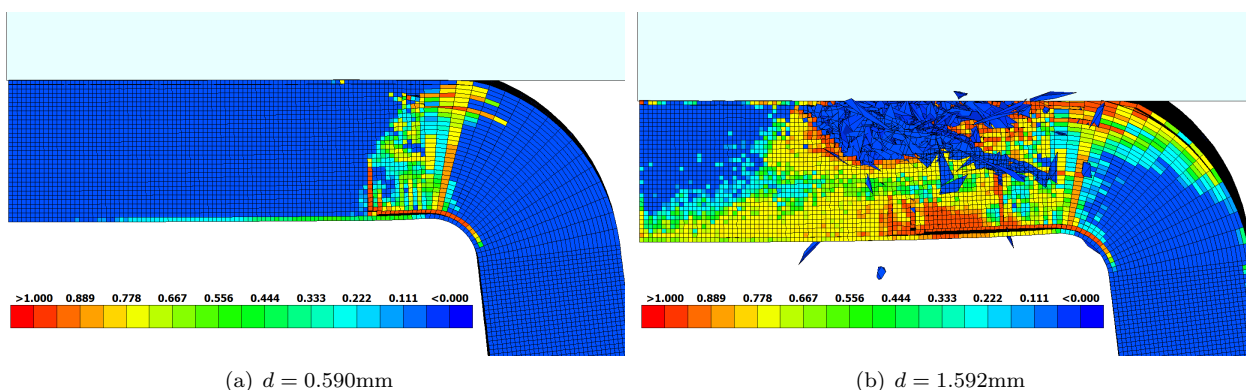

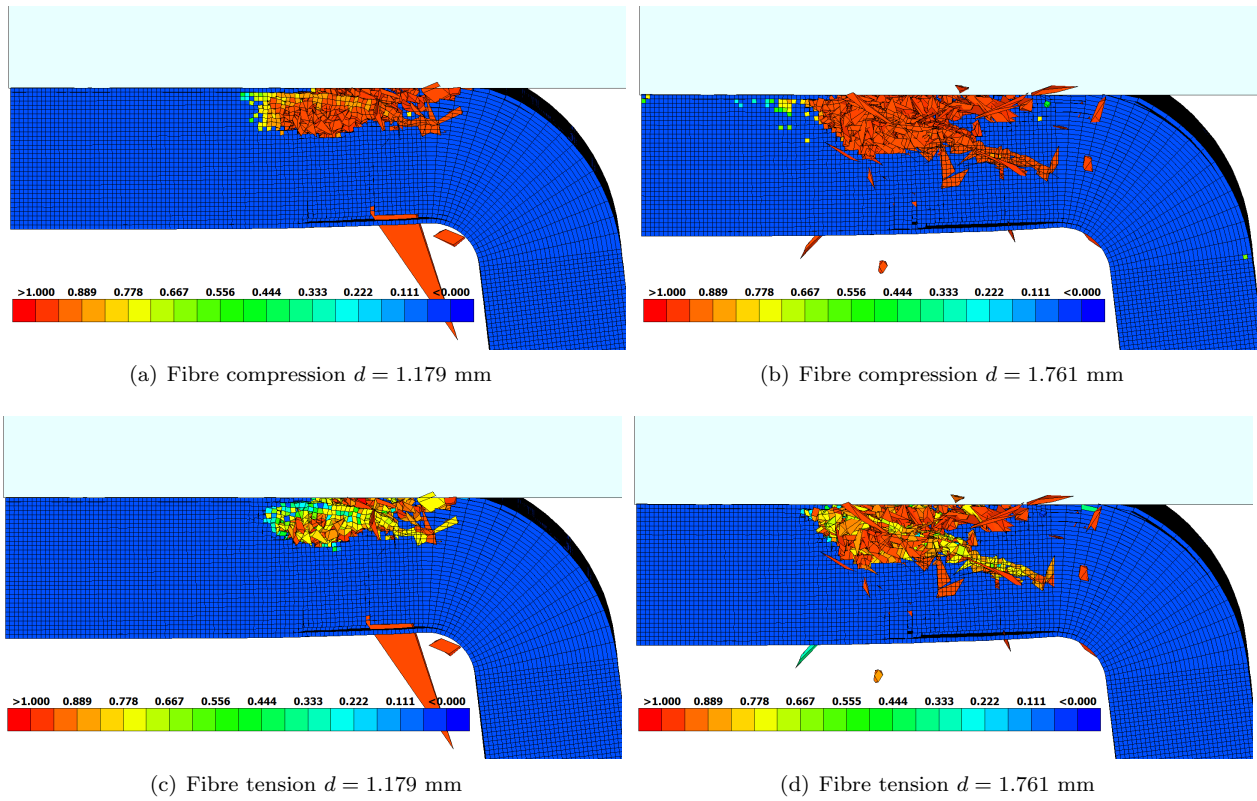(c) Fibre tension $d = 1.179$ mm

(d) Fibre tension $d = 1.761$ mm

Figure 7.23: Illustration of how the fibre dominated damage propagates throughout the simulation for two different impactor displacements, d.
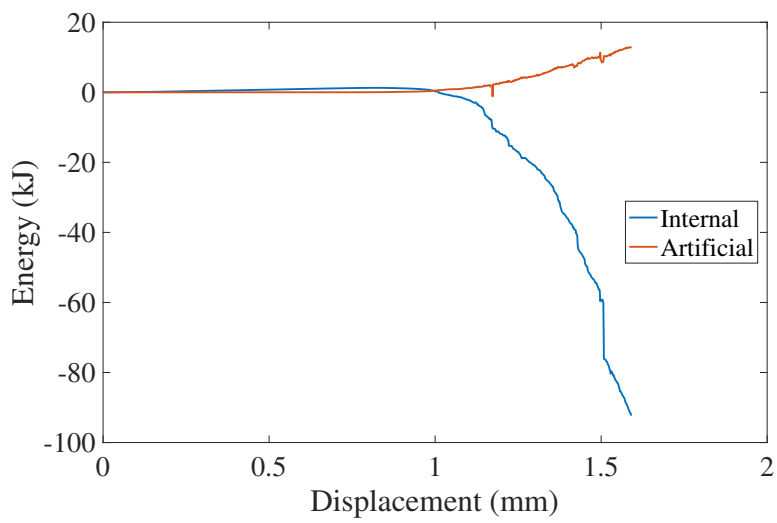
Figure 7.24: Energy-displacement response of the internal energy as well as the artificial energy.

SICOMP's model

Initially, the simulation cancelled at an impact displacement of $d = 6.49$ mm due to that the calculated maximum strain in the failure onset routine exceeded the onset strain. This implies that during one time step the stress calculated, using an elastic relation to the strain, was higher than the strength of the material in accordance to Section 2.2.3. The failure onset variable in matrix tension was $f_{mt} = 8.9$. Thus, the strength of the material was exceeded by the calculated stress, by a factor of 8.9. In order to reach further with the simulation, a smaller scale factor of the calculated time step was used. This was done by changing the default value of SCFT=0.9 to SCFT=0.6. With this modification, the simulation successfully terminated at an impact displacement of $d = 12.95$ mm.

The first damage to occur was, as before, the damage through the beam thickness at the radius which is illustrated in Figure 7.25(a). It can be seen that the damage occur in matrix compression. In addition, a clear delamination occur between the lowermost 90 degree ply and the overlaying 0 degree ply. Figure 7.25(b) illustrates the damage variable for matrix tension where it can be seen that damage in this mode occur at the lowermost 90 degree ply. No damage occurred in fibre tension which is illustrated in Figure 7.25(c). In fibre compression, damage occur in the uppermost part of the beam, close to the impactor as can be seen in Figure 7.25(d). However, fully damage did not occur in this mode. As the simulation continued the delamination grew as illustrated in Figure 7.26 where it can be seen that a more extended damage in matrix tension occurred, compared to when no delamination was permitted, Figure 7.7.

(a) Matrix compression

(b) Matrix tension

(c) Fibre tension

(d) Fibre compression
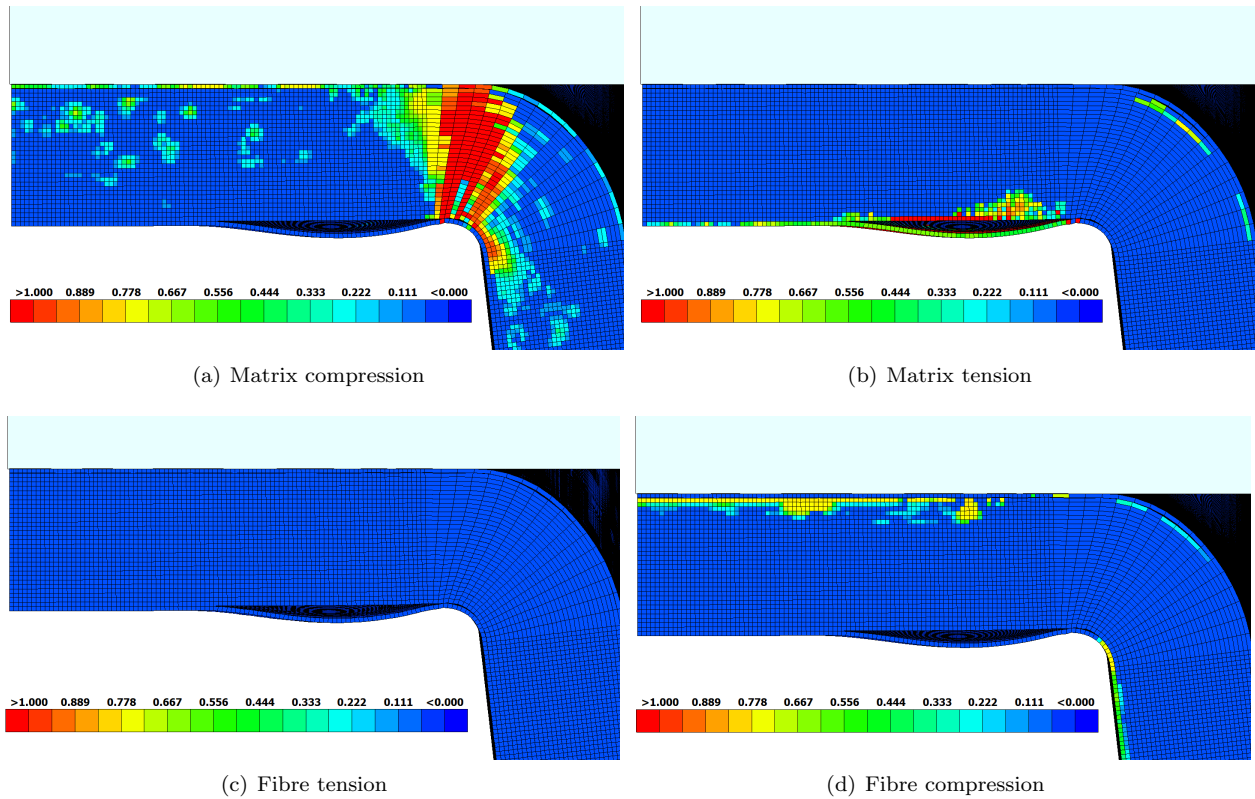
Figure 7.25: Illustration of the damage variables, using SICOMP's model, including delamination in the cross section at the impactor at the displacement $d = 5.653$mm.
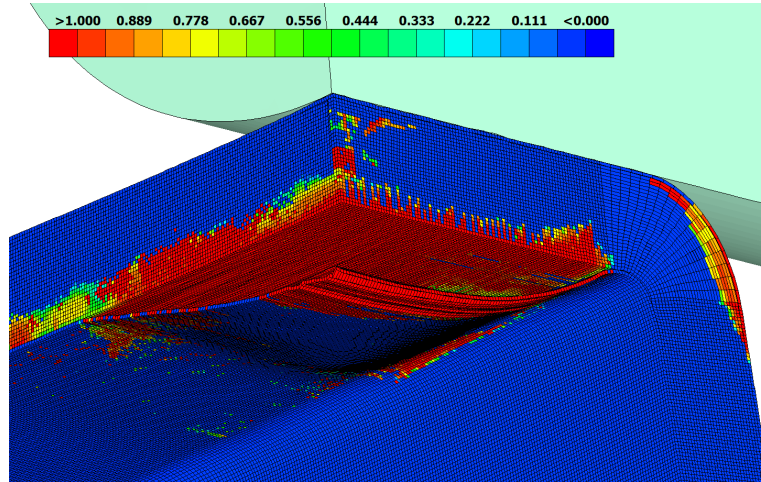
Figure 7.26:   Illustration of the damage variable for matrix tension, using SICOMP's model, including delamination at the displacement $d = 12.95$mm.

The internal as well as the artificial energy with respect to the impactor displacement is illustrated in Figure 7.27. It can be observed that the internal energy is almost linearly increasing throughout the simulation. However it was also observed that the artificial energy starts to increase as the impactor displacement reaches $d = 4$ mm. The ratio between the artificial energy and the internal energy reaches 5% for the displacement of $d = 5.83$ mm. This implies that the results becomes unreliable for displacements larger than $d = 5.83$ mm.

Figure 7.27:   Illustration of the obtained energy-displacement responses including delamination using SICOMP's material model.

Comparison

In this section a comparison between the results with and without delamination using MAT261 and SICOMP's material model will be presented. The comparison will include the damage modes as well as the relation between force and displacement. In addition, a comparison of the energy absorbed in the crash will be presented. The results in the simulations will also be compared to the experimental test.

It was seen that when adding delamination between the 0 and 90 degree plies the initial failure was altered using MAT261. The fracture at the radius through the beam thickness which was seen for the solid uniform beam, Figure 7.1(b), did not occur when adding delamination. Instead, matrix damage at the lowermost 0 degree ply at the radius occurred, Figure 7.22(a).

The damage occurring in the simulation using SICOMP's model was similar between the results with and without delamination. The same damage occurred at the large radius for both models which can be seen in Figure 7.6(a) and Figure 7.25(a). Furthermore the same damage trends can be seen for the other damage variables without delamination, Figure 7.6, as well as with delamination, Figure 7.25. The main difference is that the lowermost 90 degree ply delaminates, which results in that more damage occurred in matrix tension, in the lowermost 0 degree plies.

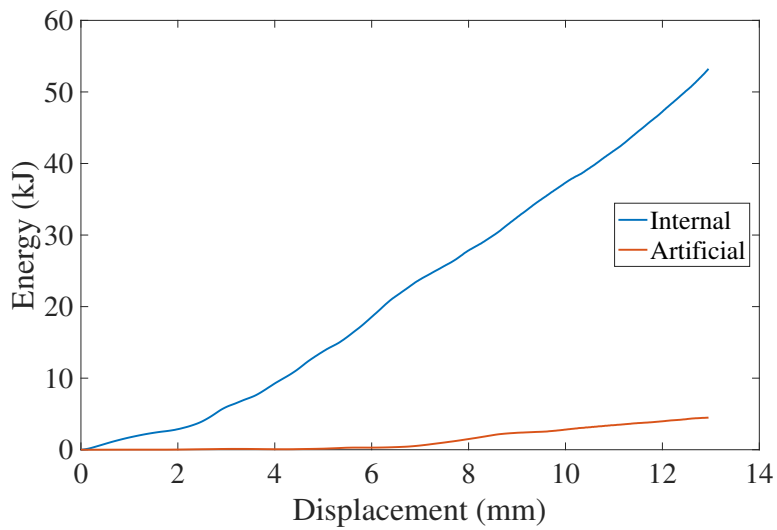A comparison between the obtained force-displacement responses, as well as the energy-displacement responses, are illustrated in Figure 7.28 and Figure 7.29 respectively. In this comparison, the responses have again been adjusted in order for the first significantly force and energy increase to occur in the support at the same displacement.

Unfortunately, no force-displacement response was obtained using MAT261 with cohesive elements. This since the time steps in the simulation got significantly decreased, causing the simulation to be stagnated. Thus, the comparison contains results from; the experimental test, simulation results using MAT261 with ERODE, simulation results using SICOMP's material model with and without delamination taken into account. From Figure 7.28 it can be distinguished that the highest obtained force peak from the simulation results was obtained with SICOMP's material model when delamination was taken into account. This deviates from the actual physical behaviour. When more damage occur, the stiffness should decrease and consequently a smaller reaction force should be obtained. This deviation may be caused by the fact that SICOMP's material model does not allow damage evolution to occur for other failure modes than the one that initiates first.

It can be observed that the addition of the cohesive elements generates a different force-displacement response with SICOMP's material model. The maximum force peak when delamination is taken into account occur at an impactor displacement of $d = 1.7$ mm, whereas it for the other model occur at $d = 4.9$ mm. The force peak with MAT261 using ERODE occur at a similar impactor displacement as with SICOMP's model using cohesive elements. However, none of the models used seems to capture a similar force-displacement response as what was observed in the experimental tests.

The absorbed energy from the experimental test, as well as from the obtained simulation results, is being illustrated in Figure 7.29(a). The energy-displacement relation with SICOMP's material model, when taking delamination into account, is higher compared to when delamination is not considered. The stresses that occur between the outermost 0 degree plies and the 90 degree plies will give rise to delamination when they become sufficiently large to initiate failure. This implies that the stresses that occur in the structure will become smaller. In addition, more damage occur and thus the stiffness decreases. This implies that the amount of absorbed energy should decrease when the cohesive elements have been added to the beam model, which is the opposite to what can be seen in Figure 7.29. With this reasoning it is possible to conclude that the increase in energy, when delamination is taken into account, is non-physical.

(a) Force-displacement relation

(b) Zoomed in Force-displacement relation

Figure 7.28:   A comparison, in the force-displacement response, between the experimental test results and finite element simulations using MAT261 with ERODE, as well as SICOMP's model with and without delamination taken into account.

(a) Energy-displacement relation

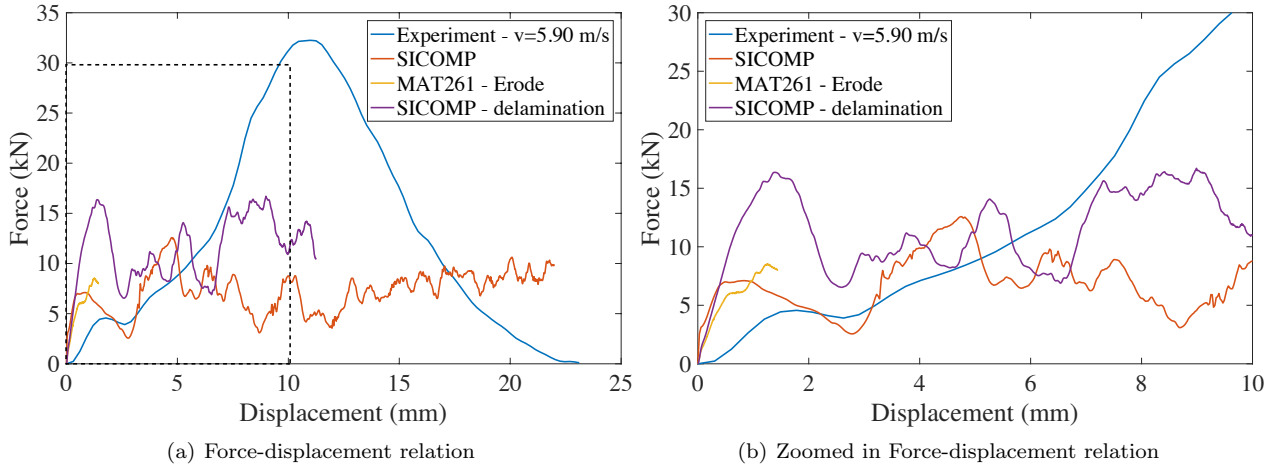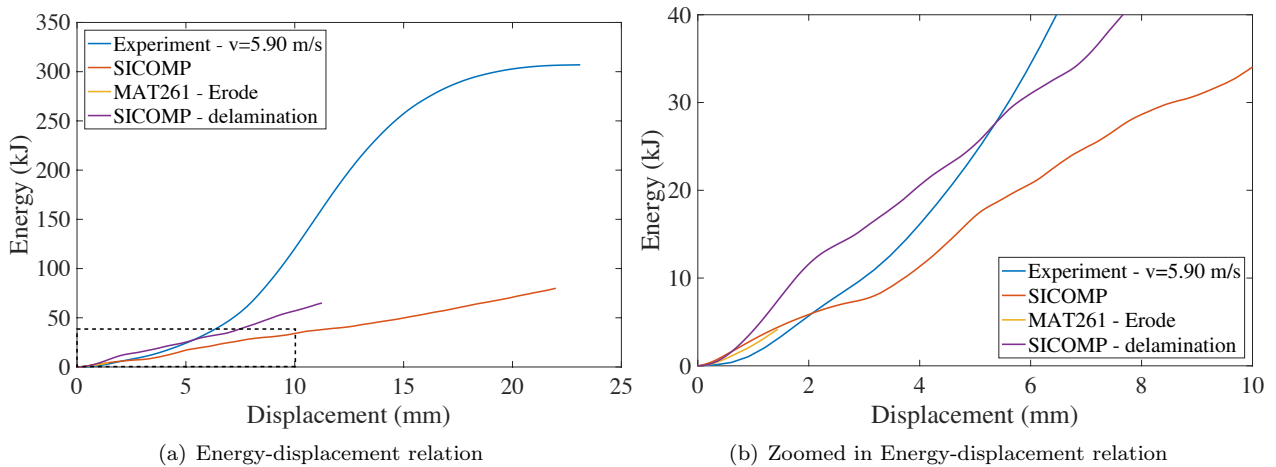(b) Zoomed in Energy-displacement relation

Figure 7.29:   A comparison, in the Energy-displacement response, between the experimental test results and finite element simulations using MAT261 with ERODE, as well as SICOMP's model with and without delamination taken into account.

7.2 Corrugated specimen

In this section the damage modes triggered in the corrugated specimen will be presented as well as the energies in the simulation for MAT261 and SICOMP's model separately. In addition a comparison will be presented where the force-displacement relation will be compared between the material models. Furthermore these results will be compared to the experimental test.

7.2.1 MAT261

The matrix damage variable, for the displacement of $d = 1.2$ mm, is illustrated in Figure 7.30(a) where it can be seen that damage occurred in almost all 0 degree plies as well as 90 degree plies.

In fibre tension, no damage was seen and therefore the damage in this mode is not shown. Figure 7.30(b) illustrates the fibre compression damage where it was observed that no final damage occurred.

(a) Matrix damage variable

(b) Fibre compression damage variable

Figure 7.30: The damage variable for fibre compression as well as matrix direction for the corrugated specimen using MAT261 for an impactor displacement of $d = 1.2$ mm.

The internal energy, the kinetic and the artificial energy are illustrated in Figure 7.31. From the results it can be observed that the internal energy increases exponentially as the impactor displacement increase. At a displacement of $d = 0.54$ mm the energy-displacement response starts to oscillate. This may be caused by dynamic effects. However, since the internal energy is significantly larger compared to the kinetic energy, this should not be the case. The reason to this oscillating behaviour may instead be related to the fact that elements are rapidly failing. The internal energy then proceeds to increase as the displacement increases. The same trend can be seen for the artificial energy. The ratio between the artificial energy and the internal energy exceeds 5% when the oscillating behaviour occurred, that is at $d = 0.53$ mm. This implies that the results become unreliable for displacements larger than $d = 0.53$ mm.

7.2.2 SICOMP's model

Just after the displacement of $d = 1.2$ mm the calculated onset strain in the failure onset routine exceeded the maximum strain. The failure onset variable in matrix tension was $f_{mt} = 7$. Thus, the strength of the material was exceeded by the calculated stress, by a factor of 7. This phenomena is the same as seen for the simulation in Section 7.1.3 and is more comprehensively explained in Section 2.2.3.

The damage arising in the corrugated specimen using SICOMP's material model is illustrated in Figure 7.32. In matrix dominated damage it was seen that the combination between compressional damage in the uppermost plies, Figure 7.32(a), and lowermost plies damaged in tension, Figure 7.32(b), correlates with the combined damage seen in Figure 7.30(a) when using MAT261. However, for the same displacement of $d = 1.2$ mm the damage was not as widespread as with MAT261. This implies that SICOMP's model absorbs more energy
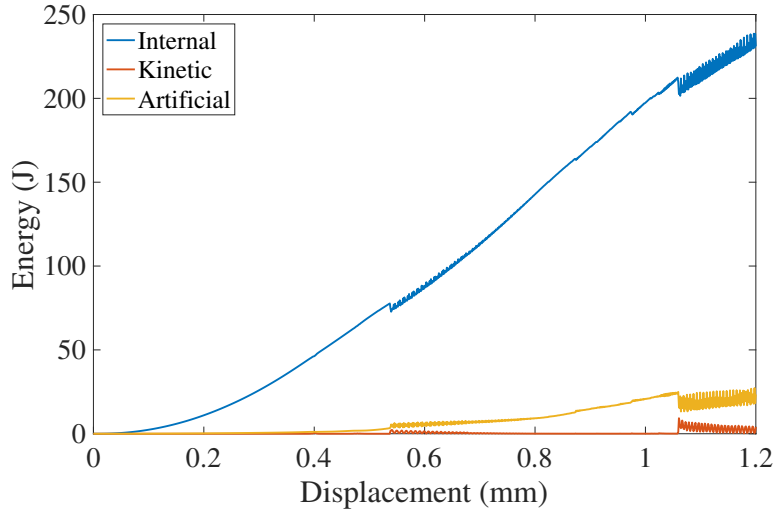
Figure 7.31:   Energy-displacement response for the corrugated specimen using MAT261.

before fully damage occur in matrix compression. This since the material response in matrix compression also take frictional effects into account. As for MAT261 no damage occurred in fibre tension and the damage in fibre compression did not reach a fully damaged state which is illustrated in Figure 7.32(c).

Figure 7.33 illustrates the energy-displacement responses for the internal energy, as well as the kinetic and the artificial energy. The internal energy increases as the impactor displacement increases. The ratio between the artificial energy and the internal energy exceeds 5% at an impactor displacement of $d = 0.44$ mm. The ratio then decrease below 5% when the displacement has reached $d = 0.46$mm. It is then kept below 5% until $d = 1.73$ mm has been reached. Since the ratio only exceeds 5% during a short time interval the results may still be considered as acceptable until $d = 1.73$ mm has been reached. However, the experimental results which this model should be compared to had a maximum displacement of 1.2 mm and thus the results, where the ratio exceeds 5%, is outside the area of interest. In addition the onset strain exceeded the maximum strain in the material model prior to the increase of artificial energy. This implies that it may not be the artificial energy that limits the reliability of the results.

(a) Matrix compression damage variable
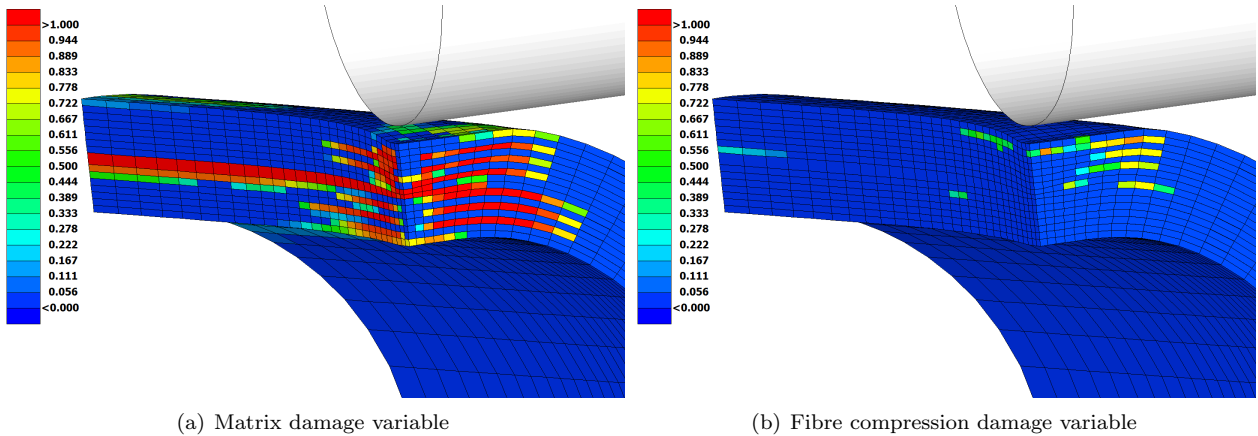
(b) Matrix tension damage variable

(c) Fibre compression damage variable
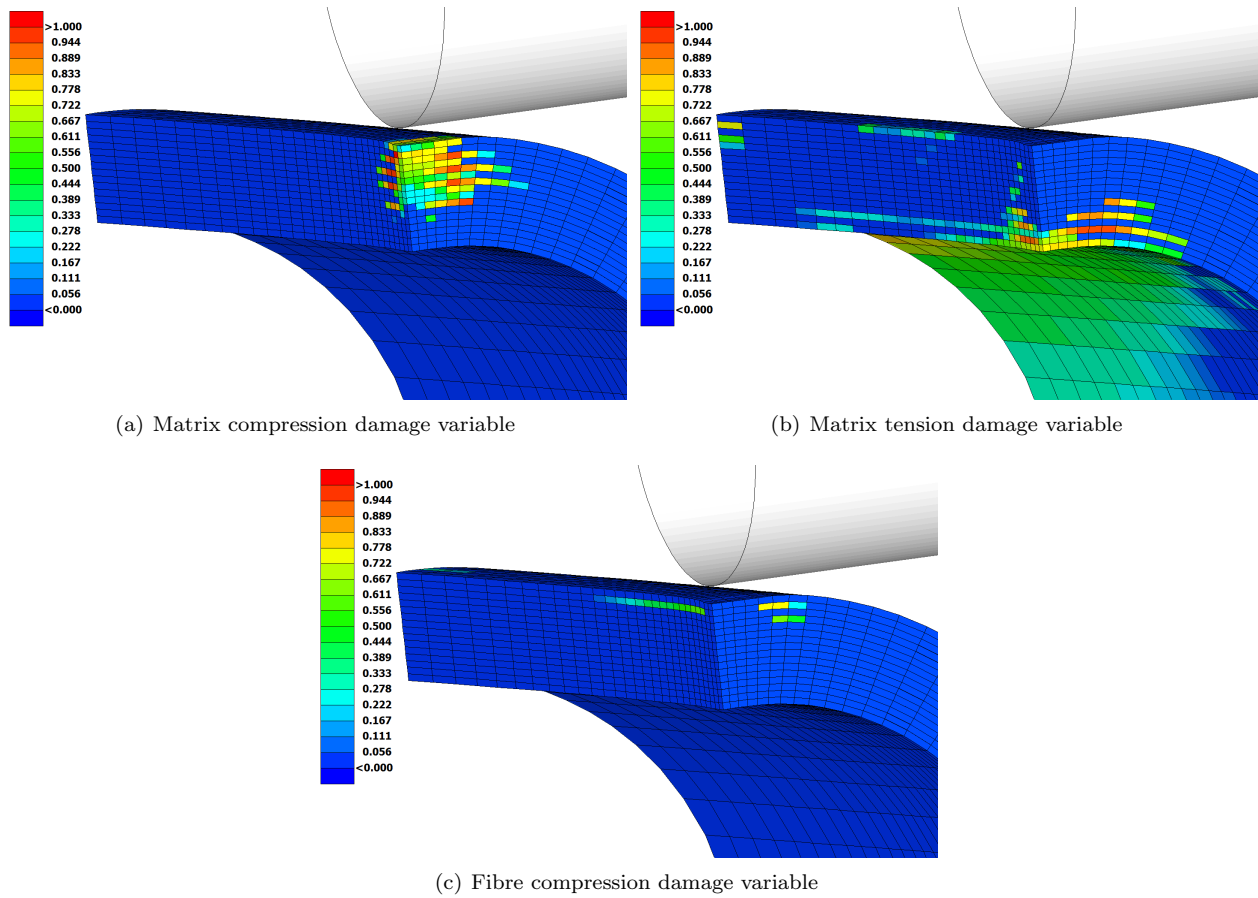
Figure 7.32: The damage variable for fibre compression as well as matrix direction for the corrugated specimen using SICOMP's material model.
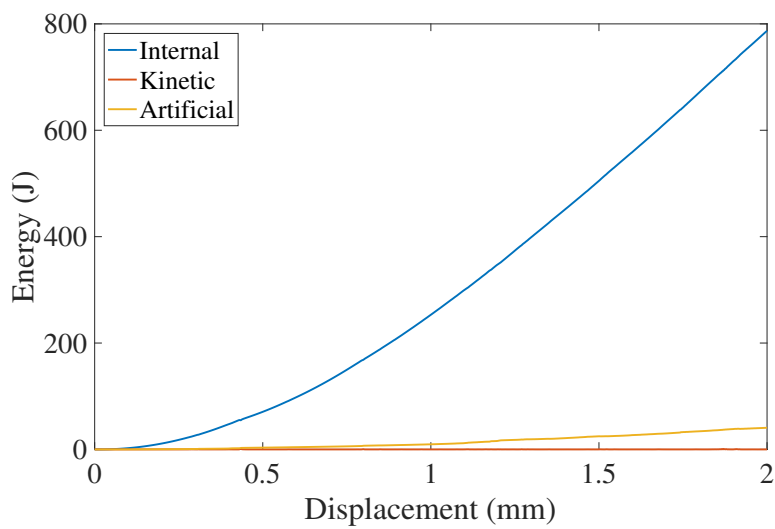
Figure 7.33: Energy-displacement response for the corrugated specimen using SICOMP's material model.

7.2.3 Comparison

The force-displacement relation for the corrugated specimen using MAT261 and SICOMP's model as well as the experimental data is illustrated in Figure 7.34. It can be observed that the initial stiffness correlates well between both material models as well as to the experimental test. However, around the displacement of $d = 0.4$ mm both material models gets a drop in force which is not seen in the experiments. After this drop, the force increase linearly with the same inclination as the experimental test using SICOMP's model. Although when the force have its peak in the experimental test the force continues to increase using SICOMP's model. For MAT261, the force continues to increase after the initial force drop. However, the remaining stiffness is lower compared to both SICOMP's model as well as to experimental test. This implies that the stresses becomes underestimated when using MAT261. In addition an oscillating behaviour occur at a displacement of $d = 0.54$ mm. As mentioned above, at this displacement, elements rapidly fails. This may be the cause to the oscillation behaviour in the force response. After a displacement of $d = 1.1$ mm a clear force drop can be observed which can be related to the damage of the two innermost 90 degree plies.
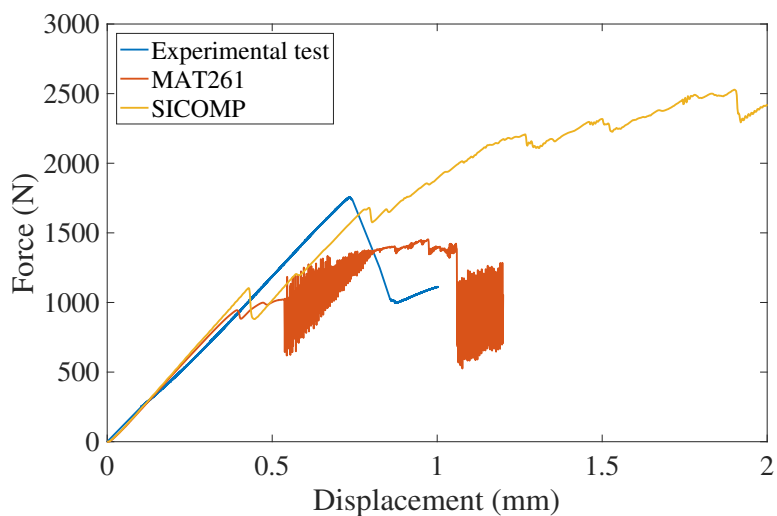
Figure 7.34: A comparison between the experimental force-displacement response for the corrugated specimen as well as when using MAT261 and SICOMP's material model.

8 Discussion

The SMP version of LS-DYNA was changed to the MPP version, since the MPP version is more developed and improved. It was noticed that the results altered significantly when changing from SMP to MPP. The results from the verification study and the benchmarking with the cube model was performed using SMP. In addition, the parameter study of the beam as well as the solid to shell transition investigation with an elastic material model, were also conducted using SMP. However, this is considered to be sufficient since these parts only are compared to results using the same version of LS-DYNA.

In this study mainly solid elements have been used. In industry shell elements are almost entirely applied due to computational costs within crash modelling. This entails that the material models implemented in a commercial software are mainly applied and used in FE-models with shell elements. Thus the experience of successfully using the material model MAT261 for large crash models with solid elements are limited. However, the solid elements have generally greater kinematic properties than shell elements, which implies that it would be an improvement in the results to use solid elements. Furthermore, SICOMP's model is previously tested using solid elements and not shell elements. Thus no documentation of using SICOMP's material model with shell elements exists.

In SICOMP's material model, failure initiation is checked until failure occur in a time step. Afterwards, no additional failure initiation is permitted. This implies that if failure in matrix compression has been initiated, the failure is not allowed to occur in the other failure modes. When the elements have been subjected to sufficiently large deformations, all the stress components are reduced and not only the one corresponding to the first initiated failure mode. As an improvement, failure initiation could be checked even after the first initial failure. This would allow the damage to switch into another failure mode, which in turn allow a competition between failure modes even in the damage evolution. Furthermore, if this was implemented only the stress components which corresponds to the actual activated damage evolution mode could be reduced.

When it comes to SICOMP's material model, there is no guarantee that the onset strain should be less than the maximum strain, for the present version. If the corresponding strain, to the calculated stress in an element, exceeds the maximum failure strain, the response will go from a non-damaged state to be fully damaged within two time increments. This implies that the material model will become sensitive against rapid changes in stress response in the elements. Further investigation and improvements would be needed in order to obtain a material model which accurately can treat this sudden change. One possible way to solve this would be to reduce the calculated onset strain as soon as this problem occur, in such a way that the stress response still follows the intended stress-strain behaviour.

Another short-term solution would be to reduce the time step size. This since the difference between two time steps becomes smaller, when using smaller time steps. As described in Section 7.1.3, by reducing SCFT=0.9 to SCFT=0.6 allowed the simulation, with cohesive elements using SICOMP's material model, to overcome this problem. The same problem occurred in Section 7.2.2, where the corrugated specimen was studied. The corrugated specimen was included during the final phase of the project. Thus, it was not possible, due to time limitations, to investigate if a reduced time step would solve this problem. However, the onset strain exceeding the maximum failure strain occurred after a displacement of $d = 1.2$ mm was reached, which was the displacement where the experimental test was ended. By this reasoning the results up until $d = 1.2$ mm should be reliable and thus a valuable comparison could still be conducted.

The beam was modelled using as close to cubic elements as possible. However, in the radius cubic elements could not be fulfilled. Therefore, since one of the larger damage modes occurred in the radius, in combination with that SICOMP's model does not compensate for non-cubic elements error in the damage evolution calculation, this might be a source of error. It is hard to conclude how this specific modelling error effect the overall beam response.

During the project some problems regarding negative volumes was seen, mainly for MAT261. In order to prevent this, the function ERODE was applied for the solid uniform beam. However, the function only bases the quality of the element by its shape, and no consideration if the element contributes to the models stiffness, is taken into account. Another approach to remove these elements with negative volumes is to change the material properties in order initiate failure in advance. However, since a comparison between already conducted experiments should be conducted, this alternative was not possible.

In the beam model, negative internal energy occurred using the material model MAT261. This occurred for the solid uniform beam model, the model including delamination as well as the model with the transition from solid to shell. This unphysical behaviour does not occur using the same FE-models with SICOMP's material model. This implies that some numerical problems occur when combining MAT261 with these FE-models. An investigation was conducted where it was tested if the negative energy occurred due to strangely shaped elements, released from the beam. This was done by preventing damaged elements to be removed. The results showed that the negative internal energy still remained. Thus, this possible source of error may be disregarded.

An increased trend in artificial energy was observed in the beam simulation. As described in Section 2.1.3, the simulation results becomes unreliable when the artificial energy exceeds 5%. With MAT261 it is hard to draw any conclusion whether the artificial energy is high or not, since the internal energy was negative. With SICOMP's material model it was possible to observe that, in the solid uniform beam, the artificial energy exceeded 5% at an impact displacement between $d = 5$ mm to $d = 6$ mm. Therefore, after this increase in artificial energy, the results becomes unreliable.

In this thesis, no in-situ effects have been accounted for. These effects occur when major changes in the fibre orientation is present between neighbouring plies. In the three-point bending of the beam, these effects were assumed to be negligible. The majority of the plies were oriented in the same direction, thus the potential in-situ effects should be small. However, in the corrugated specimen a cross ply stack-up was used. This indicates that in-situ effects should be more pronounced in this model. Although, the corrugated specimen was included late in the project and due to the limited time the in-situ effects were not taken into account. To fully understand these effects, a deeper investigation is required, which was not possible. If in-situ effects would be included, the failure would theoretically be postponed. Thus, the initial force drop in the FE-results may instead be delayed and thus occur closer to the experimental force drop.

In the experimental test of the corrugated specimen it was observed that damage occurred due to matrix damage, as well as delamination. However, the FE-model did not include failure mechanisms due to delamination, which implies that one of the main driving damage mechanisms is not considered. This implies that the model excludes an important part of the physics behind the observed failure in the experiment.

9 Conclusions and Future work

9.1 Conclusions

The purpose of this Master's Thesis was to implement a new material model, developed at Swerea SICOMP, into the commercial software LS-DYNA. It also intended to verify the implementation of the material model, using data from already performed finite element simulations. Furthermore, to validate the new material model against available experimental tests, as well as to benchmark it against an already existing material model in LS-DYNA. This in order to determine if the new material model improved the accuracy of the results.

From the results it was observed that the transfer of the material model had been successfully carried out. However, in fibre compression the response deviated. In the benchmarking between SICOMP's model and MAT261 the response deviated in matrix compression as expected. This since friction within the matrix is taken into account in SICOMP's material model, which is not included in MAT261.

When extending the benchmark investigation to a three-point bending of a beam, both SICOMP's material model and MAT261 predicted reasonable failure of the beam upon crushing. However, the force-displacement response and energy absorption was far from the experimental test. When adding delamination in all interfaces between 0 and 90 degree plies, a non-intuitive response occurred where the energy absorption became higher. Even though delamination is taken into account the force-displacement response and energy absorption were not close to the experimental test.

A corrugated specimen was also studied. The results shows a fairly good stiffness correlation in the force-displacement relation against the experimental test, until failure occurred in the experiment. The correlation was seen for both the material models, where SICOMP's model was closest to the experiment. However, delamination, which is one of the main driving failure mechanisms, was not included.

The assumption of that the scaling of the fracture energy density is calculated without taking the fracture angle into account, may give error in the absorbed energy in matrix compression using SICOMP's model. However, the amount of possible energy absorption in this mode is low. Furthermore, no additional failure mode initiation is permitted after failure has been onset. Moreover, there is no guarantee that the onset strain should be less than the maximum strain, for the present version. Thus, SICOMP's material model is sensitive to large time steps.

In order to discretise the solid uniform beam such that all plies through the thickness of the beam, and preserve cubic elements in the fracture zone, the number of solid elements were 5.88 millions with 6.2 million nodes. Since the solid element formulation have three degrees of freedoms for each node, the formulation have no rotational degrees, the number degrees of freedom were 18.6 million. To reach the same displacement of 22 mm as for the experiment test, with an impact velocity of 5.9 m/s, it was required to run for 70 hours using 40 cpu's with a time step of $1.1 \cdot 10^{-8}$ s. If this refinement should be applied to a larger structure compared to this beam, problems due to high simulation costs will occur. This will in turn complicate an eventual implementation of this modelling approach, in daily simulation usage.

There are several improvements which can be done for SICOMP's material model in order to establish a more reliable material model in crash simulations, cf. Section 9.2 describing recommended future work. Although, the overall conclusion is that the present version of SICOMP's material model appear to be more robust than MAT261.

9.2 Future Work

In order to improve the simulation accuracy and in that way reduce the deviation to experimental results some work is still remaining. Future improvement and development can be divided into three main areas; reduce computational cost, improve software stability for anisotropic materials as well as improve the material models. The subsequent sections more specific describes some areas to be improved.

- Re-investigate the transition from solid to shell using constrained nodal rigid body with the transition further away from the fracture zone as well as investigate if an alternative transition approach from solid to shells can be used in order to reduce the computational cost.

- As an alternative, investigate if a thick-shell formulation can be used in the modelling of the three point bending test in combination with cohesive elements.

- Different eroding techniques can be investigated in order to exclude nonphysical elements which may cause negative volumes. This in order to be able to run longer simulations which in turn makes it possible to compare simulation results to experimental results.

- Investigate if the modelling of the three point bend test of the beam can be improved. For instance by including the entire testrig in the dynamic simulation in order to investigate the dynamic effects of the rig. Moreover, adding cohesive elements between all plies in order to further investigate the delamination failure mechanisms.

- Extend the simulations of the beam to include a quasi-static test as well as other experimentally investigated impact velocities from the dynamic test. Furthermore, a comparison of the fracture arising should be conducted between the simulation results and the experiments when fractography has been carried out.

- In the simulation of the corrugated specimen in-situ effects can be included in order to get more accurate FE results. Furthermore, delamination can be taken into account by adding cohesive elements. Decrease the time step in the simulation in order to prevent the onset strain to be larger than the maximum strain with SICOMP's model.

- Improve SICOMP's model by including the physics of kinking in fibre compression as well as by making it compatible with non-cubic elements and accurate for inclined failure planes. Investigate how to solve the problem that the onset strain can exceed the maximum strain. Finally allow initiation of additional damage in another failure mode after initial failure as well as only compensate the stresses which corresponds to the current failure.

References

[1] B. D. Agarwal, L. J. Broutman, and K. Chandrashekhara, *Analysis and Performance of Fiber Composites*, 3rd ed. Wiley, 2006.

[2] L. Grauers, R. Olsson, and R. Gutkin, Energy absorption and damage mechanisms in progressive crushing of corrugated ncf laminates: fractographic analysis, *Composite Structures* vol. **110**, 110–117, 2014.

[3] G. C. Jacob, J. F. Fellers, S. Simunovic, and J. M. Starbuck, Energy absorption in polymer composites for automotive crashworthiness, *Journal of Composite Materials* vol. **36**, no. 7, 813–850, 2002.

[4] R. Alia, Z. Guan, N. Jones, and W. Cantwell, The energy-absorption characteristics of metal tube-reinforced polymer foams, *Journal of Sandwich Structures Materials* vol. **17**, no. 1, 74–94, 2015.

[5] S. Pinho, L. Iannucci, and P. Robinson, Physically based failure models and criteria for laminated fibre-reinforced composites with emphasis on fibre kinking, Part II: FE implementation, *Composites Part A: Applied Science and Manufacturing* vol. **37**, no. 5, 766–777, 2006.

[6] A. C. Orifici, I. Herszberg, and R. S. Thomson, Review of methodologies for composite material modelling incorporating failure, *Composite Structures* vol. **86**, no. 1-3, 194–210, Nov. 2008.

[7] S. T. Pinho, C. G. Dávila, P. P. Camanho, L. Iannucci, and P. Robinson, "Failure models and criteria for frp under in-plane or three-dimensional stress states including shear non-linearity", Tech. Rep., 2005, p. 68.

[8] A. Turon, P. P. Camanho, J. Costa, and C. G. Davila, "An interface damage model for the simulation of delamination under variable-mode ratio in composite materials", Tech. Rep. October, 2004.

[9] P. P. Camanho, C. G. Davila, M. F. de Moura, and M. F. D. Moura, Numerical simulation of mixed-mode progressive delamination in composite materials. *Journal of composite materials* vol. **37**, no. 16, 1415–1438, 2003.

[10] T. Johansson, D. Storer, R. Matheis, A. Gutsche, and C. Kurzböck, "Deliverable D2.4, Report on thick UD-composite structure modelling", Tech. Rep. Revision 1, 2013.

[11] D. Siromani, J. Awerbuch, and T. M. Tan, Finite element modeling of the crushing behavior of thin-walled cfrp tubes under axial compression, *Composites Part B: Engineering* vol. **64**, 50–58, 2014.

[12] J. Karlsson and M. Fagerström, "Edge-to-edge cohesive shell elements in ls-dyna", Tech. Rep., DYNAmore GmbH, 2015.

[13] D. C. Fleming, Modelling composite crushing initiation using a cohesive element formulation, *International Journal of Crashworthiness* vol. **16**, no. 5, 475–485, 2011.

[14] T. Belytschko, J. S.-J. Ong, W. K. Liu, and J. M. Kennedy, Hourglass control in linear and nonlinear problems, *Computer Methods in Applied Mechanics and Engineering* vol. **43**, no. 3, 251–276, 1984.

[15] S. Costa, "Material model implementation – version one", Tech. Rep., Swerea SICOMP, 2015.

[16] R. Olsson, "In-situ strength of composite plies - theory and experiments", Tech. Rep., Swerea SICOMP, 2016.

[17] K. Vallons, "The behaviour of carbon fibre – epoxy NCF composites under various mechanical loading", PhD thesis, Katholieke Universiteit Leuven, 2009.

[18] M. Uustalu, "Crush simulation of carbon/epoxy ncf composites - development of a validation test for material models", Master's thesis, Swerea SICOMP, 2015.

[19] R. Gutkin and S. T. Pinho, Combining damage and friction to model compressive damage growth in fibre-reinforced composites, *Journal of Composite Materials*, 2014.

[20] S. T. Pinho, L. Iannucci, and P. Robinson, Physically-based failure models and criteria for laminated fibre-reinforced composites with emphasis on fibre kinking, Part I: Development, *Composites Part A: Applied Science and Manufacturing* vol. **37**, no. 1, 63–73, 2006.

[21] *LS-DYNA keyword user's manual, Volume II - material models*, version R8.0, March 2015.

[22] G. Petersson, "Modeling crash behaviour in future lightweight composite vehicles - quasi-static testing at volvo trucks", Volvo Group Trucks Technology, Jan. 2016.

[23] J. Jergeus, "CFRP door beam QS & dynamic testing", Volvo Cars Safety Centre, Dec. 2015.

[24] S. Costa, "Crushing / bending of a corrugated specimen", Tech. Rep., Swerea SICOMP, 2015.

[25] T. Bru, P. Hellström, R. Gutkin, D. Ramantani, and G. Peterson, Characterisation of the mechanical and fracture properties of a uni-weave carbon fibre/epoxy non-crimp fabric composite, *Data in Brief*, 1–16, 2016.

[26] *LS-DYNA keyword user's manual, Volume I*, version R8.0, March 2015.

[27] R. Grahn and P.-Å. Jansson, *Mekanik: statik och dynamik*. Lund: Studentlitteratur, 2013, vol. 3. uppl.

[28] T. Johansson, C. Kurzböck, R. Matheis, and G. Gstrein, "Deliverable D2.2, Report on modelling for fabric reinforced structures", Tech. Rep. Revision 4, 2013.

[29] L. Gigliotti and S. Pinho, Multiple length/time-scale simulation of localized damage in composite structures using a mesh superposition technique, *Composite Structures* vol. **121**, 395–405, 2015.

A Appendix - Hourglass investigation

An hourglass investigation was conducted using material model MAT261. The model studied was a cube with the same setup as in Chapter 5 using eight solid elements. The loading condition studied was fibre compression since this was the case where the most artificial energy occur.

The hourglass formulations compared were the default viscous based formulation for solid elements, that is $IHQ = 2$ in CONTROL-HOURGLASS, and a stiffness based formulation. The are two stiffness based formulations for an explicit solver in LS-DYNA, both according to Flanagan-Belytschko. The one used in the comparison is the one which uses exact volume integration, $IHQ = 5$ in CONTROL-HOURGLASS. The stiffness based formulation was tested using hourglass coefficient, QH, of the default value of 0.1 as well as 0.05 and 0.02.

The stress-strain response using the different hourglass formulations can be seen in Figure A.1. It can be seen that the only formulations which did not pre-terminate was the default viscous based formulation and the stiffness based formulation using $IHQ = 0.05$. The viscous based formulation have a drop in stress down to zero at $\varepsilon = 3.2\%$ whilst the stiffness based formulation give an increase in stress at $\varepsilon = 3.3\%$ until a stress drop at $\varepsilon = 4.6\%$. The model does not reach fully damage using stiffness based formulation.

A study of the energies for the formulations which not pre-terminated was conducted and the results can be seen Figure A.2. For the viscous based formulation, the artificial energy increases significantly at $\varepsilon = 3.2\%$ which is the same strain as the drop in strain occur. In the stiffness based formulation, the artificial energy increases slightly at $\varepsilon = 3.5\%$ and oscillates. At $\varepsilon = 7\%$ the artificial energy increases to a value of 20% in ratio to the internal energy. Furthermore a small deviation of the internal energy response occur at $\varepsilon = 4.6\%$.
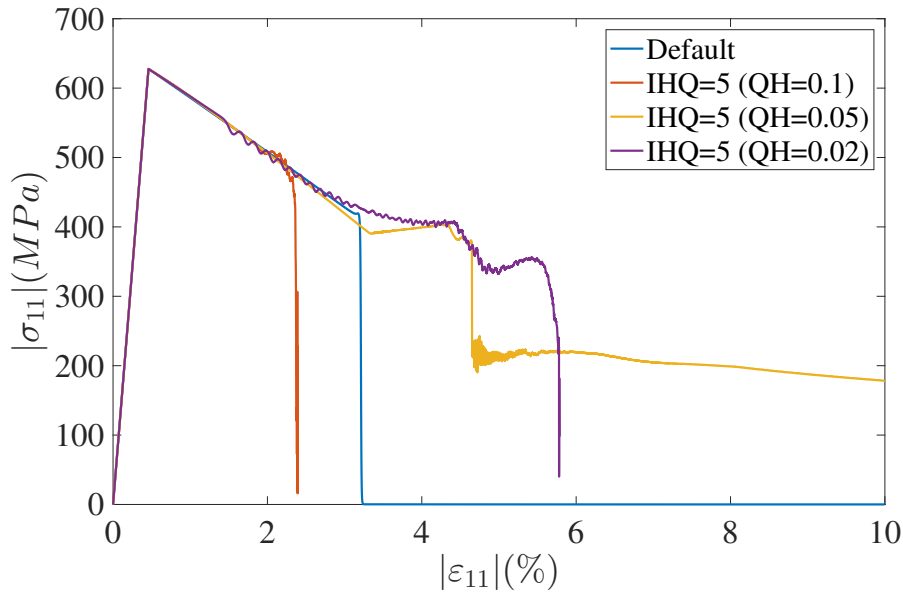
Figure A.1: Stress-strain relation in fibre compression for MAT261 using different hourglass formulations and coefficients.

(a) Default: Viscous based (EQ 2)   (b) Stiffness based (EQ5) HQ=0.05
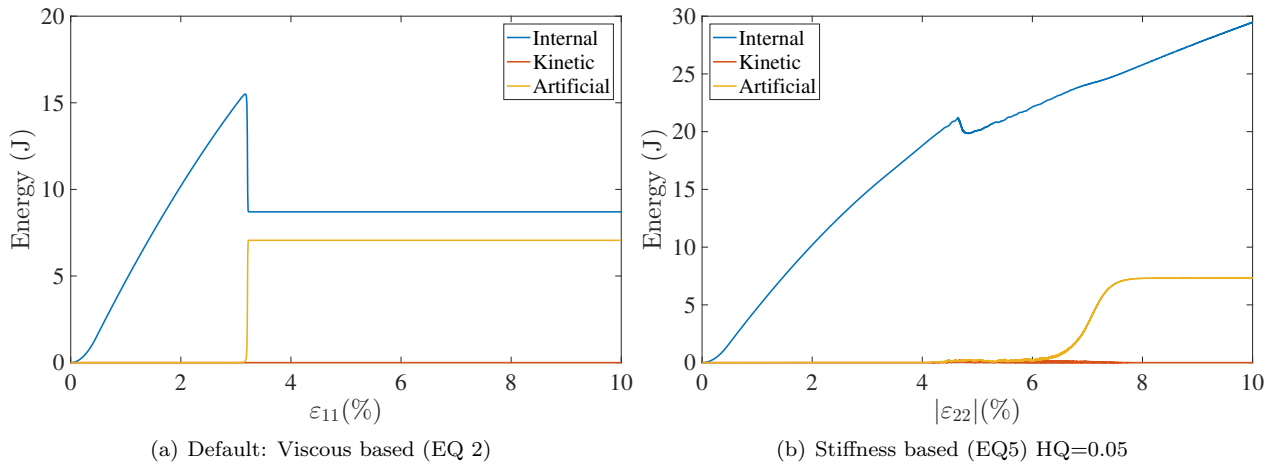
Figure A.2: Energy response for the viscous based ($IHQ = 2$) and stiffness based ($IHQ = 5$) formulations.

The sudden increase in artificial energy for the viscous formulation and the corresponding drop in stress at the same strain indicates that numerical problems occur using this formulation. For the stiffness based formulation using $QH = 0.05$ the stress-strain response have some numerical problems as well both at the stress drop as well as in the end of the simulation. However, the stiffness based formulation with $QH = 0.05$ seemed to give a more stable response and was therefore determined to be used in this project.

B   Appendix - user material

The material card for the user material (SICOMP's material model), when calling on dyn21.f, with the corresponding values for the cube, beam and corrugated specimen simulations can be seen in Table B.1 and Table B.2. A more detailed description of some of the material parameters will now be presented. A brief description of each individual parameter can be found in LS-DYNA's user manual [21].

In card one, the density (RO) of the material is defined as well as which user material that was used by setting MT between 41 and 50. The number of material inputs which is inserted in card five is defined by LMC. The strength parameters of the material are the only ones that are not hard coded within the material subroutine. Thus, these were defined in the material card, together with the inputs required for LS-DYNA to determine the time step. Parameter P1 and P2 corresponds to the bulk modulus as well as the shear modulus of the material, which were addressed as IBULK and IG in card 5. Parameter P3 to P7 corresponds to the strength parameters of the material, and they were defined in the following manner; P3 corresponds to XT, P4 corresponds to XC, P5 corresponds to YT, P6 corresponds to SL and finally P7 corresponds to ST.

To calculate the values, of IBULK and IG, the largest Young's modulus in the material was used since this gives the smallest time step. Thus the calculation of the the bulk and shear modulus was performed in accordance to Equation (B.1). The last parameter in card one is IORTHO where it is defined if the material is othotropic or having spot weld thinning. In this investigation, IORTHO was set to one and since the material used is orthotropic.

$$K = \frac{E_{11}}{3(1 - 2\nu_{23})} \qquad G = \frac{E_{11}}{2(1 + \nu_{23})} \tag{B.1}$$

In card two, the only value of interest in this application is the flag IFAIL which for zero do not allow deletion of failed elements and for a value of one do allow deletion. In the cube test, the total response even after total failure was of interest and thus this parameter was set to zero whilst to the beam test deletion was required.

The cards three and four determines the direction of the material coordinate system in relation to the local element coordinate system. There are several methods to define this relation and the desired method is determined by the value on AOPT. In this material model there were only two definitions of interest for this application using solid elements. The first definition (AOPT=2) defines the first material direction (a) using a vector **a** as well as a vector **d** which is setting the second (b) direction of the material. The second definition (AOPT=3), which is the one used in this investigation, defines a plane where the direction of the material is defined using an angle. The vector **v** is used to span this plane together with the normal **n** to the element coordinate system. If setting vector **v** to **v**=[1,0,0] and the angle to zero (BETA=0) then the first material direction (a) will be the same as the first direction of the local system for the element. Then in order to rotate the direction of (a) either the angle can be altered or the vector **v**. In addition MACF can be used to make quick changes between different material axes. However, this addition were not used. Furthermore IEVTS is a material parameter used if thick shell formulation five is used.

Table B.1: Material card for the user material used in the cube simulations.

Card 1	MID	RO	MT	LMC	NHV	IORTHO	IBULK	IG
	X	1.6e-9	43	7	38	1	1	2
Card 2	IVECT	IFAIL	ITHERM	IHYPER	IEOS			
	0	0	0	0	0			
Card 3	AOPT	MAFC	XP	YP	ZP	A1	A2	A3
	3	1	-	-	-	-	-	-
Card 4	V1	V2	V3	D1	D2	D3	BETA	IEVTS
	1	0	0	-	-	-	0	0
Card 5	P1	P2	P3	P4	P5	P6	P7	P8
	226667	48571.4	1787	626	29	40	60	0

III

Table B.2: Material card for the user material used in the beam and the corrugated specimen simulations.

Card 1	MID	RO	MT	LMC	NHV	IORTHO	IBULK	IG
	X	1.51e-9	43	7	38	1	1	2
Card 2	IVECT	IFAIL	ITHERM	IHYPER	IEOS			
	0	1	0	0	0			
Card 3	AOPT	MAFC	XP	YP	ZP	A1	A2	A3
	3	1	-	-	-	-	-	-
Card 4	V1	V2	V3	D1	D2	D3	BETA	IEVTS
	1	0	0	-	-	-	0	0
Card 5	P1	P2	P3	P4	P5	P6	P7	P8
	220000	47143	1787	631	29.2	77.8	60	0

C Appendix - MAT261

The material cards defining the material response using MAT261 can be seen in Table C.1 and Table C.2 for the cube, the beam and the corrugated specimen test. In the next paragraphs a description of some of the parameters will be presented. For more information see LS-DYNA's user manual [21].

Table C.1: Material card MAT261 used in the cube simulations.

Card 1	MID X	RO 1.6e-9	EA 136000	EB 9150	EC 9150	PRBA 0.019	PRCA 0.019	PRCB 0.4
Card 2	GAB 4900	GBC 3267.86	GCA 4486.81	AOPT 3	DAF 1	DKF 1	DMF 1	EFS 0
Card 3	XP -	YP -	ZP -	A1 -	A2 -	A3 -		
Card 4	V1 1	V2 0	V3 0	D1 -	D2 -	D3 -	MANGLE 0	
Card 5	ENKINK 25	ENA 50	ENB 0.222	ENT 1.92	ENL 1.92			
Card 6	XC 626	XT 1787	YC 130	YT 29	SL 40			
Card 7	FIO 62	SIGY -	LCSS -	BETA -	PFL -	PUCK -	SOFT 1	

Table C.2: Material card MAT261 used in the beam and the corrugated specimen simulations.

Card 1	MID X	RO 1.51E-9	EA 132000	EB 9300	EC 9300	PRBA 0.02	PRCA 0.02	PRCB 0.43
Card 2	GAB 4400	GBC 3251.75	GCA 4558.82	AOPT 3	DAF 0	DKF 0	DMF 0	EFS 0
Card 3	XP -	YP -	ZP -	A1 -	A2 -	A3 -		
Card 4	V1 1	V2 0	V3 0	D1 -	D2 -	D3 -	MANGLE 0	
Card 5	ENKINK 103,1	ENA 67,1	ENB 0,149	ENT 0,69	ENL 0,69			
Card 6	XC 631	XT 1787	YC 130	YT 29.2	SL 77.8			
Card 7	FIO 62	SIGY -	LCSS -	BETA -	PFL -	PUCK -	SOFT 1	

In card one and two the density, Young's modulus, Poisson's ratios as well as the shear modulus are defined. The parameter values are defined in the material coordinate system {A,B,C}, sometimes referred to as {1,2,3}. The equations needed to determine the Poisson's ratio, as well as the shear modulus, are presented in Equation

(C.1).

$$
\begin{cases}
\nu_{BA} = \nu_{21} = \dfrac{E_{22}}{E_{11}} \nu_{12} \\[3mm]
\nu_{CA} = \nu_{31} = \dfrac{E_{33}}{E_{11}} \nu_{13} \\[3mm]
\nu_{CB} = \nu_{32} = \dfrac{E_{33}}{E_{22}} \nu_{23}
\end{cases}
\quad
\begin{cases}
G_{AC} = G_{12} \\[3mm]
G_{BC} = G_{23} = \dfrac{E_{22}}{2(1+\nu_{23})} \\[3mm]
G_{CA} = G_{31} = \dfrac{E_{33}}{2(1+\nu_{31})}
\end{cases}
\tag{C.1}
$$

In accordance to Appendix B, the direction of the material with respect to the local element coordinate system was defined using AOPT set to three using vector $\mathbf{v}$. The only difference between the cards for MAT43 and MAT261 is that the angle BETA in MAT43 here is called MANGLE. In card two, the flags DAF, DKF and DMF determines if failed elements should be visualised or removed.

The intralaminar and translaminar fracture toughness for the material is defined in card five and the strength properties in card six. The translation from the parameters in the material card to the defined material parameters can be seen in Table C.3. In the last card, the fracture angle in transverse compression is defined in FIO which default value are 53 degrees. However for this material, the angle is $62°$ in accordance to Chapter 4.

The last behaviour to include it the strength reduction in a crashfront. A crash front is initiated in the neighboring elements if a specified number of plies have failed in an element. The number of elements required to fail is determine in parameter PFL where the default setting requires that all plies must fail. The reduction of the strength of the material in the crashfront elements is determined in SOFT. When no reduction is allowed the SOFT parameter is one whilst a value of zero gives fully reduction. In this case no reduction of the strength was allowed.

Table C.3: Translation of definition in material card to material parameters.

ENKINK	$G_c^{fc}(kJ/m^2)$	Longitudinal compressive failure
ENA	$G_c^{ft}(kJ/m^2)$	Longitudinal tensile failure
ENB	$G_c^{mt}(kJ/m^2)$	Intralaminar matrix tensile failure
ENT	$G_{IIc}^{mt}(kJ/m^2)$	Intralaminar matrix tranverse shear failure
ENL	$G_{IIc}^{ft}(kJ/m^2)$	Intralaminar matrix longitudinal shear failure